University of California, Merced

Ionic Transport through Carbon Nanotube Porins

A Dissertation Submitted in Partial Satisfaction of the Requirement

for the Degree of Doctor of Philosophy

In

Chemistry and Chemical Biology

In

School of Natural Sciences

By

Yun-Chiao Yao

Committee in Charge:

Professor Michael E. Colvin, Chair
Professor Aleksandr Noy, Advisor
Professor Tao Ye
Professor Meni Wanunu

Spring, 2021

The dissertation of Yun-Chiao Yao is approved, and it is acceptable in quality and form for publication on microfilm and electronically:

_____ Date _____
Professor Michael E. Colvin

_____ Date _____
Professor Aleksandr Noy

_____ Date _____
Professor Tao Ye

_____ Date _____
Professor Meni Wanunu

University of California, Merced
2021

Ionic Transport through Carbon Nanotube Porins

To My Family.

What I cannot create, I do not understand.

-Richard Feynman

Acknowledgement

It has been a unique journey for me from studying peptide structures and functions at National Taiwan University to advancing the nanofluidic field using carbon nanotube porin channels at the University of California, Merced and Lawrence Livermore National Laboratory (LLNL). Lots of learning, trying, and some accomplishments along my path pursuing greater understanding in chemistry. I cannot be here, finishing my doctoral studies, without the many people guiding, helping, and supporting me over these years.

First and foremost, I would like to thank my advisor Prof. Aleksandr Noy. I decided to come here after several emails and talks with him. In the Noy group, I have been working on exciting projects and Prof. Noy has always provided sharp insight and supportive mentorship. I am deeply grateful for all the things I have learned from him, especially for the discussion on scientific ideas and his scientific attitude.

I would also like to thank my dissertation committee: Prof. Michael E. Colvin and Prof. Tao Ye at UC Merced, and Prof. Meni Wanunu at Northeastern University. Their support and guidance has helped sharpen my dissertation work.

I would like to acknowledge the Center for Enhanced Nanofluidic Transport (CENT) for the fruitful collaborations and discussions with various members and also the academic cooperation program at LLNL for access to resources and facilities. I would also like to thank all of the collaborators I have worked with over the last few years: Prof. Wanunu's group, Prof. Aluru's group, Prof. Ando's group, Prof. Reed's group, and Prof. Rawson's group.

I would like to give special thanks to Dr. Robert Henley for his mentoring when I started my PhD work. The three months we worked together laid a solid foundation for my following projects. I would also like to thank Dr. Nga Ho, specifically for the mental (and food) support. I love our chatting time. In addition, I would like to thank Dr. Alice Gillen for helping me with the editing of this dissertation. I'm also grateful for all the help and support I got from all the Noy group members over the years: Dr. Ramya Tunuguntla, Dr. Yuliang Zhang, Dr. Jeremy Sanborn, Dr. Xi Chen, Dr. Yuhao Li, Dr. Margaryta Sheliakina, Dr. Jacqueline Hicks, Zhongwu Li, Wu Zhan, and Sidi Zhao.

I would like to thank my dear friends all over the world, and would like to give special thanks to Patricia Shuppert and Stewie for giving me a home feeling in the US.

Last but not least, I would like to thank my wonderful family. The unconditional love from my parents, Pai-Tao Yao and Tsau-Ying Tsao, and my young brother, Yun-Han Yao, makes me fearless when exploring the world. Also, I would like to thank my beloved husband, Kai-Chieh Chen, for always being there for me. The adventures, as well as daily life, with Kai-Chieh and Marvelette are cherished moments for me.

Abstract

Ionic Transport through Carbon Nanotube Porins

by Yun-Chiao Yao

Advisor: Professor Aleksandr Noy

Doctor of Philosophy in Chemistry and Chemical Biology

University of California, Merced

Nanofluidic channels confine water and ions down to length scales that are comparable to the sizes of individual molecules. This strong confinement creates unique transport phenomena, such as enhanced water flow, unusual selectivity patterns, and strong electroosmotic coupling. To probe transport behavior and the underlying physics under extreme confinement, our group developed a model system - carbon nanotube porins (CNTPs), which are synthetic analogs of aquaporins made of carbon nanotubes. CNTPs have well-defined, nanometer-sized diameters and ultrashort lengths of *ca.* 10 nm. In addition, CNTPs have the ability to self-insert into lipid bilayers, forming artificial membrane channels. Using ionic transport measurement setups adapted from protein channels, I was able to obtain ionic conductance scaling and selectivity values through CNTPs with average diameters of 0.8 nm and 1.5 nm. While the 0.8 nm-diameter CNTPs showed exclusive-cation selectivity, the 1.5 nm-diameter CNTPs demonstrated strong ion-water coupling during transport. Furthermore, I demonstrated that built-in charges (end-groups), environmental changes (such as altering pH), or external forces (such as applying a gate voltage) could alter the ionic distribution and selectivity of the CNTP channels. Our CNTPs represent a versatile nanofluidic model system that we can utilize to advance our understanding and control of ion and water behavior at the nanoscale, which could further benefit desalination membrane design and lab-on-a-chip sensing.

Table of Contents

List of Figures

List of Tables

Abbreviations

ALD	Atomic Layer Deposition
AQP	Aquaporin
BNNT	Boron Nitrite Nanotube
CNT	Carbon Nanotube
SWNT	Single-Walled Carbon Nanotube
MWNT	Multi-Walled Carbon Nanotube
CNTP	Carbon Nanotube Porin
nCNTP	Narrow Carbon Nanotube Porin
wCNTP	Wide Carbon Nanotube Porin
CVD	Chemical Vapor Deposition
DOPC	1,2-Dioleoyl-*sn*-Glycero-3-Phosphocholine
DLS	Dynamic Light Scattering
I-V Curves	Current-Voltage Curves
LUV	Large Unilamellar Vesicle
MD	Molecular Dynamics
PL	Photoluminescence
RED	Reverse Electrodialysis
TEM	Transmission Electron Microscopy

Chapter 1. Nanofluidics

*Parts of Section 1.2, 1.4, 1.5, and 1.6 are adapted from the book chapter entitled: "Advances in Water Desalination Technologies, Chapter 14: Transport in Carbon Nanotube Pores: Implications for next generation water purification technologies", Authors: Aleksandr Noy, Yun-Chiao Yao, and Xi Chen, World Scientific Publishing Company, 2021. https://doi.org/10.1142/12009

Recent advancements in material fabrication and characterization techniques have promoted an expansion in nanofluidic research, which is related to study of fluidic behavior at the nanometer scale. Several model systems have been created to probe nanofluidic transport behavior and mechanism, even down to sub-nanometer scale. This has enabled the observation of many exotic transport phenomena, significantly different from those observed at the bulk scale, such as a lower water dielectric constant, enhanced water permeability, and exclusive ion selectivity. While many aspects of the physics remain unrevealed, the great potential of nanofluidics for membrane technologies is evident and presents a need for further systematical experimental and theoretical studies. In this chapter, I am going to provide an overview of certain core concepts in nanofluidics. In addition, I will discuss carbon nanotube platforms developed to date and their transport behaviors, which provided a basis for the carbon nanotube porin studies presented later in this dissertation.

1.1 From the Continuum to Molecular Scale

Nanofluidics focus on phenomena that occur in confined spaces at scales of around 1 nanometer (nm). At macroscopic scales (>> 1 nm), fluids are commonly treated as a continuum, meaning that it is considered to completely fill the space it occupies and it distributes continuously throughout the whole region. Physical frameworks including continuum hydrodynamics and electrodynamics laid the foundations for studying fluidic, microfluidic, and even part of nanofluidic behaviors.[1] However, when the length scale goes down to *ca.* 1 nm, it reaches the limit of continuum description and a breakdown of continuum theory occurs (Fig. 1.1).[2] This is because below 1 nm, the length scales being considered are comparable to individual atoms and molecules. For example, the size of water molecules is *ca.* 0.3 nm and the size of hydrated monovalent ions in water is about

0.7 to 1 nm.[3, 4] When studying transport behavior at this scale, individual molecules and any interactions between them become increasingly important. For ionic transport, the Debye length - a characteristic length used when considering electrostatic effects, is about 0.3 to 10 nm; while for water transport, the lip length - a characteristic length used when considering fluidic transport, is no longer considered as zero, but a number ranging up to tens or few hundreds of nanometers. When the model system being used to probe fluidic transport has a size close to the Debye length or much smaller than the slip length, for example with single-digit nanopores (SDNs) at 0.1 to 10 nm range, unique phenomena emerge due to the geometrically confined space.

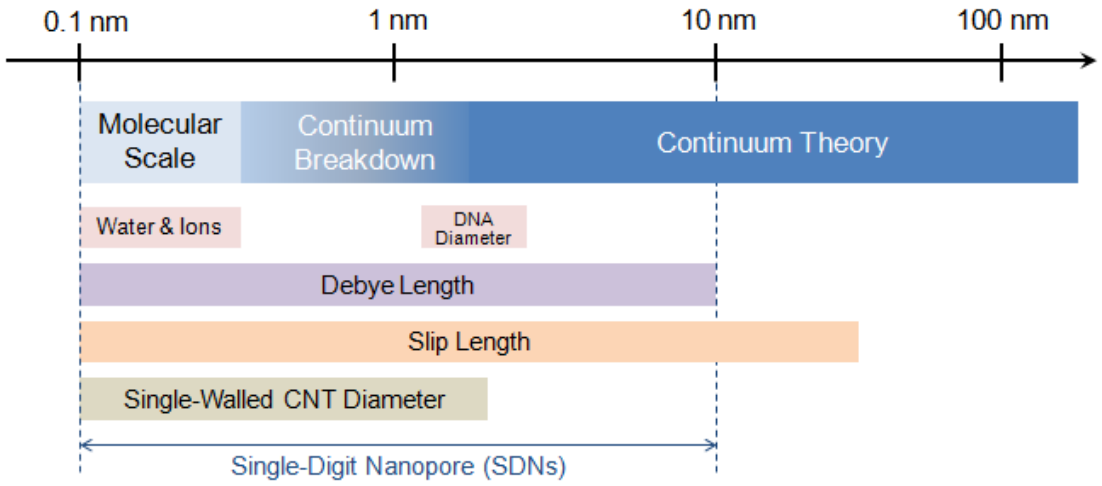

Figure 1.1. Length scale for nanofluidics. Ranging from continuum theory (10 – 100 nm) to molecular scale (0.1 – 1 nm). Water, ions, the diameter of DNA, and the diameter of single-walled carbon nanotubes (SWNTs) are labeled as references for the length scale. Characteristic lengths for fluidic and ions, slip length and Debye length, are labeled as well to understand the physics.

Debye Length

The Debye length (λ_D) is the thickness of the layer of counter-ions attracted to a charged particle in a solution; it is the distance from the charged center to at which the electrostatic potential decreases in magnitude by a factor of 1/e. The Debye length in

electrolyte solution gives an estimate of how far the electrostatic effects of unscreened charges will persist and can be written as:

$$\lambda_D = \frac{1}{\sqrt{8\pi\ell_B c_0}}$$

where c_0 is the concentration of the electrolyte in molar (M) and the Bjerrum length (ℓ_B) is the distance between two charged particles where electrostatic energy is equal to thermal energy, $k_B T$. For monovalent ions in water, ℓ_B is *ca.* 0.7 nm. For the main electrolyte solution used in the work, KCl, the Debye length is *ca.* 0.3 nm at 1 M, *ca.* 1 nm at 100 mM, and *ca.* 3 nm at 10 mM.

Slip Length

Slip length (*b*) is the hydrodynamic term used to describe fluid behavior near a solid surface. It is defined as the depth penetrating into the solid where the projection of the fluid velocity profile equals zero (Fig. 1.2). Under non-slip conditions, the fluid velocity ($v(z)$) at the solid surface is zero relative to the boundary. In slip conditions, the velocity projection penetrates the solid to a depth *b*, the slip length, and so, the velocity at the wall is non-zero. An extreme case of slip length is the perfect slip condition, where slip length is infinite ($b \rightarrow \infty$); this could occur at a frictionless surface where *b* is much larger than the system length scales.

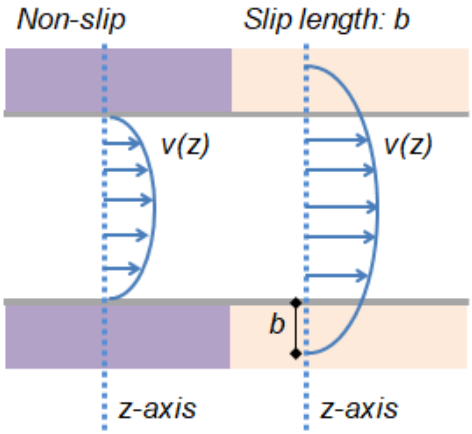

Figure 1.2. Non-slip condition and slip condition with a slip length *b*. Velocity (*v*) is z-axis dependent. Under non-slip conditions, the fluid at the wall has zero velocity.

Single-Chain Water Transport

Fluids are considered disordered compared to solids, but fluid "structures" appear in confined spaces and can give rise to various water packing structures. One extreme variation of these structures is the single-file water chain. This phenomenon leads to the fast water transport rates, faster than one-dimensional diffusion, that can be found in biological protein channels, aquaporins (AQPs).[5, 6, 7] Artificial channels like sub-nanometer carbon nanotubes were also predicted to exhibit this behavior and later proved to have enhanced water flow.[8, 9] It has also been shown that the number of water hydrogen bonds is directly related to water permeability.[6, 9] In an extremely confined space, the number of hydrogen bonds between water molecules reduces from *ca.* 4 in the bulk to *ca.* 2 in a single water chain.[6] This one dimensional hydrogen-bonded water chain provides a great path for proton hopping, which was predicted to give rise to faster proton transport permeability values in theory.[10] In aquaporins, proton hopping is blocked by a water molecule rotation at a specific domain.[7] However, in narrow diameter carbon nanotube porins, the behavior was clearly demonstrated with fast proton transport.[11]

1.2 Applications of Nanofluidics

The breakdown of continuum theory at a nanometer scale leads to special transport phenomena. Many of the unique results observed in nanofluidic studies indicate there is potential to achieve exceptional water transport efficiency and ion selectivity using this technology. These findings could be applied to several applications including desalination, blue energy harvesting, and nanofluidic circuitry. In addition, nanofluidic model systems can serve as a protein channel analog[12] and be used for separation of molecules, such as organic compounds.[13]

Membranes for Desalination

Membrane-based water treatment processes separate water from salts and contaminants by pushing it through tiny selective pores in thin membrane layers. The performance of such membranes depends on their ability to achieve two key goals that are almost diametrically opposed: maximize flow through the pores while maintaining high pore selectivity to ensure the quality of the final product stream. Current polyamide-

based reverse osmosis (RO) membranes rely on a solution-diffusion transport mechanism that is subject to fundamental permeability-selectivity trade-offs, and hence have constrained the performance.[14] Breaking these performance limitations requires a new generation of engineered pores that can potentially support transport mechanisms going beyond solution-diffusion. One successful alternative is provided by the biological membrane water channels, AQPs. The pore size of AQPs is *ca.* 0.3 nm, comparable to water molecules.[6, 7] Within AQPs, a single-file water chain forms along the well-aligned hydrophobic amino acids, providing fast and efficient water flux.[6] Since AQP-based membranes were develop, a number of additional biomimetic membrane systems have been reported, including a recent membrane system based on peptide-appended hybrid[4]arenes which demonstrated extremely high ion selectivity and water permeability.[15] Nevertheless, industrial scale manufacturing for widespread use will likely require a platform that is based on a nano-porous membrane pore that is more robust and scalable. In this regard, artificial nanostructures developed for nanofluidic studies have the potential to be a game changer that break the permeability-selectivity trade-offs of the current polymer membranes to deliver enhanced desalination performance, while simultaneously offering improved stability and scalability.[16]

Blue Energy Harvesting

Reverse electrodialysis (RED) is one approach for providing sustainable, environmentally friendly, and efficient energy sources for our future.[17, 18] RED uses semi-permeable membranes that are highly selective for either cations or anions to separate charged solutes and converts the osmotic potential into voltage difference, thereby generating electrical energy.[17, 18] Harvesting energy by RED is commonly referred to as "blue energy" as salt water from the earth's oceans is an ideal starting material. However, due to the low efficiency of RED, this method remains non-viable for commercial use. Currently, commercially available ion-selective membranes for RED consist of chemically modified 2D nanocomposite materials whose selectivity and resistance are around 95% and 0.5-3 Ω cm^2.[19, 20] To optimize the RED process, new membrane materials that exhibit higher ion selectivity and lower resistance need to be developed.[21]

New developments in nanofluidic systems that enable exclusive cation selectivity over anion promise even further improvements for energy harvesting.[9, 22]

Nanofluidic Circuitry

Charges within the nanochannels significantly alter the ionic distribution and selective ion transport, which can result in ionic current rectification and diode-like or transistor-like behaviors.[9, 23, 24] Due to the physical difference between ions and electrons, fluidic circuitry is not a complete analog of semiconductor microelectronics. However, nanofluidic circuitry, owing to the reduced scale, can be considered much more similar to manipulating electric currents using ion flow. Built-in charges, environmental changes (like altering pH), or external forces (such as applying a gate voltage) could provide controls for regulating molecule flow in confined nanoscale channels, which could further benefit lab-on-a-chip sensing or drug delivery.[23]

1.3 Model Systems to Study Nanofluidics

Well-controlled geometry, size, and chemical properties at nanometer scale are critical factors that must be controlled during systematic studies of nanofluidic phenomena. Emerging top-down and bottom-up fabrication methods provide increased control of nanostructures, which in turn creates improved and various model systems for probing nanofluidic physics. However, not all nanostructures are created equal.[25] Below, I divide model systems by the dimensions of the nanostructure into nanoslits (2D), nanotubes (1D), and nanopores (0D), and briefly introduce example materials, fabrications, and experimental results (Figure 1.3).

Nanoslits

A series of fluidic studies using nanoslits were published by several groups from the University of Manchester, led by the Geim group.[4, 26, 27, 28] In these studies, they took advantage of the crystal structure of 2D materials such as graphite, hBN (hexagonal boron nitride), and MoS_2 (molybdenum disulfide) to fabricate narrow capillaries that acted as 2D channels. This was achieved using few layers or even a single layer of graphene were used as spacers between top and bottom crystals,[26, 28] allowing smooth channels of atomic heights (h) (0.34 nm for single layer and 0.7 nm for two layers of

graphene), with micrometer lengths (*L*) and nanoscale widths (*w*) about 100 nm. Using ionic transport measurements, they demonstrated complete steric exclusion for ions in 0.34 nm nanoslits, with only water and protons showing transport.[28] More surprisingly, they observed an anomalously low dielectric constant of the confined water.[27] The dielectric constant of bulk water is about 80 at room temperature but for the structured water within a confined space, due to decreasing rotational freedom of water dipoles, the dielectric constant reduced down to 2 as determined using scanning dielectric microscopy with the nanoslits.[27]

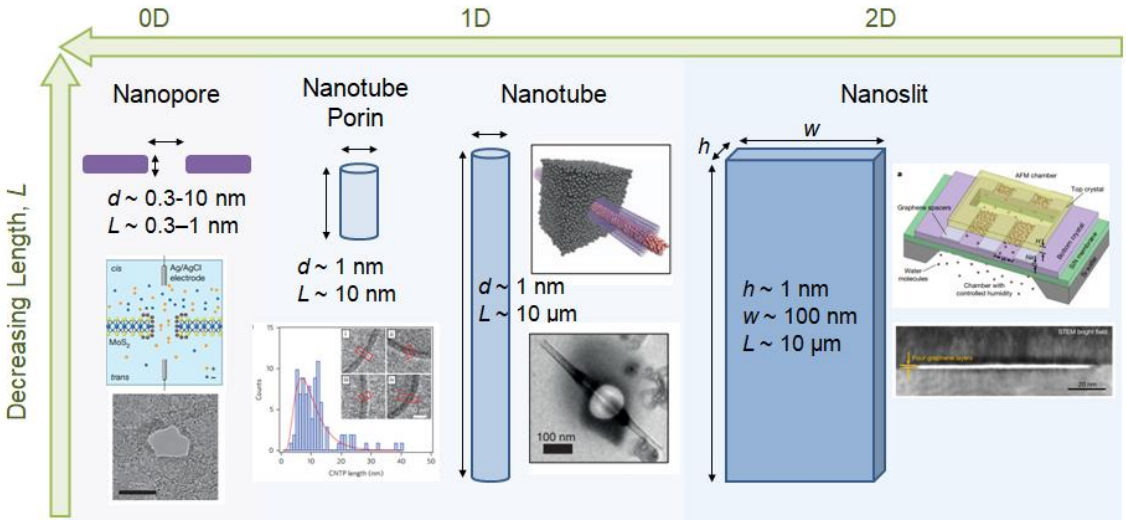

Figure 1.3. Nanostructures commonly used to study nanofluidics: two-dimensional (2D) nanoslits, 1D nanotube, and 0D nanopore. Nanoslits were built from 2D materials like graphite with few layers or single layer of the material as spacers for certain height (*h*) at few nanometer, while width (*w*) and length (*L*) are hundred nanometers and micron, respectively. Nanotube models were mainly boron nitrite tubes or carbon nanotubes with nanometer diameter (d) and micron in length. A special subgroup is nanotube porin, which is ultrashort with length around 10 nm. Nanopores here focus on nanopore in thin 2D materials with pore size less than 10 nm, which are created from focused beam drilling or material defects. Images adapted with permission from ref.[11, 21, 22, 29].

Nanotubes

Nanotubes are cylindrical channels that have a diameter (*d*) in nanometer scale. The length (*L*) of nanotubes can range from microns to nanometers. Commonly used examples of nanotubes are either carbon nanotubes (CNTs) or boron nitride nanotubes (BNNTs). To facilitate nanofluidic measurements, nanotubes can be incorporated into many different systems, including polymer-filled membranes,[30] glass capillary holders,[21, 31] or microfluidic platforms.[32, 33] Using these systems, researchers are able to perform water permeability and ionic transport measurements through the nanotubes while dealing with the challenge that flow could leak between nanotubes and adjacent materials. Ultra-short carbon nanotube porins are a sub-group of nanotubes that *L* equals to *ca.* 10 nm. Owing to the comparable length scales to lipid bilayer thickness,[12, 34] carbon nanotube porins (CNTPs) can mimic protein channels and self-insert into the lipid bilayer, creating a measuring platform similar to that achieved with membrane proteins.[9, 12]

Nanopores

Initial nanopore studies were performed using micro-fabricated silicon-based devices, such as SiN_x (silicon nitrite) membranes. These devices could be fabricated with various nanopore sizes, where both diameter and length could range from tens of nanometers to microns.[35, 36] Recent efforts to achieve zero-dimensional (0D) nanopore systems, where length and diameters are both on the nanoscale, have focused on using 2D materials like graphene and MoS_2 as thin membranes for fabricating pore sizes less than 10 nm. In these systems, nanopores can be formed by focused ion beam drilling,[37] electrical pulse fabrication,[22, 38] or by using the intrinsic defects in 2D materials like hBN (hexagonal boron nitride) or graphene.[39, 40] By suspending these 2D membranes over a SiN_x aperture, it is then possible to study transport through a single nanopore.

Comparing nanoslits, nanotubes, and nanopores, CNTs offer the most variety in a simplistic design owing to their nanometer sized structures which can be tuned by carefully selecting the nanotube chirality. The tunability of diameter coupled with CNTs' cylindrical structure and smooth surface makes CNTs an excellent model system for probing nanofluidics phenomena. In the following sections, I will present various CNT

platforms used to probe nanofluidic behaviors and further discuss the transport results as well as the underlying physics in these systems.

1.4 Carbon Nanotube Platforms

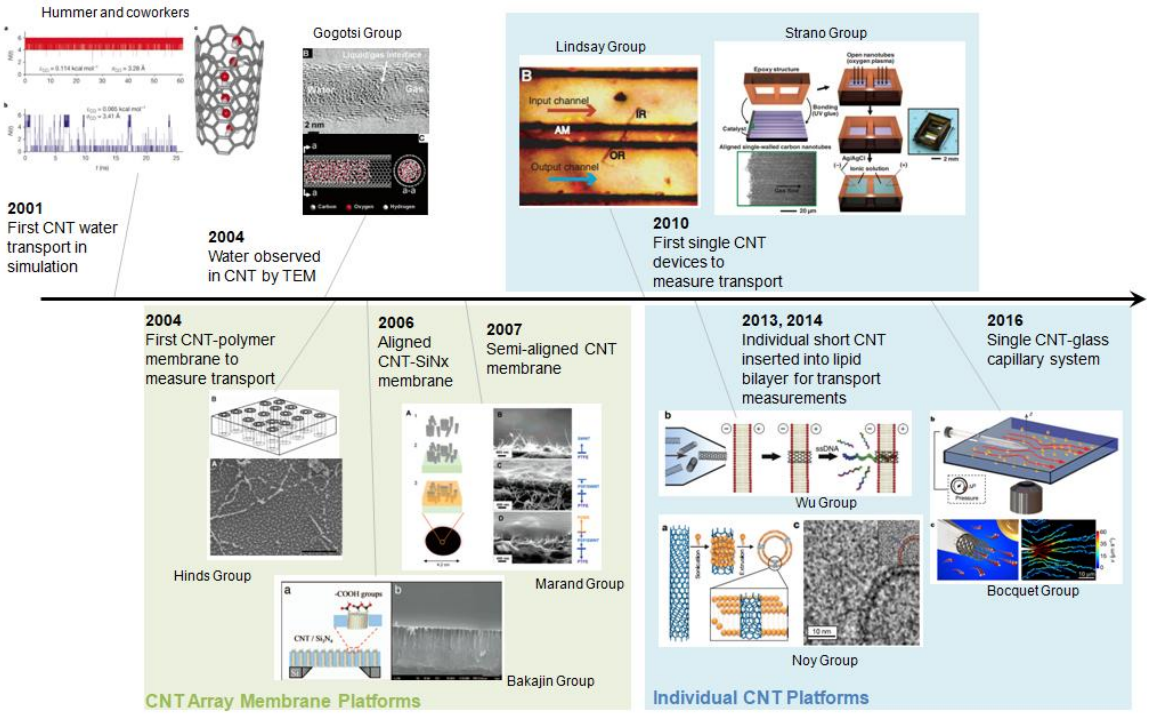

Figure 1.4. The history of CNT platform development for nanofluidic studies. From prediction in simulation to CNT membrane platform and single CNT platform. Images adapted with permission from reference [8, 12, 30, 31, 32, 33, 34, 41, 42, 43]. Copyright© 2001, Macmillan Magazines Ltd. Copyright © 2004, American Chemical Society. Copyright © 2004, American Association for the Advancement of Science. Copyright © 2007, American Chemical Society. Copyright © 2010, American Association for the Advancement of Science. Copyright © 2010, American Association for the Advancement of Science. Copyright © 2013, The Author(s). Copyright © 2014, Nature Publishing Group, a division of Macmillan Publishers Limited. All Rights Reserved. Copyright © 2016, Macmillan Publishers Limited, part of Springer Nature. All rights reserved.

Molecular Dynamic Simulations Prediction

After the discovery of CNTs in 1991,[44] research in this area explosively grew to thousands of articles in 5 years. However, the majority of these articles dealt with synthesis, growth control, or the mechanical and electronic properties of CNTs. Due to

the hydrophobic nature of the CNT interior, few people initially suspected that CNTs could be filled with water or ions. This situation lasted for a decade, but changed abruptly in 2001 when Hummer and coworkers observed that water could fill the 0.81 nm inner cavity of a (6,6) CNT using molecular dynamics (MD) simulations (Fig. 1.4).[8] A particularly striking feature of this simulation was that water inside the CNT cavity changed its arrangement to form a single-file chain, reminiscent of the water arrangement in aquaporin channels.[45] Further analysis also revealed that the enthalpic penalty of losing two hydrogen bonds upon water entry was offset by the narrowed energy state distribution as well as increased rotational entropy of the molecules in the single-file chain.[5]

Applying osmotic pressure to the water-filled nanotube in the simulation revealed an even greater surprise of a nearly friction-less water flow, where the transport was no longer governed by the Hagen-Poiseuille equation.[8] Moreover, subsequent simulations indicated that the barriers to transport were mostly from energy penalties entering and exiting the CNT, and hence relatively independent of the nanotube length.[46] Interestingly, these fast transport predictions were not just limited to just water, and subsequent MD simulations also indicated that proton transport through the one-dimensional water chain should be also faster than bulk water. This was attributed to the single-file water configuration inside the CNT enabling the Grotthuss mechanism which promoted fast proton hopping.[47]

Early experimental observation of water in CNTs

Not long after the seminal simulation by Hummer *et al*., Gogotsi and coworkers experimentally confirmed water filling in CNTs using transmission electron microscopy (TEM).[41] In this work, closed nanotubes, with an inner diameter 2 - 5 nm, were filled with water through sidewall defects during autoclave treatments. The water remained trapped within the CNTs even under TEM vacuum conditions. Internalized water was further confirmed by the crystalline ice peak in the electron energy loss spectroscopy (EELS) data when the sample was cooled to -80 °C. In addition to using TEM or EELS, neutron scattering can also be used to confirm water entry into CNTs. For example, Zanotti and coworkers showed that following exposure to saturated water vapor, most

water molecules preferred to freeze along the interior of the nanotube in an ice-shell and exist as a water-chain structure within 1.4 nm-diameter CNTs.[48] Subsequent work by Mamontov *et al.* also employing neutron scattering, examined the temperature dependence of the confined water and demonstrated that the phase-transition temperature shifts was shifted depending on the CNT diameters.[49] These results clearly demonstrated that water-filling could occur within the narrow CNT channels, presenting them as an attractive material for fabricating synthetic nanochannels and as a system to probe nanofluidic phenomena.

Experimental platforms for observing transport in CNTs

The promising results obtained from computer simulations and experimental results prompted researchers to further investigate water transport in CNTs. The Hinds group won the race to demonstrate mass transport in CNTs. In 2004 they reported that they had fabricated aligned CNT membranes (4.3 ± 2.3 nm diameter) from chemical vapor deposition (CVD)-grown vertically-aligned CNT forests filled with a polymer matrix and successfully observed water and ion transport through these membrane.[30] Subsequent work performed by Holt *et al.* demonstrated fast gas and water transport in aligned 1.6 nm diameter CNT membranes sealed with SiN_x ceramic filling,[42] while the Marand group also came up with an innovative approach to create permeable CNT-membranes by filtering CNTs onto a porous support and sealing this with a polymer.[43]

Aligned CNT membranes, with μm-long nanotube channels, are potentially scalable platforms that could be used for a variety of experiments such as gas flow, pressure-driven water flow, and various electrical measurements. However, a number of significant drawbacks prevented this system from being an ideal model to study fluidic transport within CNTs. One concern remains the purity of the CNTs in the array, which inevitably contain a mixture of different chiralities and diameters due to limitations achieving chirality selective growth. An even larger concern is the presence, and moreover the impact, of point defects along the CNT sidewalls, which could hinder ion transport and water flux. Furthermore, there remain concerns regarding possible leakage from gaps between the aligned CNTs and additional defects that may be formed during the filling of the aligned CNT "forest" with the membrane matrix material. Single CNT

measurement approaches aimed at overcoming these drawbacks were developed between 2010 to 2014, partially as a reaction to the problems associated with aligned CNT membrane platforms.[12, 31, 32, 33]

CNT Array Membrane Platforms

The Hinds group embedded polystyrene (PS) between a multi-walled CNT (MWNT) array in their initial demonstrate.[30] Dense, vertically-aligned MWNT arrays were grown on quartz substrates using the CVD method and gaps between nanotubes were filled with PS solution by a spin-coating. The high wetability of CNTs by PS results in complete infiltration of the PS into the spaces between the CNT array. Top and bottom substrates were removed by etching and CNTs were opened using H_2O plasma oxidation, resulting in a freestanding CNT membranes, with a thickness of *ca.* 5 – 10 μm and inner pore sizes of 4.3 ± 2.3 nm. The Hinds group further demonstrated that these membranes could be chemically modified at the pore mouth to introduce different functional groups.[30]

CNT membranes with pore sizes < 2 nm were first fabricated by Holt *et al.* using a vertically aligned double-walled carbon nanotube array that was grown on a silicon chip surface. Encapsulation with CVD-deposited silicon nitride (Si_3N_4) resulted in a composite that could subsequently be opened by plasma etching to produce a thin membrane.[42, 50] This fabrication procedure produced rather thin and fragile, micron-sized CNT membrane patches. However, these membranes were nonetheless able to withstand over 1 atm pressure gradient during the measurements. A more recent study from the Park group used a similar design, but instead incorporated single-walled carbon nanotube (SWNT) arrays. In this study, a titanium dioxide (TiO_2) coating was deposited using atomic layer deposition (ALD).[51, 52] A key fabrication step involved opening the CNT ends by argon ion-beam-milling. Crucially, this etching step also served as a quality control step: the etching was stopped once gas flow through the membrane reached a constant value and stopped increasing after further etching, confirming that all CNT pores were open. This ensured that further etching did not result in the creation of any additional defect-based leaks in the membrane.[52]

Despite the many advantages of the CNT ‘forest’ membranes, researchers remained fundamentally limited in pore size by the diameter of the CNTs that could be grown in

vertically aligned synthesis. An early attempt to overcome this was introduced by the Marand group in 2007: a hybrid CNT platform that featured semi-aligned CNTs in a polymer membrane.[43] CNTs were first treated with acids to open the end tips and cut the nanotubes into small lengths. Treated CNT solution were filtered through a porous membrane, which created semi-aligned CNTs on the support membrane owing to a self-assembly mechanism that was directed by the shear forces of the flow. The CNT membranes were later coated with polymers such as PDMS. This resulted in thin-film CNT/polymer nanocomposite membranes where the CNTs protruded from the top of the membranes. The researchers further demonstrated that these membranes were capable of achieving similar gas separation and water filtration properties to the nanotube forest membranes grown by CDV.[43, 53] The Hinds group also developed a CNT membrane platform based on microtomed slices of an epoxy resin block filled with randomly oriented long carbon nanotubes,[54] where sufficiently long CNTs were able to span the cross-section of the membrane and form well-defined pores. A key advantage of these hybrid techniques was that they alleviated researchers from the limitation of CNT pore sizes imposed by the vertically-aligned CNT "forest" synthesis method and enabled them to use smaller diameter pores. However, these strategies were not without drawbacks and typically suffered from inherently low pore densities that placed severe limitations on their functionality.

Individual CNT Platforms

One of the first individual CNT measurement platforms was introduced by Lindsay and co-workers in 2010.[32] This measurement device was fabricated by using individual 1-2 nm diameter CNTs, grown by ethanol vapor CVD on a Si wafer, to connect two fluid reservoir channels which were created using e-beam lithography. The CNT ends were removed by O_2 plasma etching before the device was sealed. 20% of the devices fabricated using this approach showed relatively large ion current, indicating that the CNT channel was open and that ions were being conducted through the CNT. Researchers were also able to observe electrophoretic transport of single-stranded DNA in this system.

The Strano group also reported a platform that enabled measuring ion transport through individual or a small number of CNTs in 2010.[33] To fabricate these CNT devices, they seeded catalyst nanoparticles at a substrate edge and grew very long aligned CNTs using a CVD process.[55] Sections of the nanotubes were protected using lithographically-defined masks and the remainder was etched away and opened by oxygen plasma. These were then connected to two microfabricated fluid reservoirs. Measurements using this platform first focused on electrical potential-driven ion transport.[33, 56, 57] Subsequently, a similar device platform was used to monitor water transport using Raman spectrum peak shifts, where a shift of the RBM region peak indicated the existence of a continuous water phase inside a nanotube.[58]

Another iconic single nanotube platform was demonstrated by the Bocquet group, where a glass nanocapillary/nanotube combination (nanojet) was used to study nanofluidics behavior in CNTs and BNNTs.[21, 31] To fabricate the nanojet setup, a single, long CNT protruding from a CNT forest was picked up using a tungsten tip. This tube was glued to the tip and then carefully maneuvered into the orifice of a glass nanocapillary at which point local electron beam-induced naphthalene deposition was used to seal the gap between the CNT and the capillary wall. This CNT bridged two reservoirs: one inside the capillary and one into the fluid chamber which the capillary was placed. All fabrication steps were performed in an SEM to ensure that there was well-controlled pressure and position alignment. In this work, researchers examining several different CNTs with diameter ranges from 7 nm to 100 nm and lengths of several hundred nanometers. This platform turned out to be surprisingly versatile, enabling electrophoretic ion transport experiments[31, 59] as well as pressure-driven water transport measurements, which utilized 500 nm polystyrene tracer particles and tracked the motion of these particles to map the flow velocity.[31] Works by the Nuckolls group also created isolated single-walled CNT devices using a CNT channel suspended in a polymer matrix that bridged two reservoirs, which they could use to measure DNA translocation and ion transport through the channel.[60] The Jourdain group fabricated similar devices to study electrophoretic ion transport, but used several individual CNTs with diameters in the range of 1 - 2 nm instead of one single CNT .[61]

Single CNT Platform: Carbon Nanotube Porins

Work by our group (the Noy group) and the Wu group between 2013 - 2014 developed an alternative strategy for measuring water and ion transport in CNT channels.[12, 34] In these platforms, carbon nanotube porins (CNTPs), ultrashort CNTs 10 - 20 nm in length embedded in lipid or polymer membranes, emulate membrane channels, such as AQPs.[12, 62, 63] To fabricate CNTPs, commercially available, long CNTs were cut by ultrasonication into much shorter pieces.[62] This procedure was compatible with CNT stocks of different diameters, enabling the production of CNTPs with different pore sizes. Specifically, work in our group examined CNTPs with 0.8 and 1.5 nm diameter, allowing direct comparison of transport efficiency between channels with the same geometry but different pore sizes. Another key advantage of this biomimetic platform was that it allowed direct adoption of a number of protocols that were developed for measuring water and ion transport in biological membrane channels, including lipid vesicle and planar lipid bilayer platforms.[9, 11, 16, 64]

1.5 Water Transport in CNT Channels

The macroscopic laws of hydrodynamics, defined by the Hagen–Poiseuille equation, govern flow in conventional fluidic channels. From the very first simulations that predicted fast flow in carbon nanotubes it was clear that the continuum description would not be applicable in these nanoscale systems.[8, 46] In addition, the smooth hydrophobic surface of CNTs is inherently a low friction interface, which conventionally means a very large slip length,[31, 65] however Hagen-Poiseuille equation assumes a non-slip condition at the interface. In extreme cases, when the slip length is much larger than the channel diameter, the boundary is essentially shear-free, making the Hagen-Poiseuille equation invalid. In pioneering work from the Aluru group, it was shown that continuum flow theory was valid for CNTs with 10 nm diameter, but broke down in smaller diameter (0.95 nm) nanotubes.[66] One of the principal reasons why conventional hydrodynamics breaks down in the smallest CNT pores with diameters below 1 nm is that those pore sizes squeeze water molecules down into a single-file configuration, drastically altering the hydrogen bonding pattern compared to in continuum bulk water

arrangement.[8, 9, 11] Subsequent work by the Aluru group (Fig. 1.5) also demonstrated how the nature of the channel surface impacts the flow inside a nanotube. Among nanotubes of similar diameters, CNTs exhibited the highest water velocity and flux, compared to BNNTs, hydrophilic silicon nanotubes (NT Si), and hypothetical CNTs with computationally-engineered rough surface.[67] The study concluded that the origin of the remarkable flux enhancement in CNTs was a combination of the smoothness of the CNT surface and its hydrophobicity, which further reduced the interactions between the water molecules and the nanotube surface.

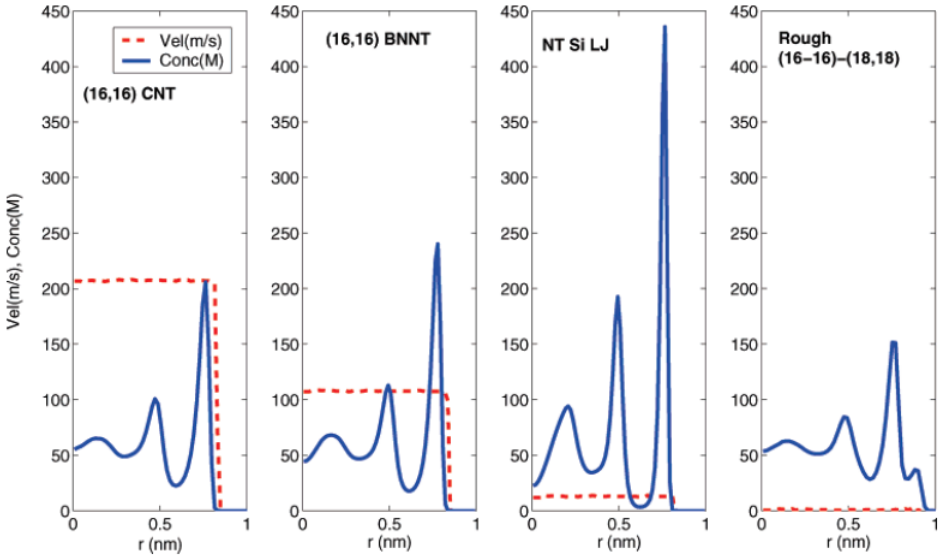

Figure 1.5. MD simulation of water velocity (red dash line) **and water density** (blue line) **profiles** as a function of the radius from the center of a (16, 16) CNT, (16, 16) BNNT, (16, 16) nanotube with silicon, and a rough surface (16, 16)/(18, 18) CNT combination. Images adapted with permission from reference [67]. Copyright © 2008, American Chemical Society.

The first experimental demonstrations of high water flux enhancement in CNT pores were reported shortly after the publication of the first computational predictions when the Hinds group demonstrated high rates of water transport through aligned MWNT membranes with pore size *ca.* 7 nm. They reported remarkably long slip lengths,[65] indicating an increase in water permeability of more than four orders of magnitude compared to the predictions from the Hagen-Poiseuille equation. Furthermore, the

permeability of solvents through the MWNT membranes decreased as the solvents became more hydrophobic, re-emphasizing that it was not only the smoothness of the CNT surface but also the hydrophobic nature that was responsible for the high water velocity. Holt *et al.* also reported water fluxes exceeding those calculated by continuum hydrodynamics models by more than three orders of magnitude in aligned < 2-nm CNT membranes under pressure-driven flow conditions.[42] More recent work by the Park group also demonstrated that these high water fluxes could be observed for osmotic water and salt transport across CNT membranes in a forward osmosis (FO) setup.[52]

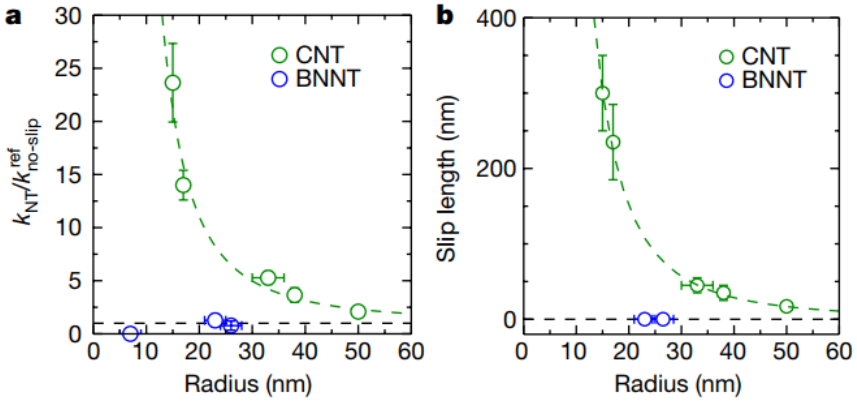

Figure 1.6. Water permeability and slip length of individual CNTs and BNNTs derived from the nanojet measurements. (**a**) Normalized permeability and (**b**) slip length of tubes as a function of nanotube radius. The horizontal dash lines indicate the no-slip prediction. Images adapted with permission from reference [31]. Copyright © 2016, Macmillan Publishers Limited, part of Springer Nature. All rights reserved.

Measurements of water-filling and water-flow in individual CNT pores revealed an even more complicated physical picture. Experiments from the Strano group showed evidence of phase transitions between ice, liquid water, and gas phase water in CNTs near room temperatures,[58] providing experimental evidence for water behavior that was previously predicted in MD simulations.[68] The Bocquet group demonstrated that their "nanojet" platform could be used to observe exceptionally high water transport rates directly in individual CNTs.[31] Remarkably, these measurements (Fig. 1.6) showed that the values of the slip length became divergent as the diameter of CNTs became smaller

and started to approach the "single-digit nanopore" regime (when d < 10 nm). In contrast, BNNTs of similar diameters showed very small slip length values. This was because, compared to CNTs, BNNTs have a much more charged surface, which interacts with strongly water molecules and significantly slows down the water flow through the tube.

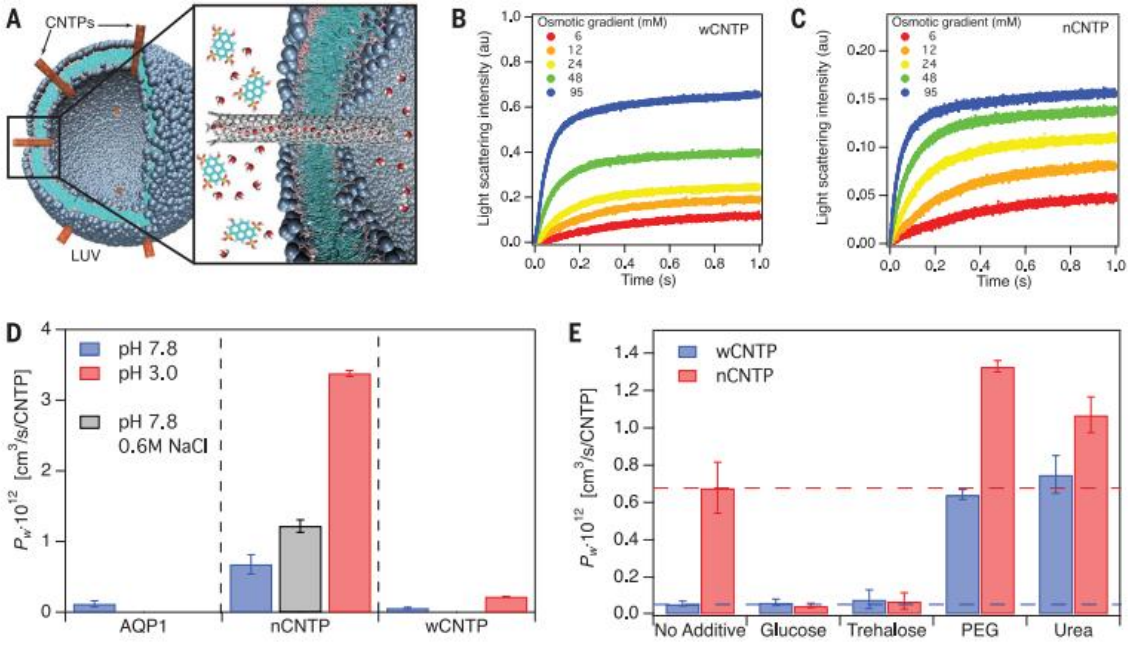

Figure 1.7. Water transport through 0.8 nm and 1.5 nm diameter CNTPs. (**A**) Sketch of CNTP in the lipid vesicle platform for water flux measurements under osmotic pressure. (**B**, **C**) Light scattering traces for lipid vesicle with CNTPs under various osmotic gradients. (**D**) Water permeability for 0.8 nm and 1.5 nm diameter CNTPs at pH 7.5 and pH 3.0, compared with AQP-1. (**E**) Water permeability changes with additives, which change water structure of water. Images adapted with permission from reference [9]. Copyright © 2017, The American Association for the Advancement of Science.

Another interesting comparison could be made with the water transport in AQPs. Very narrow (*ca.* 0.3 nm) AQP channels, which are lined mostly with hydrophobic residues, exhibit extremely fast water transport and are considered the gold standard of membrane water channels. Work from our group compared water transport in two types of CNTPs (diameters of 0.8 and 1.5 nm) to that in AQPs.[9] While the 1.5 nm diameter

CNTP showed bulk water-like transport with the fluxes significantly lower than that of the AQP-1 protein channels, the 0.8 nm diameter CNTP showed enhanced water flow rates that even exceeded those of AQP-1 (Fig. 1.7).[9, 16] This remarkably strong performance was attributed to a combination of several factors. Narrow diameter CNTPs benefit from the same physical phenomena that enhance water transport in wider CNTPs: the smoothness of the tube walls and their hydrophobic character. However, in addition to this, 0.8 nm CNTPs force water into a single-file configuration where a chain-like hydrogen bonding pattern leads to a further enhancement of water transport efficiency.[9] For water transport, the combination of single-chain water configuration and the hydrophobic, smooth walls of the CNTs results in enhanced permeability through the confined channel spaces.

1.6 Ion Transport in CNT Channels

A number of physical attributes determine the ion selectivity of nanochannels: the size of the pore mouth, a requirement for partial solute dehydration upon entry into the pore, and electrostatic exclusion due to the charges present at the pore mouth or along the pore surface (Fig. 1.8). The constant diameter of CNT pores means that their size exclusion properties are fairly straightforward. Holt *et al.* demonstrated that 2 nm gold colloids could be excluded from aligned double-wall carbon nanotube membranes with a pore size < 2 nm.[42] However, the diameters of carbon nanotubes are *a-priori* still too large to exclude all ions based simply on their ionic radii. This situation becomes very different when considering the hydrated radii of the ions, making the energy costs associated with partial ion dehydration upon entry into the carbon nanotube pore another powerful mechanism for controlling ion selectivity.[69] Electrostatic repulsion is potentially another powerful mechanism for conveying selectivity to the CNT pores. Generally, the range and impact of electrostatic effects is highly dependent on the electrostatic screening due to the presence of mobile charges in solution, which is described by the Debye length. Specifically, when the Debye length of the electrolyte is larger than the radius of the nanopore with charged ends or walls, the electric fields overlap and create a barrier to free ion passage. As the ion concentration increases and the Debye length drops, the

electric fields contract and create an opening through which certain ions can pass. Indeed, the effect of decreasing ion selectivity at higher ion concentration was observed experimentally for both aligned carbon nanotube membranes and carbon nanotube porin experimental platforms.[9, 64, 70] For most nanostructure systems, the ionic transport could be described by these three mechanisms (Fig. 1.8).

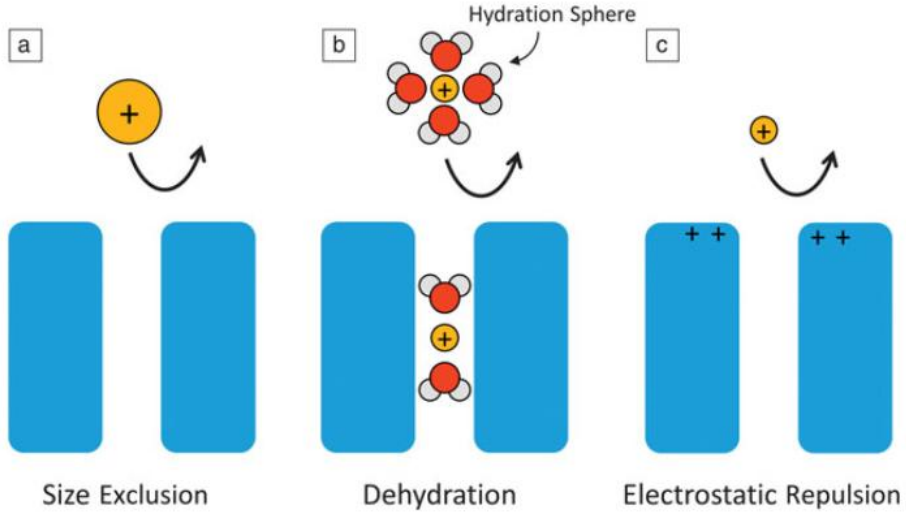

Figure 1.8. Mechanisms of ion selectivity and rejection for a nanochannel. (**a**) size exclusion, (**b**) dehydration barriers, and (**c**) electrostatic interactions. Images adapted with permission from reference [71]. Copyright © Materials Research Society 2017.

The first observation of ion transport through CNT pores was reported by the Hinds group using aligned nanotube membranes,[30] where they observed the diffusion of $Ru(NH_3)_6^{3+}$ ions across their membranes. The same work demonstrated the possibility of using size exclusion/steric hindrance mechanism to modulate $Ru(NH_3)_6^{3+}$ ion flux by showing reduced transport in nanotubes where the CNT pore entrances were functionalized with biotin-streptavidin complex.[30] Fornasiero *et al.* studied the transport behavior of a variety of ionic compounds through smaller (1.6 nm) diameter aligned CNT membranes using pressure-driven reverse osmosis experiments. In these experiments, they observed that salt rejection in these pores strongly depended on the species tested, ranging from almost 100% for $K_3Fe(CN)_6$ (complete rejection) to very low levels

rejection for $CaCl_2$.[70] The degree of rejection was also found to be strongly dependent on the overall ionic strength of the solution, with cation rejection in KCl solutions ranging from 41% at low ion concentration to *ca.* 0% at high concentration. These results provided clear evidence that Donnan model was appropriate for describing the ion rejection in CNT pores of this size.[70] Subsequent work traced the origin of this selectivity to the presence of charged COO^- groups at the rim of the CNT pores.[72] Interestingly, the Marand group reported that membranes incorporating CNTs functionalized with chain-like zwitterion molecules rejected essentially all ions, giving a 98.6% rejection rate with NaCl.[53] The high levels of rejection were attributed to both size exclusion (from the bulky functional groups) and electrostatic repulsion (from the multiple charges) effects.

Experimental observations of ion transport in individual CNT channels took comparatively longer, with the first reports appearing in 2010.[32, 33] In these earlier studies, researchers from several groups opted to use ultra-long CNTs incorporated into different microfluidic device platforms. Lindsay and coworkers used one such platform to probe electrophoretic current through single SWCNTs and reported measured current values greatly exceeding that estimated based on the CNT diameter and KCl bulk solution conductivity.[32, 73] This enhancement was interpreted as further evidence for friction-less transport inside of CNT pores. Additionally, this work noted that metallic CNTs exhibited larger ion current versus their semiconducting counterparts.[73] The Strano group investigated similar devices and reached a radically-different conclusion; they observed that the current through their devices, which incorporated *ca.* 1.5 nm diameter and 500 μm long CNTs, was largely from protons.[33, 57] Moreover, this group observed that alkali metal ions could act as current blockers and create regular current oscillation in their device's response.[33] A further systematic study of various CNTs, with diameters ranging from 0.94 to 2.01 nm, showed that dwell times and blocking currents were diameter dependent and that CNTs with a diameter around 1.58 nm displayed the largest blocking current.[57]

More recently, a number of measurements have examined ion and proton transport in individual CNT channels with lengths ranging from several micrometers[59] to ultra-short (10 nm) CNTPs.[9, 11, 64, 74] A study from our group reported ultra-fast proton

transport in 0.8 nm diameter CNTPs due to the single-file water arrangement inside that channel promoting proton transport via the Grotthuss hopping mechanism,[10, 11] confirming earlier MD simulations predictions.[47] Results from the Bocquet group showed an intriguing dependence of conductance of MWNTs on salt concentration.[59] When examining KCl transport in MWNTs (7 nm, 20 nm, 28 nm, or 70 nm in diameter), all MWNTs showed conductance scaling that transitioned from approximately linear at high salt concentrations to 1/3 power law at low salt concentrations. The explanation provided by Secchi *et. al.* relied on an elegant model that assumed that the CNT inner surface carried some negative charges due to adsorption of the OH^- groups. This adsorption process, in turn, was subject to charge regulation at varying ionic strengths, with a combination of this charge regulation and preferential accumulation of the counterions inside the channel producing the observed 1/3 power law scaling of the ion conductance. However, many questioned the validity of this model as there was no direct evidence for the OH^- ions adsorption on the CNT surfaces and any such adsorption could potentially interfere with the fast transport and high water flux commonly observed in the CNT pores.

The 1/3 power law presented by Secchi *et. al.* turned out to not be a universal scaling law for CNT pores. The Nuckolls group reported non-linear concentration scaling for ion transport in 1.5 nm diameter CNT pores which followed a 1/2 power law.[60] They attributed the observed effects to the charge regulation of the COO^- groups at the pore entrances. We reported an even richer set of behaviors for CNTPs of different diameters. For ultra-narrow, 0.8 nm diameter CNTPs, the ion conductance initially followed the 1/2 exponent power law and then saturated at higher ionic strengths,[9] mimicking the behavior of small diameter biological ion channels.[75] On the other hand, ionic conductance in larger-diameter, 1.5 nm CNTPs followed a 2/3 power law and no saturation at high ion concentrations.[64] Extensive modeling efforts by several groups have clarified some of the origins of these rich set of scaling behaviors. Biesheuvel and Bazant extensively analyzed how a solution to the Poisson-Nernst-Planck equations, in combination with charge regulation, can describe some of the scaling laws observed in experiments.[76] In particular, they proposed that the 1/2 power law could be evidence of the conductance following the "good co-ion exclusion" limit where the nanotube pore becomes exclusively selective to

one kind of ion. Manghi and coworkers added another layer of complexity to the model by accounting for the possibility of strong fluid slip along the nanotube pore walls.[77] Building on these interpretations, our group in collaboration with the Aluru group rationalized the observation of the 2/3 power law scaling in larger diameter CNT pores and attributed it to extremely strong electroosmotic coupling within these channels.[64] More details of CNTP ionic transport are discussed in Chapter 2 and 3.

The Strano group, Nuckolls group and our (Noy) group have all reported that CNT pores with negatively charged COO^- groups at the ends show preferential cation selectivity. The Nuckolls group compared the transport of KCl and $K_3(Fe(CN)_6)$ in 1.5 nm diameter CNTs and reported negligible effects on ion transport; however, when they replaced potassium with a bigger cation, tris(bipyridine)ruthenium(II), $[Ru(bpy)_3]^{2+}$, they observed a significant reduction in conductance, which they attributed to the increased ion rejection of the larger cation at the nanotube entrance.[60] Our group has performed extensive characterization of CNTP ion selectivity using reversal potential measurements in single CNTP conductance experiments.[9, 64] In these experiments, CNTPs with a 0.8 nm diameter showed near-perfect cation selectivity, which only started to decrease at very high ionic strength (*ca.* 1 M KCl, > 600 mM KCl which is the salinity levels of seawater). This observation was remarkable as it indicated that at small enough diameters CNTPs could exhibit monovalent salt rejection that was sufficient for seawater desalination application. Unsurprisingly, larger 1.5 nm diameter CNTPs did not exhibit the same degree of ion selectivity and instead showed much weaker cation selectivity, with a permselectivity (the selectivity of cation over anion, the permselectivity value for a cation-exclusive channel is 1) value of around 0.5.[64] When the COO^- groups at the CNTP ends were neutralized by lowing the pH to 3, the selectivity further reduced as indicated by permselectivity dropping down to zero.[64] Additional information on CNTP channel selectivity are presented in Chapter 2 and 3.

Overall, despite the significant progress in elucidating the mechanisms for ion selectivity in CNTs, our understanding remains incomplete. For example, experimental data on CNTP conductance showed linear I-V curves for even the smallest 0.8 nm pores, indicating that the barrier for entry into these tubes for at least the majority carrier species

is quite low.[9] This observation directly contradicts the results from classical MD simulations that showed ion entry into a small diameter CNT pore required energy costs associated with partial dehydration of the ion solvation shell.[78] A more complicated questions that remains unanswered is whether the partial desolvation and strong degree of confinement can induce any unusual differential selectivity effects or correlated transport effects. Additionally, we still do not have a good understanding of surface charge regulation on CNT walls and how this may govern the ionic conductance trends.

In this dissertation, I present the work I completed during my PhD on using CNTPs as a model system to probe nanofluidic ion transport. These results demonstrate an established model that gives an opportunity to study the unique transport behavior and reveal the underlying transport physics in nanofluidics systems. Details on the synthesis and characterization of CNTPs, as well as information on the setups and devices used for ionic measurements are introduced in Chapter 2. The ionic transport behavior and physics of 0.8 nm diameter CNTPs (nCNTPs) are also discussed in Chapter 2, while details about 1.5 nm diameter CNTPs (wCNTPs) are presented in Chapter 3. In Chapter 4, a modeling study investigating the effect of adding a gate voltage control to our CNTP device is discussed. Finally, in Chapter 5, I include an outlook for using the CNTP model system presented within this dissertation to further probe the field of nanofluidics and advance the applicability of this technology. Overall, our CNTPs represent a versatile nanofluidic model system that we can utilize to advance the understanding and control of ion and water behavior at nanoscale.

References

1. Bocquet, L.; Charlaix, E., Nanofluidics, from bulk to interfaces. *Chem. Soc. Rev.* **2010,** *39*, 1073.
2. Kavokine, N.; Netz, R. R.; Bocquet, L., Fluids at the nanoscale: From continuum to subcontinuum transport. *Annu. Rev. Fluid Mech.* **2021,** *53*, 377.
3. Marcus, Y., Ionic radii in aqueous solutions. *Chem. Rev.* **1988,** *88*, 1475.
4. Esfandiar, A.; Radha, B.; Wang, F. C.; Yang, Q.; Hu, S.; Garaj, S.; Nair, R. R.; Geim, A. K.; Gopinadhan, K., Size effect in ion transport through angstrom-scale slits. *Science* **2017,** *358*, 511.
5. Horner, A.; Pohl, P., Single-file transport of water through membrane channels. *Faraday Discuss.* **2018,** *209*, 9.

6. Horner, A.; Zocher, F.; Preiner, J.; Ollinger, N.; Siligan, C.; Akimov, S. A.; Pohl, P., The mobility of single-file water molecules is governed by the number of H-bonds they may form with channel-lining residues. *Sci. Adv.* **2015,** *1*, e1400083.
7. de Groot, B. L.; Grubmuller, H., Water permeation across biological membranes: mechanism and dynamics of aquaporin-1 and GlpF. *Science* **2001,** *294*, 2353.
8. Hummer, G.; Rasaiah, J. C.; Noworyta, J. P., Water conduction through the hydrophobic channel of a carbon nanotube. *Nature* **2001,** *414*, 188.
9. Tunuguntla, R. H.; Henley, R. Y.; Yao, Y. C.; Pham, T. A.; Wanunu, M.; Noy, A., Enhanced water permeability and tunable ion selectivity in subnanometer carbon nanotube porins. *Science* **2017,** *357*, 792.
10. Wraight, C. A., Chance and design--proton transfer in water, channels and bioenergetic proteins.
11. Tunuguntla, R. H.; Allen, F. I.; Kim, K.; Belliveau, A.; Noy, A., Ultrafast proton transport in sub-1-nm diameter carbon nanotube porins. *Nat. Nanotechnol.* **2016,** *11*, 639.
12. Geng, J.; Kim, K.; Zhang, J.; Escalada, A.; Tunuguntla, R.; Comolli, L. R.; Allen, F. I.; Shnyrova, A. V.; Cho, K. R.; Munoz, D.; Wang, Y. M.; Grigoropoulos, C. P.; Ajo-Franklin, C. M.; Frolov, V. A.; Noy, A., Stochastic transport through carbon nanotubes in lipid bilayers and live cell membranes. *Nature* **2014,** *514*, 612.
13. Qu, H.; Rayabharam, A.; Wu, X.; Wang, P.; Li, Y.; Fagan, J.; Aluru, N. R.; Wang, Y., Selective filling of n-hexane in a tight nanopore. *Nat. Commun.* **2021,** *12*, 310.
14. Elimelech, M.; Phillip, W. A., The future of seawater desalination: energy, technology, and the environment. *Science* **2011,** *333*, 712.
15. Song, W.; Joshi, H.; Chowdhury, R.; Najem, J. S.; Shen, Y. X.; Lang, C.; Henderson, C. B.; Tu, Y. M.; Farell, M.; Pitz, M. E.; Maranas, C. D.; Cremer, P. S.; Hickey, R. J.; Sarles, S. A.; Hou, J. L.; Aksimentiev, A.; Kumar, M., Artificial water channels enable fast and selective water permeation through water-wire networks. *Nat. Nanotechnol.* **2020,** *15*, 73.
16. Li, Y.; Li, Z.; Aydin, F.; Quan, J.; Chen, X.; Yao, Y. C.; Zhan, C.; Chen, Y.; Pham, T. A.; Noy, A., Water-ion permselectivity of narrow-diameter carbon nanotubes. *Sci. Adv.* **2020,** *6*.
17. Pattle, R. E., Production of Electric Power by Mixing Fresh and Salt Water in the Hydroelectric Pile. *Nature* **1954,** *174*, 660.
18. Loeb, S., Osmotic Power-Plants. *Science* **1975,** *189*, 654.
19. Hong, J. G.; Zhang, B. P.; Glabman, S.; Uzal, N.; Dou, X. M.; Zhang, H. G.; Wei, X. Z.; Chen, Y. S., Potential ion exchange membranes and system performance in reverse electrodialysis for power generation: A review. *Journal of Membrane Science* **2015,** *486*, 71.
20. Logan, B. E.; Elimelech, M., Membrane-based processes for sustainable power generation using water. *Nature* **2012,** *488*, 313.
21. Siria, A.; Poncharal, P.; Biance, A. L.; Fulcrand, R.; Blase, X.; Purcell, S. T.; Bocquet, L., Giant osmotic energy conversion measured in a single transmembrane boron nitride nanotube. *Nature* **2013,** *494*, 455.

22. Feng, J.; Graf, M.; Liu, K.; Ovchinnikov, D.; Dumcenco, D.; Heiranian, M.; Nandigana, V.; Aluru, N. R.; Kis, A.; Radenovic, A., Single-layer MoS2 nanopores as nanopower generators. *Nature* **2016,** *536*, 197.
23. Guan, W.; Fan, R.; Reed, M. A., Field-effect reconfigurable nanofluidic ionic diodes. *Nat. Commun.* **2011,** *2*, 506.
24. Daiguji, H.; Oka, Y.; Shirono, K., Nanofluidic diode and bipolar transistor. *Nano Lett.* **2005,** *5*, 2274.
25. Faucher, S.; Aluru, N.; Bazant, M. Z.; Blankschtein, D.; Brozena, A. H.; Cumings, J.; Pedro de Souza, J.; Elimelech, M.; Epsztein, R.; Fourkas, J. T.; Rajan, A. G.; Kulik, H. J.; Levy, A.; Majumdar, A.; Martin, C.; McEldrew, M.; Misra, R. P.; Noy, A.; Pham, T. A.; Reed, M.; Schwegler, E.; Siwy, Z.; Wang, Y.; Strano, M., Critical knowledge gaps in mass transport through single-digit nanopores: A review and perspective. *J. Phys. Chem. C* **2019,** *123*, 21309.
26. Radha, B.; Esfandiar, A.; Wang, F. C.; Rooney, A. P.; Gopinadhan, K.; Keerthi, A.; Mishchenko, A.; Janardanan, A.; Blake, P.; Fumagalli, L.; Lozada-Hidalgo, M.; Garaj, S.; Haigh, S. J.; Grigorieva, I. V.; Wu, H. A.; Geim, A. K., Molecular transport through capillaries made with atomic-scale precision. *Nature* **2016,** *538*, 222.
27. Fumagalli, L.; Esfandiar, A.; Fabregas, R.; Hu, S.; Ares, P.; Janardanan, A.; Yang, Q.; Radha, B.; Taniguchi, T.; Watanabe, K.; Gomila, G.; Novoselov, K. S.; Geim, A. K., Anomalously low dielectric constant of confined water. *Science* **2018,** *360*, 1339.
28. Gopinadhan, K.; Hu, S.; Esfandiar, A.; Lozada-Hidalgo, M.; Wang, F. C.; Yang, Q.; Tyurnina, A. V.; Keerthi, A.; Radha, B.; Geim, A. K., Complete steric exclusion of ions and proton transport through confined monolayer water. *Science* **2019,** *363*, 145.
29. Yang, Q.; Sun, P. Z.; Fumagalli, L.; Stebunov, Y. V.; Haigh, S. J.; Zhou, Z. W.; Grigorieva, I. V.; Wang, F. C.; Geim, A. K., Capillary condensation under atomic-scale confinement. *Nature* **2020,** *588*, 250.
30. Hinds, B. J.; Chopra, N.; Rantell, T.; Andrews, R.; Gavalas, V.; Bachas, L. G., Aligned multiwalled carbon nanotube membranes. *Science* **2004,** *303*, 62.
31. Secchi, E.; Marbach, S.; Nigues, A.; Stein, D.; Siria, A.; Bocquet, L., Massive radius-dependent flow slippage in carbon nanotubes. *Nature* **2016,** *537*, 210.
32. Liu, H.; He, J.; Tang, J.; Pang, P.; Cao, D.; Krstic, P.; Joseph, S.; Lindsay, S.; Nuckolls, C., Translocation of single-stranded DNA through single-walled carbon nanotubes. *Science* **2010,** *327*, 64.
33. Lee, C. Y.; Choi, W.; Han, J. H.; Strano, M. S., Coherence resonance in a single-walled carbon nanotube ion channel. *Science* **2010,** *329*, 1320.
34. Liu, L.; Yang, C.; Zhao, K.; Li, J.; Wu, H.-C., Ultrashort single-walled carbon nanotubes in a lipid bilayer as a new nanopore sensor. *Nat. Commun.* **2013,** *4*, 2989.
35. Dekker, C., Solid-state nanopores. *Nat. Nanotechnol.* **2007,** *2*, 209.
36. Lin, K.; Lin, C. Y.; Polster, J. W.; Chen, Y.; Siwy, Z. S., Charge inversion and calcium gating in mixtures of ions in nanopores. *J. Am. Chem. Soc.* **2020,** *142*, 2925.
37. Garaj, S.; Hubbard, W.; Reina, A.; Kong, J.; Branton, D.; Golovchenko, J. A., Graphene as a subnanometre trans-electrode membrane. *Nature* **2010,** *467*, 190.
38. Rollings, R. C.; Kuan, A. T.; Golovchenko, J. A., Ion selectivity of graphene nanopores. *Nat. Commun.* **2016,** *7*, 11408.

39. O'Hern, S. C.; Stewart, C. A.; Boutilier, M. S.; Idrobo, J. C.; Bhaviripudi, S.; Das, S. K.; Kong, J.; Laoui, T.; Atieh, M.; Karnik, R., Selective molecular transport through intrinsic defects in a single layer of CVD graphene. *ACS Nano* **2012,** *6*, 10130.
40. Comtet, J.; Grosjean, B.; Glushkov, E.; Avsar, A.; Watanabe, K.; Taniguchi, T.; Vuilleumier, R.; Bocquet, M. L.; Radenovic, A., Direct observation of water-mediated single-proton transport between hBN surface defects. *Nat. Nanotechnol.* **2020,** *15*, 598.
41. Naguib, N.; Ye, H.; Gogotsi, Y.; Yazicioglu, A. G.; Megaridis, C. M.; Yoshimura, M., Observation of water confined in nanometer channels of closed carbon nanotubes. *Nano Lett.* **2004,** *4*, 2237.
42. Holt, J. K.; Park, H. G.; Wang, Y.; Stadermann, M.; Artyukhin, A. B.; Grigoropoulos, C. P.; Noy, A.; Bakajin, O., Fast mass transport through sub-2-nanometer carbon nanotubes. *Science* **2006,** *312*, 1034.
43. Kim, S.; Jinschek, J. R.; Chen, H.; Sholl, D. S.; Marand, E., Scalable fabrication of carbon nanotube/polymer nanocomposite membranes for high flux gas transport. *Nano Lett.* **2007,** *7*, 2806.
44. Iijima, S., Helical microtubules of graphitic carbon. *Nature* **1991,** *354*, 56.
45. Murata, K.; Mitsuoka, K.; Hirai, T.; Walz, T.; Agre, P.; Heymann, J. B.; Engel, A.; Fujiyoshi, Y., Structural determinants of water permeation through aquaporin-1. *Nature* **2000,** *407*, 599.
46. Kalra, A.; Garde, S.; Hummer, G., Osmotic water transport through carbon nanotube membranes. *Proc. Natl. Acad. Sci. U.S.A.* **2003,** *100*, 10175.
47. Dellago, C.; Naor, M. M.; Hummer, G., Proton transport through water-filled carbon nanotubes. *Phys. Rev. Lett.* **2003,** *90*, 105902.
48. Kolesnikov, A. I.; Zanotti, J. M.; Loong, C. K.; Thiyagarajan, P.; Moravsky, A. P.; Loutfy, R. O.; Burnham, C. J., Anomalously soft dynamics of water in a nanotube: a revelation of nanoscale confinement. *Phys. Rev. Lett.* **2004,** *93*, 035503.
49. Mamontov, E.; Burnham, C. J.; Chen, S. H.; Moravsky, A. P.; Loong, C. K.; de Souza, N. R.; Kolesnikov, A. I., Dynamics of water confined in single- and double-wall carbon nanotubes. *J. Chem. Phys.* **2006,** *124*, 194703.
50. Holt, J. K.; Noy, A.; Huser, T.; Eaglesham, D.; Bakajin, O., Fabrication of a carbon nanotube-embedded silicon nitride membrane for studies of nanometer-scale mass transport. *Nano Lett.* **2004,** *4*, 2245.
51. Guerra-Nuñez, C.; Zhang, Y.; Li, M.; Chawla, V.; Erni, R.; Michler, J.; Park, H. G.; Utke, I., Morphology and crystallinity control of ultrathin TiO2 layers deposited on carbon nanotubes by temperature-step atomic layer deposition. *Nanoscale* **2015,** *7*, 10622.
52. Lokesh, M.; Youn, S. K.; Park, H. G., Osmotic transport across surface functionalized carbon nanotube membrane. *Nano Lett.* **2018,** *18*, 6679.
53. Chan, W.-F.; Chen, H.-y.; Surapathi, A.; Taylor, M. G.; Shao, X.; Marand, E.; Johnson, J. K., Zwitterion functionalized carbon nanotube/polyamide nanocomposite membranes for water desalination. *ACS Nano* **2013,** *7*, 5308.
54. Wu, J.; Gerstandt, K.; Zhang, H.; Liu, J.; Hinds, B. J., Electrophoretically induced aqueous flow through single-walled carbon nanotube membranes. *Nat. Nanotechnol.* **2012,** *7*, 133.

55. Huang, S.; Cai, X.; Liu, J., Growth of millimeter-long and horizontally aligned single-walled carbon nanotubes on flat substrates. *J. Am. Chem. Soc.* **2003,** *125*, 5636.
56. Choi, W.; Lee, C. Y.; Ham, M.-H.; Shimizu, S.; Strano, M. S., Dynamics of simultaneous, single ion transport through two single-walled carbon nanotubes: Observation of a three-state system. *J. Am. Chem. Soc.* **2011,** *133*, 203.
57. Choi, W.; Ulissi, Z. W.; Shimizu, S. F.; Bellisario, D. O.; Ellison, M. D.; Strano, M. S., Diameter-dependent ion transport through the interior of isolated single-walled carbon nanotubes. *Nat. Commun.* **2013,** *4*, 2397.
58. Agrawal, K. V.; Shimizu, S.; Drahushuk, L. W.; Kilcoyne, D.; Strano, M. S., Observation of extreme phase transition temperatures of water confined inside isolated carbon nanotubes. *Nat. Nanotechnol.* **2017,** *12*, 267.
59. Secchi, E.; Nigues, A.; Jubin, L.; Siria, A.; Bocquet, L., Scaling behavior for ionic transport and its fluctuations in individual carbon nanotubes. *Phys. Rev. Lett.* **2016,** *116*, 154501.
60. Amiri, H.; Shepard, K. L.; Nuckolls, C.; Hernández Sánchez, R., Single-walled carbon nanotubes: mimics of biological ion channels. *Nano Lett.* **2017,** *17*, 1204.
61. Yazda, K.; Tahir, S.; Michel, T.; Loubet, B.; Manghi, M.; Bentin, J.; Picaud, F.; Palmeri, J.; Henn, F.; Jourdain, V., Voltage-activated transport of ions through single-walled carbon nanotubes. *Nanoscale* **2017,** *9*, 11976.
62. Tunuguntla, R. H.; Escalada, A.; V, A. F.; Noy, A., Synthesis, lipid membrane incorporation, and ion permeability testing of carbon nanotube porins. *Nat. Protoc.* **2016,** *11*, 2029.
63. Sanborn, J. R.; Chen, X.; Yao, Y. C.; Hammons, J. A.; Tunuguntla, R. H.; Zhang, Y.; Newcomb, C. C.; Soltis, J. A.; De Yoreo, J. J.; Van Buuren, A.; Parikh, A. N.; Noy, A., Carbon nanotube porins in amphiphilic block copolymers as fully synthetic mimics of biological membranes. *Adv. Mater.* **2018,** *30*, e1803355.
64. Yao, Y.-C.; Taqieddin, A.; Alibakhshi, M. A.; Wanunu, M.; Aluru, N. R.; Noy, A., Strong electroosmotic coupling dominates ion conductance of 1.5 nm diameter carbon nanotube porins. *ACS Nano* **2019,** *13*, 12851.
65. Majumder, M.; Chopra, N.; Andrews, R.; Hinds, B. J., Nanoscale hydrodynamics: enhanced flow in carbon nanotubes. *Nature* **2005,** *438*, 44.
66. Qiao, R.; Aluru, N. R., Ion concentrations and velocity profiles in nanochannel electroosmotic flows. *J. Chem. Phys.* **2003,** *118*, 4692.
67. Joseph, S.; Aluru, N. R., Why are carbon nanotubes fast transporters of water? *Nano Lett.* **2008,** *8*, 452.
68. Pascal, T. A.; Goddard, W. A.; Jung, Y., Entropy and the driving force for the filling of carbon nanotubes with water. *Proc. Natl. Acad. Sci. U.S.A.* **2011,** *108*, 11794.
69. Song, C.; Corry, B., Intrinsic ion selectivity of narrow hydrophobic pores. *J. Phys. Chem. B* **2009,** *113*, 7642.
70. Fornasiero, F.; Park, H. G.; Holt, J. K.; Stadermann, M.; Grigoropoulos, C. P.; Noy, A.; Bakajin, O., Ion exclusion by sub-2-nm carbon nanotube pores. *Proc. Natl. Acad. Sci. U.S.A.* **2008,** *105*, 17250.
71. Corry, B., Mechanisms of selective ion transport and salt rejection in carbon nanostructures. *MRS Bull.* **2017,** *42*, 306.

72. Fornasiero, F.; In, J. B.; Kim, S.; Park, H. G.; Wang, Y.; Grigoropoulos, C. P.; Noy, A.; Bakajin, O., pH-tunable ion selectivity in carbon nanotube pores. *Langmuir* **2010,** *26*, 14848.
73. Pang, P.; He, J.; Park, J. H.; Krstic, P. S.; Lindsay, S., Origin of giant ionic currents in carbon nanotube channels. *ACS Nano* **2011,** *5*, 7277.
74. Li, Z.; Li, Y.; Yao, Y. C.; Aydin, F.; Zhan, C.; Chen, Y.; Elimelech, M.; Pham, T. A.; Noy, A., Strong differential monovalent anion selectivity in narrow diameter carbon nanotube porins. *ACS Nano* **2020,** *14*, 6269.
75. Nelson, P. H., A permeation theory for single-file ion channels: Corresponding occupancy states produce Michaelis–Menten behavior. *J. Chem. Phys.* **2002,** *117*, 11396.
76. Biesheuvel, P. M.; Bazant, M. Z., Analysis of ionic conductance of carbon nanotubes. *Phys. Rev. E* **2016,** *94*, 050601.
77. Manghi, M.; Palmeri, J.; Yazda, K.; Henn, F.; Jourdain, V., Role of charge regulation and flow slip in the ionic conductance of nanopores: An analytical approach. *Phys. Rev. E* **2018,** *98*, 012605.
78. Corry, B., Designing carbon nanotube membranes for efficient water desalination. *J. Phys. Chem. B* **2008,** *112*, 1427.

Chapter 2. Carbon Nanotube Porins and Ionic Transport Measurements

Carbon nanotube porins are a merger of the concept of transmembrane porin channels with the material advantages of carbon nanotubes. Porin proteins like aquaporins (AQPs) have a narrow channel size, hydrophobic inner surface, and fast water transport.[1, 2, 3] To mimic the function of porin proteins, carbon nanotubes (CNTs) are an ideal candidate due to their structural similarities: smooth hydrophobic inner surfaces and well-defined diameters based on chirality.[4, 5] Therefore, our group wrapped CNTs with lipids and further cut these CNTs using ultrasonication to obtain ultrashort carbon nanotubes, which are akin to the size of membrane proteins.[6, 7] We named these nanostructures carbon nanotubes porins (CNTPs). The advantages of CNTPs include their short length, which limits the number of defects along the tube, and also their narrow, well-defined diameter. In addition, CNTPs can self-insert into lipid bilayers.[6, 7, 8] These properties allow us to study nanofluidics through CNTPs using measurement methods commonly employed for membrane proteins, the use of lipid vesicles and planar lipid bilayer platforms. In this chapter, I will discuss the properties of CNTs and CNTPs and further talk about the ionic transport measurements carried out using these nanotubes.

2.1 Carbon Nanotubes (CNTs)

Carbon nanotubes were first discovered by Iijima in 1991 by examining arc discharged CNTs using transmission electron microscopy (TEM).[9] Later in 1993, single walled-carbon nanotubes (SWNTs) were observed.[10, 11] SWNT diameters typically range from 0.5 up to 3 nm, while multi-walled carbon nanotubes (MWNTs) are made up of two or more concentric SWNTs and can be as thick as tens of nanometers.[9] Owing to their unique physiochemical properties and atomic thickness, SWNTs have found extensive applications in a number of research areas and become an integral material in nanotechnology.[12, 13]

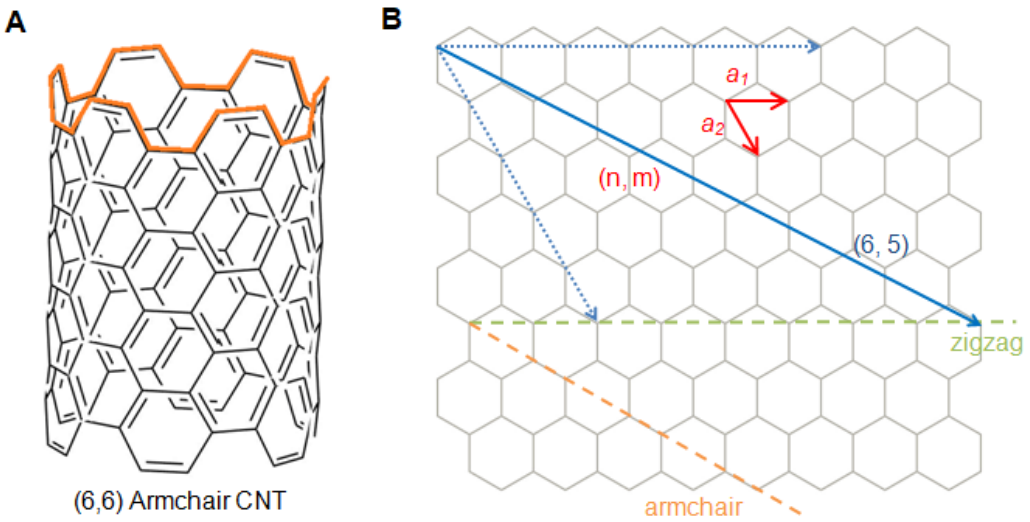

Figure 2.1. CNT structure. (**A**) An armchair CNT, (6,6) chirality. (**B**) A schematic diagram of how to roll-up a sheet of graphene to form a single-walled CNT with the roll-up vector (n, m). Green dash line direction is to form zigzag CNTs, while orange dash line direction is to form armchair CNTs like (A).

Structure/Chirality

SWNTs are conceptualized as rolled-up single graphene sheets and the cylindrical structure has been validated using TEM, scanning tunneling microscopy (STM), and Raman measurements.[9, 14] The roll-up vector, known as the chiral vector, is defined by the chiral indices (*n*, *m*).[5] By connecting the origin point (0, 0) and another point (*n*, *m*) on the 2D graphene sheet, one can form a SWNT with the chiral vector denoted as

$$\vec{C} = n\vec{a_1} + m\vec{a_2}$$

where $\vec{a_1}$ and $\vec{a_2}$ are the unit vectors of a hexagonal graphene lattice. Nanotubes with the chiral indices (*n*, 0) or (0, *m*) are known as zigzag CNTs, (*n*, *n*) corresponds to armchair CNTs, and any other combination of *n* and *m* is referred to as a chiral CNT (Fig. 2.1). The superimposition of two edges perpendicular to the vector yields the structure of the chiral CNT structure with diameter *d* and chiral angle *θ*. The diameter *d* of a CNT is given by[5]

$$d = \frac{\vec{C}}{\pi} = \frac{|\vec{a_1}| \cdot \sqrt{n^2 + m^2 + nm}}{\pi} = \frac{\sqrt{3}a}{\pi}\sqrt{n^2 + m^2 + nm}$$

where *a* is distance between the nearest neighboring carbon atoms, 144 picometer. For example, the diameter for (6,5) CNT is *ca.* 0.76 nm. The chiral angle θ is given by[5]

$$\theta = \tan^{-1}\frac{\sqrt{3}\mathrm{n}}{2\mathrm{m}+\mathrm{n}}$$

Synthesis

CNTs are typically synthesized using one of the three methods: arc discharge, laser ablation, or chemical vapor deposition (CVD).[15] Depending on the method of synthesis, SWNTs with different diameter and chirality distributions will be obtained. The first CNTs were produced by the Iijima group using the arc discharge method, which resulted in larger diameter CNT bundles, predominately MWNTs, forming at the negative electrode.[9] The Iijima group subsequently adapted the same method to yield SWNTs with sub-2-nm diameter,[10] and around the same time, Bethune *et al.* pioneered using Co filled graphite rod anodes in arc discharge chambers to produce SWNTs with a narrower diameter distribution.[11] The Smalley group later developed an efficient route for SWNT synthesis using laser ablation with a Co-Ni/graphite composite at 1200 °C.[16] This method yielded a 70-90% conversion of the graphite into SWNTs.[16] However, as arc discharge and laser ablation use solid-state carbon precursors as the carbon source for the CNT growth, they require high temperatures to vaporize the carbon and typically have large amounts of amorphous carbon and other by-product impurities.[16] To circumvent the need for high temperature, chemical vapor deposition (CVD) were subsequently presented as a synthesis method for SWNTs by leveraging hydrocarbon decomposition over transition metal catalyst nanoparticles.[17, 18] CVD utilizes hydrocarbon gases as the carbon sources and small catalyst particles as seeds for CNT growth.[18] This process happens at comparatively lower temperatures than arc discharge and laser ablation, yet can still produce both individually isolated CNTs and densely packed, vertically aligned CNT arrays.[15, 18, 19, 20] Studies have shown that the distribution of CNT chirality/diameter is strongly influenced by the size/composition of the catalyst particle, growth temperature, and other growth conditions.[15, 20] To date, the large-scale production of chirality pure CNTs remains elusive, which has somewhat limited their applications and led to

significant research into methods for chiral SWNT separation/enhancement post-synthesis.[21]

Mechanical and Electronic Properties

Graphene is exceptionally strong regarding in-plane deformations, thus CNTs, the seamless graphene tubular structures, also possess extraordinary mechanical properties.[4] CNTs exhibit no cross-sectional and twisting distortions, and have an exceptionally high Young's modulus.[14] This flexibility is in good agreement with their high tensile strength and bulk modulus. However, despite the high strength of individual CNT shells (SWNTs), that weak shear interactions between concentric shells results in much lower mechanical strength for MWNTs.[5] Additionally, for large deformations occurred upon both compression and bending, the tube buckling behavior was observed in simulation and showing that the bucking strain was CNT chirality-dependent.[22, 23] Overall, the strength and stiffness of CNTs are dependent on nanotube chirality, the presence of any defects along the nanotubes, and the direction of the applied forces (axial vs. radial).[22, 23, 24]

The nanotube chirality also determines the electronic structures of CNTs. The roll-up tubular graphene sheet has electronic states in the π-electron system, resulting in unusual band structures.[4, 25] Wavefunction boundary conditions vary with the (n, m) values and as a result, each chirality has its own electronic structure.[4, 25] Based on the distribution of electronic states, CNTs can behave as metallic or semiconducting tubes. When the value of (n - m) equals a multiple of 3, the CNT has a finite density of states at the Fermi level and therefore is metallic. When it's not, the CNT is semiconducting and has a band gap at the Fermi level (Fig. 2.2).[4, 5] For example, the band gap of a (6,5) CNT is 1.272 eV, while (7,4) CNT is metallic and therefore has no bandgap.[5]

Optical Properties

To understand the optical properties of SWNTs, a simple band theory model explaining the electronic states distribution could be used (Fig. 2.2).[25, 26] For metallic tubes, conduction bands and valence bands are adjacent, while there is a energy gap in between for semiconducting tubes.[25] Each chiral SWNTs has its own band structure and corresponding energy bandgaps, which also determine the optical features.[26, 27, 28]

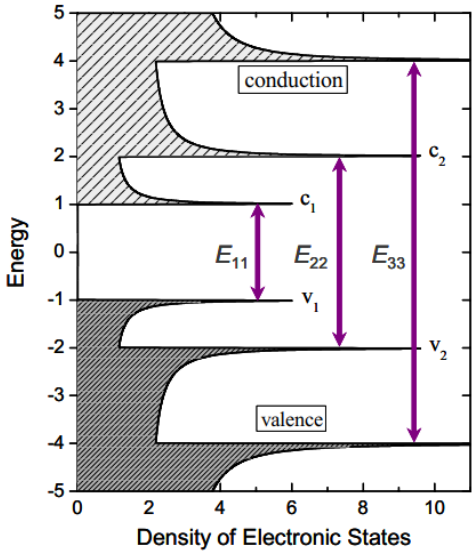

Figure 2.2. Semiconducting SWNT electronic state distribution. Vertical arrows are the illustration of allowed optical energy transition. Image adapted with permission from ref [25].

Nanotube photoluminescence (PL) happens when a excitonic state (photo-excited electron) relaxes down to the ground state by emitting a photon whose energy corresponds to the bandgap of semiconducting carbon nanotubes, like E_{11} in Fig. 2.2.[25, 26, 28] For semiconducting SWNTs with diameters near 1 nm, the first three of these transitions appear in the near-infrared (NIR), visible, and near-ultraviolet regions. Photoluminescence excitation, on the other hand, absorbs energy corresponds to higher energy bandgap (E_{22} transition).[26] Combining both PL techniques, a 3D excitation-emission profiles (PL maps) could be collected and it's a powerful optical technique to determine CNT chirality distribution.[25, 26] However, PL spectroscopy is limited to semiconducting tubes, and local dielectric constants, such as the influences from absorbed molecules on CNT surfaces and the solvent used, also strongly alter the results.[25] Furthermore, the presence of metallic tubes in CNT bundles significantly reduces the fluorescence intensity because semiconducting CNTs would transfer the energy for fluorescence to metallic CNTs and a non-radiated decay takes place.[25] All of these factors must be considered when extracting information from PL maps. While samples with higher purity and well suspended CNTs are needed for PL maps, other

complimentary techniques like Raman spectroscopy are used to validate and support PL data.

Raman spectroscopy studies the vibrational modes of CNTs by measuring inelastically scattered light emitted by the material and can be used to characterize both semiconducting and metallic CNTs.[29] The most prominent features in a CNT Raman spectrum are the radial breathing modes (RBM) and the D-band, G-band, and G'-band, which all provide structural information about the CNTs. The frequency of the RBM (100-300 cm^{-1}) are inversely proportional to the diameter of the CNTs and as such can provide information on the diameter of a carbon nanotube and the diameter distribution in the sample.[29] RBM are not present in graphene or any other graphene-related structure and hence can be used to confirm that CNTs are present in the sample.[29] The higher frequency D-band, G-band, and G'-band are feature peaks similar to graphite. The G band (~1580 cm^{-1}) is a first-order scattering process that corresponds to the in-plane bond stretching mode of the C-C bonds in the graphitic hexagonal lattice.[29] The D band (~1330 cm^{-1}) is a longitudinal phonon and is known as the defect mode.[29] The G' band (~2600 cm^{-1}) is the second-order scattering from D-band variation.[29] These Raman features provide CNT structural information based on the vibration behavior and the optoelectronics properties.

2.2 Carbon Nanotube Porins (CNTPs)

The spatial confinement and hydrophobic surface of the CNTs' inner pores are highly reminiscent of AQPs.[1, 5, 30] The Hummer group predicted that this should enable CNTs to achieve enhanced water flow, similar to the high water flux in AQPs and faster than 1D water diffusion.[31, 32] However, as discussed in Chapter 1, it took more than a decade to experimentally observe the water flux values higher or similar to AQPs. This delay is attributed to variations in two physical parameters of the nanotubes, specifically their diameter and the length. Results from simulations show that a single-file water chain occurs in CNTs when the diameter is smaller than 0.95 nm.[33] Larger diameters only give partial confinement, meaning that the molecules do not present single-file configurations and so the water permeability is not significantly higher than what is observed in the

bulk.[8, 34] Additionally, for many of the initial experiments, the length of the CNTs used was typically in the micrometer range,[5] and inevitably, there were various degrees of defects along the tube.[24, 35, 36] These defects can interact with water molecules, causing friction and breaking down the single-chain water transport.[30, 37]

Our group addressed these by using ultrashort CNTs (CNTPs) with lengths of *ca.* 10 nm and diameters of either 0.8 nm (narrow CNTP, nCNTP) or 1.5 nm (wide CNTP, wCNTP) (Fig. 2.3).[6, 7, 38] These two diameters enabled us to perform nanofluidic studies under extreme and partial confinement conditions. By using the ultrashort CNTP length, we could limit the likelihood of defects along the channel wall and therefore remove any contribution from detect interference on the flux.[24, 36] Additionally, as these CNTs were prepared using lipid molecules, which wrap along the hydrophobic side-wall of the nanotubes, the resulting CNTPs were dispersed in aqueous solution,[6, 7] facilitating single channel nanofluidic studies.

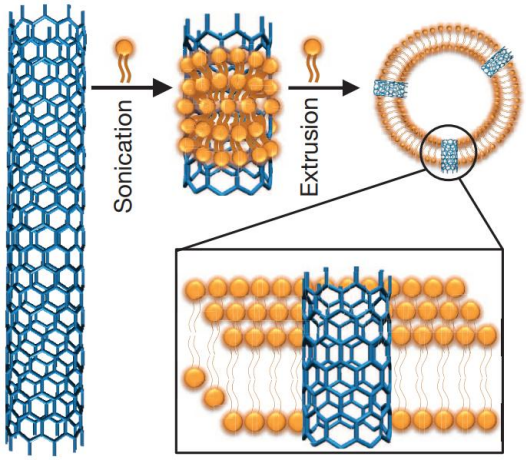

Figure 2.3. **Schematic showing CNTP preparation and incorporation into lipid vesicles.** Image adapted with permission from ref [6]. Copyright © 2014, Nature Publishing Group, a division of Macmillan Publishers Limited. All Rights Reserved.

Synthesis

Due to the van der Waals forces between CNTs, CNTs tend to aggregate into bundles. In order to synthesize CNTPs, these bundles need to first be broken apart into individual nanotubes, which subsequently need to be cut into ultrashort in lengths. Individualized CNTs were first dispersed in aqueous solution by the Smalley group by

sonicating CNTs in the presence of a surfactant, sodium dodecyl sulfate (SDS).[26] Other surfactants (sodium cholate, sodium deoxycholate) and biomolecules (DNA, RNA, proteins) have subsequently been used to non-covalently functionalize and disperse CNTs using ultrasonication.[39, 40] For our work, we utilized lipid molecules, 1,2-dioleoyl-*sn*-glycero-3-phosphocholine (DOPC), to disperse commercially available CNTs into an aqueous solution using mild bath sonication (Fig. 2.4).[7] These dispersions were subsequently sonicated for 12 hours using tip ultrasonication (650-750 kJ energy applied) to both break the bundles apart and cut the CNTs into smaller pieces.[7]

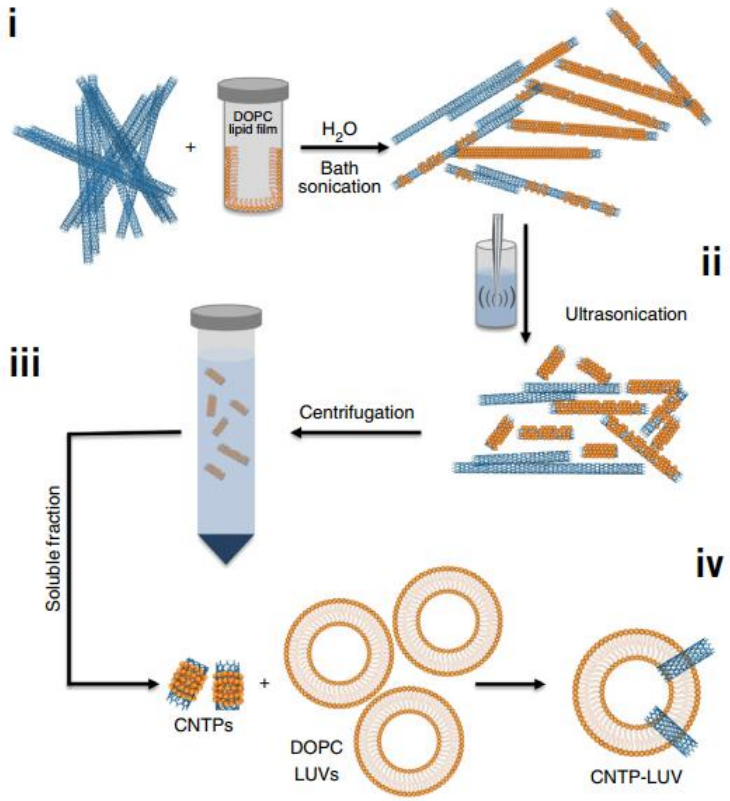

Figure 2.4. Synthesis steps for CNTPs and CNTP lipid vesicles. Image adapted with permission from ref [7]. Copyright © 2016, Nature Publishing Group, a division of Macmillan Publishers Limited. All Rights Reserved.

During the tip ultrasonication process, ultrasonic waves generate small vacuum bubbles in the solution. In each ultrasonication cycle, the bubbles grow and reach a maximum volume, and then collapse violently. This process is called cavitation and

creates extremely high temperature and pressure locally. During bubble growth, CNTs align tangentially around the vacuum bubbles due to its hydrophobic nature; while during the collapse step, the local forces could exfoliate the bundles, and moreover, buckle the CNTs making shorter tubes.[41] Studies have shown that prolonged or higher intensity ultrasonication can be used to generate shorter CNTs, down to 10 – 100 nm lengths.[41, 42, 43] Notably, this process is chirality-dependent due to difference in the critical buckling strain values for different CNTs.[22, 23] For example, CNTs with chiral angles around 15° (between 0° - 30°) have reported to have the lowest critical buckling strain, and hence are expected to be easier to break into shorter lengths.[22]

Following ultrasonication, we centrifuged our CNTP solutions to remove remaining CNT bundles (which should aggregate at the bottom), uncut long tubes, and metal particles from ultrasonication tips. The extracted supernatant contained DOPC-wrapped CNTPs that were well-dispersed in water.[7] This solution was used to incorporate CNTPs into lipid bilayers.[7] As the thickness of DOPC lipid bilayers (18 carbon atoms in the hydrocarbon chain) is *ca.* 4-5 nm,[44] any CNTs that are much longer than 10 nm cannot be successfully incorporated into the bilayers. These long CNTs should be removed during the extrusion and size separation steps when making lipid unilamellar vesicles (LUVs). As a result, we expect that the final CNTPs are those with lengths comparable to the lipid bilayer thickness and have the ability to incorporate into lipid bilayers. This hypothesis was confirmed with Cryo-TEM images that showed that the length distribution of incorporated CNTPs was from 5 to 30 nm, with the majority have a length of 10 nm.[6, 38]

CNTP Structures and Characterizations

The chirality distribution in the starting CNT material is the dominating factor determining the final diameter of the CNTPs. nCNTPs are synthesized using SWNTs with a 0.78 nm average diameter (mainly (6,5) SWNTs (Sigma, Chasm Advanced Materials)), while wCNTPs are made of SWNTs with average 1.5 nm diameter (NanoLab). The former are heavily enriched in semiconducting nanotubes and are easily characterized using optical methods such as PL maps or absorbance spectroscopy, while the latter are a mixture of semiconducting, semi-metallic, and metallic tubes and the diameter is determined by TEM images and Raman spectroscopy.

PL maps of the nCNTP starting material suspended in 1% SDS (Fig. 2.5) showed a strong fluorescence peak (*ca.* 990 nm emission) corresponding to the (6,5) CNT (as expected). The major chirality (6,5) was *ca.* 0.76 nm in diameter, while other chiralities, diameter ranging from 0.68 to 0.83 nm, were observed as well. Following ultrasonication cutting, the nCNTPs showed interesting features in PL maps (Fig. 2.6, left), most notably a distinct absence of the (6,5) peak around 990 nm. In addition, the PL map intensity was much lower, which required higher integration time during measurements and gave higher background noise. This result was expected as short nanotubes are known to have much lower fluorescence emission compared to longer nanotubes.[28, 45, 46] Post-cutting, the primary peak was significantly shifted to an emission wavelength of around 1150 nm. A similar PL spectrum was observed for end-functionalized (6,5) CNTs, where the peak around 1150 nm was attributed to and fluorescent defect state E_{11}^{-}.[47] A PL map of only DOPC solution was also measured as a background check, and no PL peak was observed (Fig. 2.6, right), indicating that the peak in the CNTP sample was indeed originating from nanotubes in the solution. Based on this, we believe our nCNTPs are predominately (6,5) CNTs of shorter length, leading to the existence of a defect state similar to the E_{11}^{-}, however, the exact origin of this state remains unknown. This hypothesis is supported by our observation that nCNTPs synthesized from chirality separated (6,5) SWNTs also showed the same, red-shifted peak in the PL map post-sonication. Based on these results, we have chosen to use the (6,5) CNT diameter, 0.76 nm, as the nCNTP diameter in the analysis of our experiments.

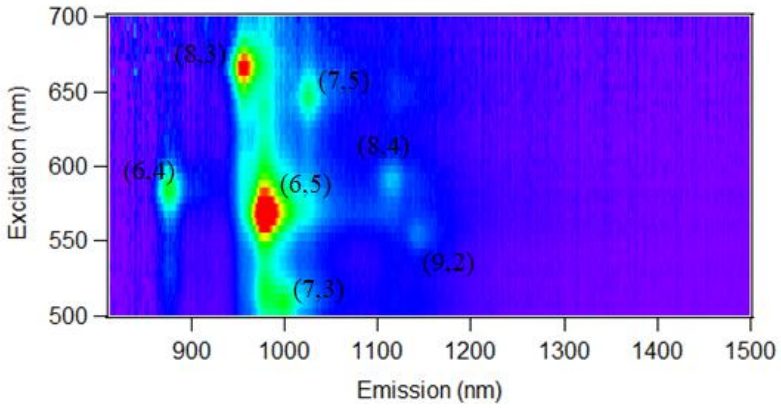

Figure 2.5. The PL map of the starting SWNT materials for nCNTP.

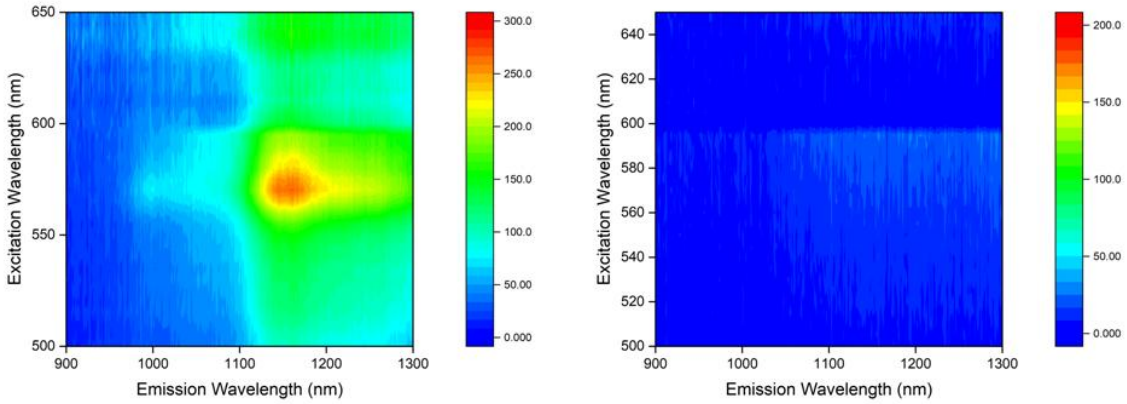

Figure 2.6. PL maps of nCNTP (left) **and DOPC as background** (right).

Absorption spectroscopy also shows the E_{11}^{-} peak at 1150 nm while we still observed the E_{11} peak around 1000 nm. The E_{22} peaks were observed around 600 nm. Compared to micron-long SWNT raw materials, the signal intensity of nCNTPs was lower and broader.[28, 48, 49] The latter could come from remained CNT bundles and the influence from lipid wraps. The resulted absorption spectroscopy actually varied between nCNTP batches (Fig. 2.7) with different peak intensities and different peak ratio (E_{11} vs. E_{11}^{-}), which could come from the differences in starting CNT material weight and conditions, applied energy during ultrasonication, and lipid wrap conditions.

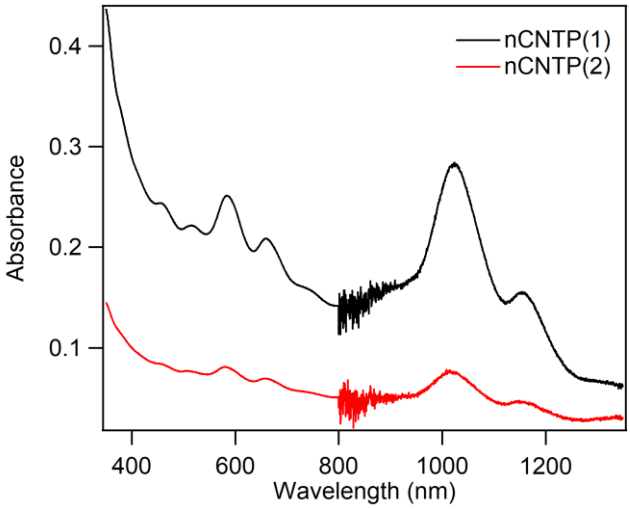

Figure 2.7. Absorption spectroscopy of nCNTP. Two samples showed different CNT concentrations that nCNTP(1) was much higher than nCNTP(2).

The length of CNTPs could be estimated using dynamic light scattering (DLS) (Fig. 2.8).[49] Although DLS cannot measure the real length of CNTPs, it reflects the relative length differences between different CNTP batches. As shown in Fig. 2.8, nCNTP1 (gray) showed two size peaks, one around 30 nm and the other around 100 nm, while nCNTP1+ (red), with a longer ultrasonication time (higher cutting energy), showed the shift of the peak toward smaller sizes.

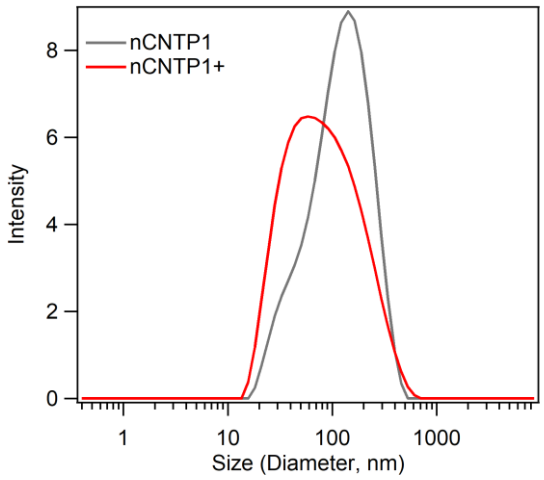

Figure 2.8. DLS particle size distribution of nCNTPs. nCNTP1+ is with longer ultrasonication time (higher cutting energy) compared to nCNTP1.

Meanwhile, the length of CNTPs could be measured using TEM and cryogenic TEM (cryoTEM). Since the length of CNTPs are *ca.* 10 nm, it's extremely hard to find these tubes in TEM images. Thus, incorporating CNTPs into lipid vesicles for imaging is a better way. It also avoids the issue that CNTs have high affinity to the carbon grids and are hard to be observed in hollow image windows. In cryoTEM images (Fig. 2.9), we observed lipid membrane around 4 nm in thickness and wCNTPs (1.5 nm in diameter, *ca.* 10 nm in length) inserted. Although the resolution of CNTP images is not high because both lipids and CNTPs are carbon-based, we can still label the CNTPs and obtain the length distribution.[6]

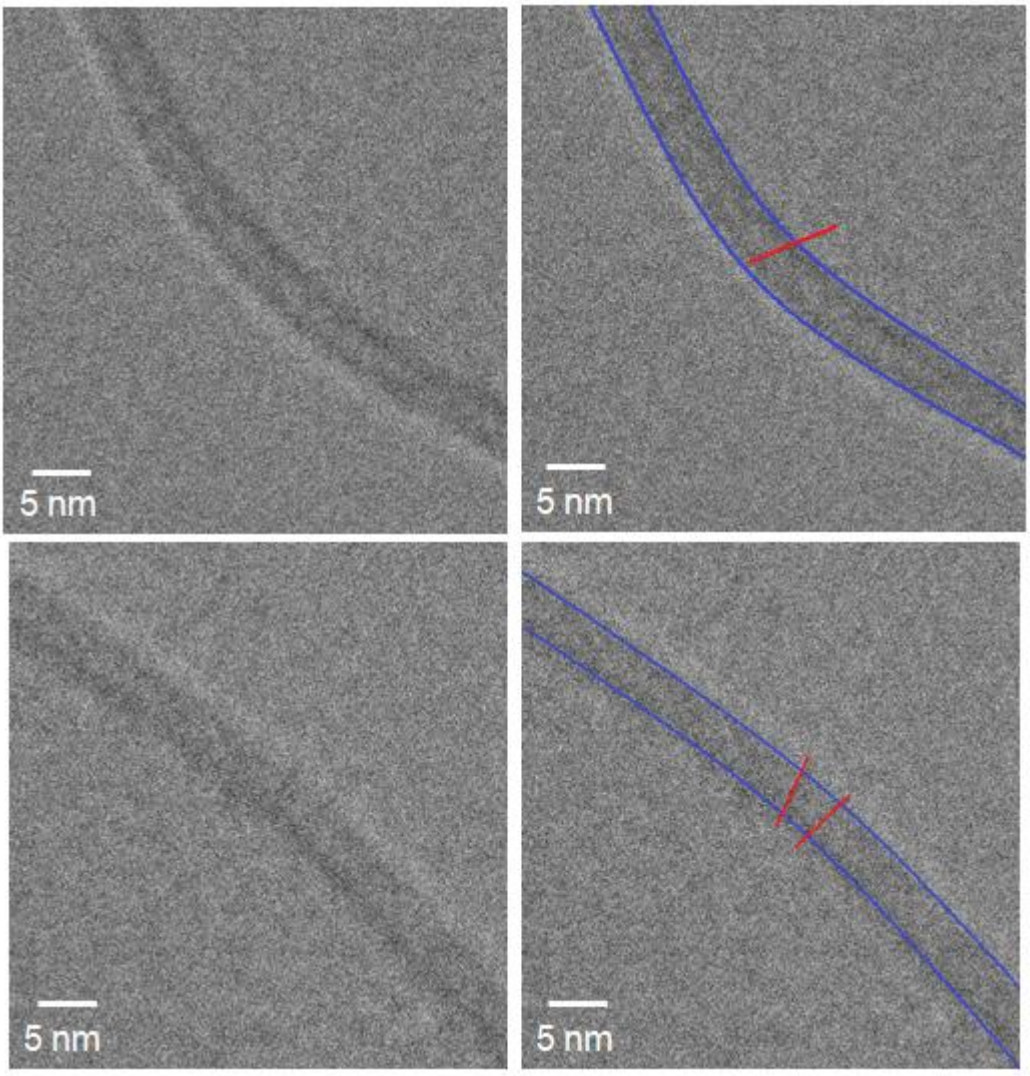

Figure 2.9. Cryogenic TEM images of wCNTP-LUVs. Left: original images. Right: images with blue lines for lipid bilayer boundary and red lines for wCNTPs.

Raman spectroscopy is another powerful tool that gives the characterization of CNTPs (Fig. 2.10). The RBM peaks for nCNTP were assigned for diameters around 0.8 nm and for wCNTPs were assigned for diameters ranging from 1.2 nm to 1.6 nm.[49] Another important parameter is the ratio between D-band (1330 cm^{-1}) and G'-band (2600 cm^{-1}), which indicates the level of "defects" in the CNTs. For μm-long CNTs, D/G' ratio is usually lower than 2%, indicating less defects and high CNT quality.[29] However, for CNTPs, the ratio is ranging from 60% to 120%. The reason that D/G' ratio is much

higher for CNTPs is that end-groups of CNTPs are counted as "defects" in Raman, and since CNTPs are much shorter, the signal from CNTP ends are much stronger.

The broad peaks with the highest point around 2800 cm^{-1} in Fig. 2.10 A and B were first assigned as DOPC lipid peak;[49] however, they are actually the photoluminescence peak of glass microscope slides using excitation laser at 633 nm.[50] When changing the sample preparation method and having the excitation laser focus on the liquid sample, the broad peak disappeared (Fig. 2.10 C).

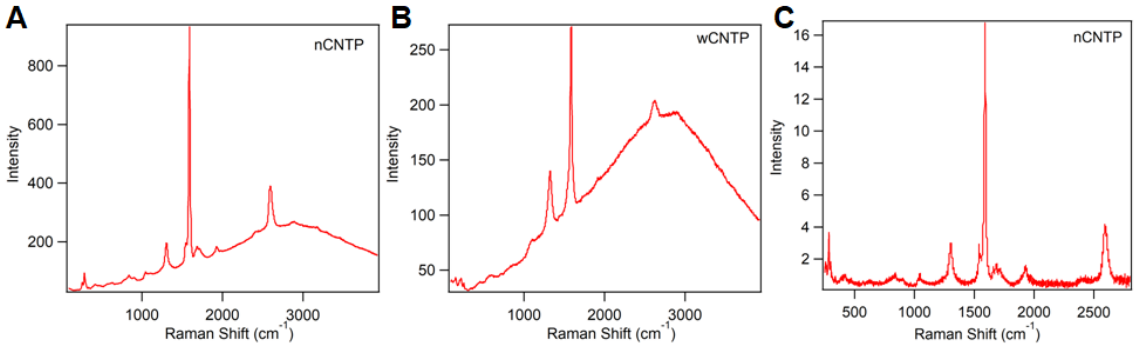

Figure 2.10. Raman spectroscopy of CNTPs. (**A**) nCNTP, (**B**) wCNTP, and (**C**) nCNTP with a new sample preparation method, using excitation laser at 633 nm.

In addition to diameter and length, the presence of end-groups on CNTPs plays a critical role in nanofluidics. Studies have shown CNT ends after tube end oxidation or ultrasonication cutting were carboxylate groups ($-COO^-$).[43, 51, 52] We further conducted pH-dependent studies with our CNTPs and found a significant difference between pH 3 and pH 5 in water and ion transport studies, which corresponds to the pK_a of carboxylate groups.[8, 52, 53] Additionally, we were able to modify the CNTP ends using EDC coupling to attach either methyl groups or gold nanoparticles.[38, 54, 55] These results demonstrate that flexibility of the platform by showing how alternative functional groups can be incorporated, which can be used to tune the transport behavior of the CNTPs.

2.3 Lipid Vesicle Platforms for Measuring CNTP Transport

The ability of CNTPs to self-insert into lipid bilayers means that experimental platforms typically used to study membrane protein channels can be readily adapted to study CNTPs.[6, 30] The use of lipid large unilamellar vesicles (LUVs) platform is one

example of platform that can be used to study CNTP transport behavior. By encapsulating pH-sensitive dyes in lipid LUVs, overall proton permeability values through CNTP-containing LUVs (CNTP-LUVs) can be measured using a fluorometer or a stopped-flow apparatus.[38] This enables the calculation of the proton flux through CNTP channels by comparing permeability differences between CNTP-LUVs and control LUVs (no CNTPs).[38] Correlating these values with the average number of CNTPs per LUV (as counted using cryoTEM), proton permeability values for individual CNTPs were derived.[38] Similarly, this setup can be used with anion-selective dyes to determine anion permeability values or with concentration-dependent self-quenching dyes to calculate water permeability numbers.[56, 57]

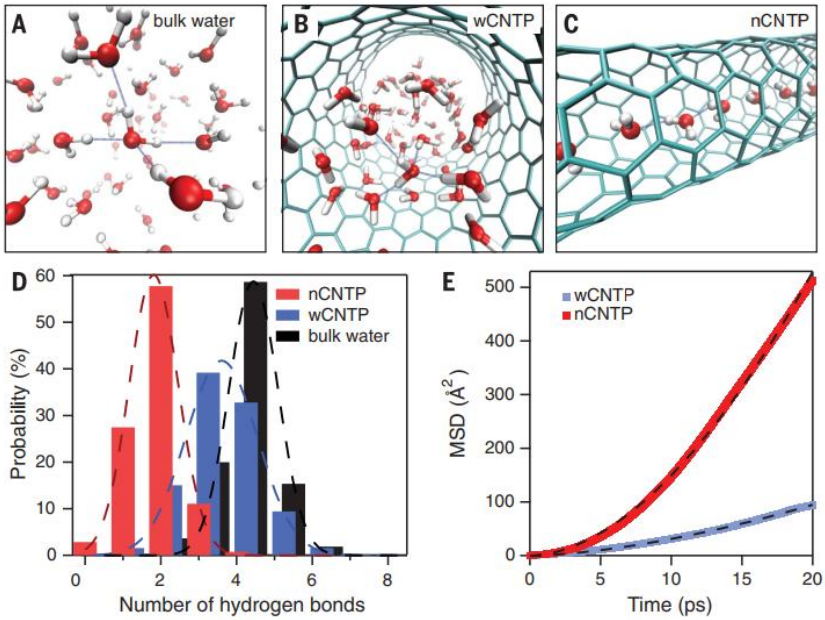

Figure. 2.11. Hydrogen-bonding pattern and water diffusion in nCNTPs and wCNTPs. Image adapted with permission from ref [8]. Copyright © 2017, The American Association for the Advancement of Science.

Previous work from our group has shown that the overall permeability values of proton and water are significantly increased following the addition of CNTPs to the LUVs. Notably, ultrafast proton permeability was observed for nCNTPs, which was attributed to single-chain water structures inside of the nCNTPs that facilitated proton

hopping (Grotthuss mechanism).[38] For water transport, experimental measurements showed that nCNTPs exhibited remarkably high rates, even exceeding those of AQPs.[57] First principle simulations supported these experimental observations and demonstrated differences in the hydrogen bonding between water molecules inside of nCNTPs, a wCNTPs, and in the bulk (Fig. 2.11).[8] This confirmed the existence of a single-file water structure under extreme confinement in nCNTPs and the direct relationship between enhanced water flux and the single chain water structure.[8] Interestingly, in the slightly larger pores, wCNTPs, water molecules were only partially confined, and the water permeability was much lower.[8, 57] These findings again highlight the critical role that molecular-scale confinement plays in transport.

Once the proton permeability values of individual CNTPs were established, proton permeability measurements (the proton assay) could be utilized to count the amount of CNTPs in a lipid vesicle (Fig. 2.12).[38, 58] As the individual proton permeability was known, the proton assay could be used to identify transport differences between different synthesized CNTP batches and the rate of incorporation into the lipid vesicle (CNTP yield, the number of CNTPs per LUV). Examining Fig. 2.12, we can compare the proton transport behavior between control LUVs (the gray line) and CNTP-LUVs (blue, red, and orange lines). With addition of transmembrane CNTPs to the LUVs, we observed clear changes in the rate of fluorescence decrease. This kinetic process shows that the proton flow goes from outside to inside the LUV (changing the local pH) over the course of the experiment (*ca.* 150 second). As shown by the red and orange lines, both nCNTP-LUVs but with different CNTP yields, when the number of CNTPs per LUV is higher, there is a faster decrease in the fluorescence.

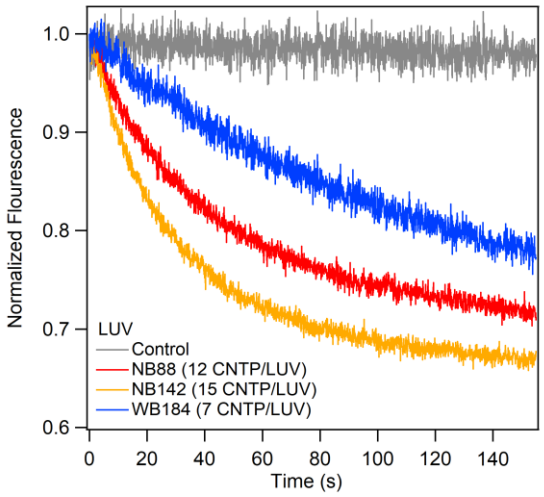

Figure 2.12. **The decreases of normalized fluorescence intensity in proton assay.** The dye encapsulated in LUVs was HPTS, a pH sensitive dye working in the range of pH 6.5-8.0.

Interestingly, proton assay yields do not seem to be directly related to CNT concentration, as determined from peak intensities in the absorption spectra. For example, as shown in Fig. 2.7, the CNT concentration of nCNTP(1) was much higher than nCNTP(2), but the proton assay yields were similar. On the other hand, the size distribution in DLS for the CNTP solutions seems to give a clue to proton assay yields, which smaller CNTPs having higher proton assay yields (Fig. 2.8, nCNTP1+ had a higher yield than nCNTP1). However, additional experiments are still required in order to fully elucidate the relationships between the physiochemical prosperities of CNTP batches and resulting incorporation yields.

2.4 Ionic Transport Measurements

Ionic transport setups are another platform typically used for studying protein membrane channels[59] that can be readily adapted for CNTP.[6] In these setups, free-standing planar lipid bilayers cover an aperture, with reservoirs for electrolyte solution on both sides. Ionic measurements are carried out by applying a voltage bias and collecting the current response.[8, 59] To form the planar lipid bilayers for CNTPs, two methods have been developed and used: painted lipid bilayers and modified planar lipid bilayers (Fig. 2.13, 2.14, and Table 2.1).[6, 7, 8, 53]

The painted lipid bilayer method is a well-established method used to form planar model lipid systems. In this setup, apertures with diameters *ca.* 30 – 80 μm are formed in a Teflon (PTFE) thin film using a high-frequency generator, which generates a spark at a high voltage. DOPC lipid molecules, dissolved in an organic solvent like decane, are 'painted' across the Teflon aperture where they undergo lipid self-assembly on the hydrophobic Teflon support triggered at water-organic solvent interfaces. CNTP insertions can be monitored by recording current jumps following the addition of CNTP solution into the electrolyte solution (Fig. 2.13). Comparing the current jumps overtime can give statistical values of CNTP conductance as a function of the number of channels inserting (Fig. 2.13c).

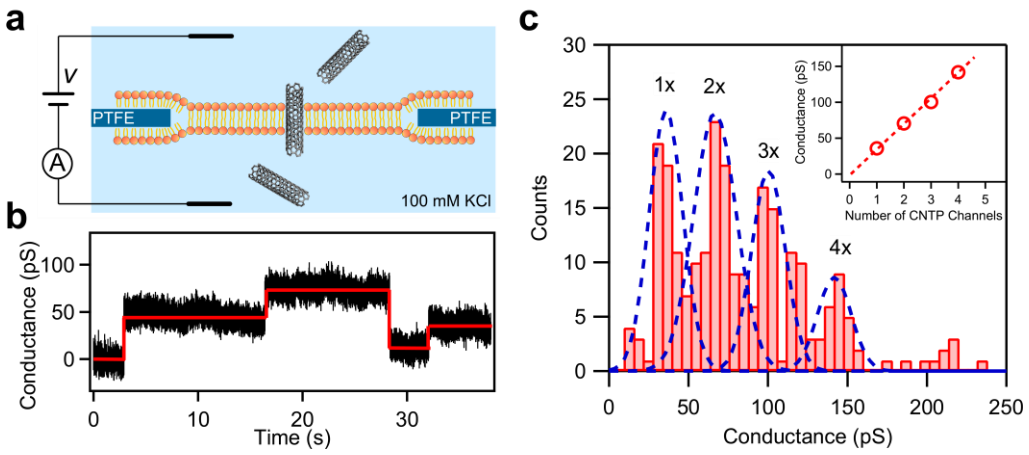

Figure 2.13. Painted lipid bilayer method for nCNTP ionic conductance measurements at 100 mM KCl. (**a**) Schematic of painted bilayers and nCNTP insertions. (**b**) Current trace over time showing jumps. (**c**) nCNTP conductance distribution. Images adapted from a manuscript in preparation.

However, these current jumps also create problems when using this platform measuring CNTP ionic transport. As the CNTPs are dynamic, showing frequent insertion and popping out movements, stable current-voltage curves (I-V curves), like those obtained for protein channel measurements, are not feasible using the painted lipid bilayer setup. Although the exact reason behind this is unclear, we hypothesize that it is related to the interaction between the organic solvent and the hydrophobic CNTP wall. Thus, in order to obtain a stable current associated with stable CNTP insertions, we

developed the modified planar lipid bilayer method. The main difference of this method is that we use fabricated silicon chips with a SiN_x (silicon nitrite) and a *ca.* 100 nm aperture. Lipid vesicles around 200 nm in diameter, including LUVs and CNTP-LUVs, were utilized to cover these nano-apertures. Upon adsorption to the hydrophilic surface, the lipid vesicles ruptured spontaneously, resulting free-standing lipid bilayers.[60, 61] This solvent-free approach was able to improve CNTP insertion and enabled stable CNTP current traces and I-V curves (Fig. 2.14). Using this setup, we were able to derive both conductance values (under symmetric electrolyte concentration conditions) and reversal potential values (under asymmetric concentration conditions) for the CNTPs. The CNTP conductance values derived using this method were in good agreement with those obtained using the well-established painted lipid bilayers, indicating the reliability of this setup. To further validate this method, we tested the ion selectivity ratio of known protein channels, including α-hemolysin channels (*ca.* 1.5 nm in diameter) and gramicidin channels (*ca.* 0.4 nm in diameter) (Fig 2.15). We obtained gave K^+/Cl^- ratio of 0.54 and close to ∞, for α-hemolysin and gramicidin respectively, matching literature numbers.[62, 63] In addition, as the aperture size was much smaller than in the Teflon film used in the painted method, this new method provided much higher stability and longer life-time. For these reasons, in my work I predominately used the modified planar lipid bilayer method with the help of the painted lipid bilayer method to confirm conductance values.

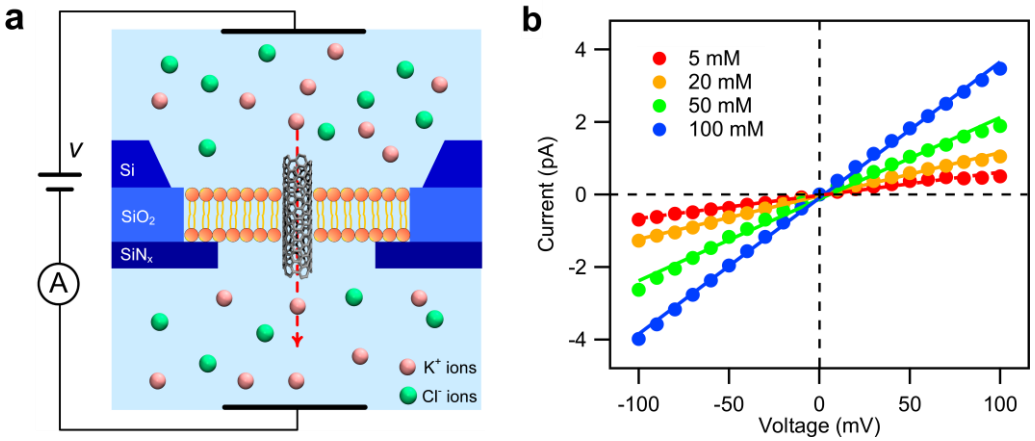

Figure 2.14. Modified planar lipid bilayer method. (**a**) Schematic of SiN_x aperture and one nCNTP inserted in the lipid bilayers. (**b**) nCNTP I-V curve measurements to derive ionic conductance values at various KCl concentrations.

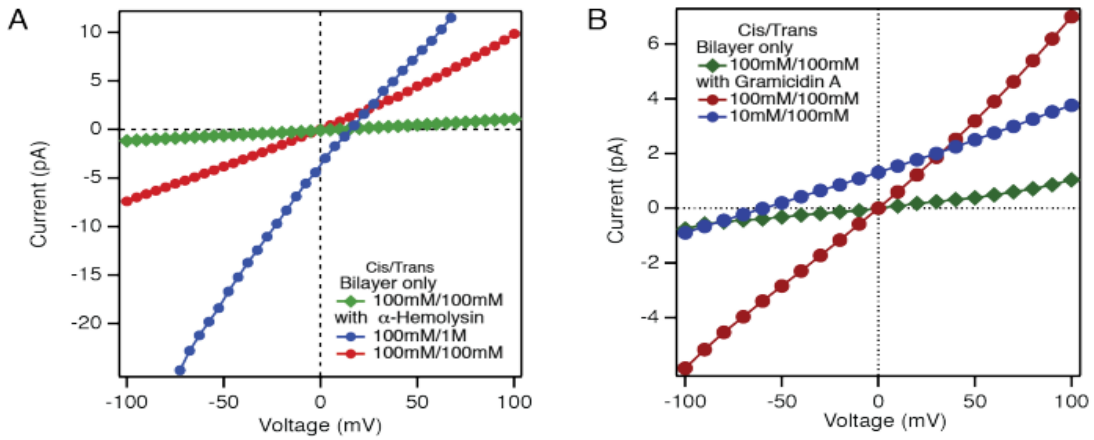

Figure 2.15. Reversal potential measurements for ion selectivity of protein channels. The I-V curves of (**A**) α-hemolysin channels and (**B**) gramicidin channels under symmetric and asymmetric KCl concentration conditions. The zero-current voltage shifts from red to blue curves are the reversal potential value. Image adapted with permission from ref [8]. Copyright © 2017, The American Association for the Advancement of Science.

Table 2.1. Comparison of painted lipid bilayer method and modified planar lipid bilayer method

Method	Painted Lipid Bilayer	Modified Planar Lipid Bilayer
Principle	Organic solvent-assisted self-assembly of lipid molecules on a hydrophobic surface in an aqueous environment	Spontaneous rupture of adsorbed lipid vesicles on a hydrophilic surface in an aqueous environment
Aperture Material	Teflon (PTFE) film	SiN_x membrane
Aperture Diameter	*ca.* 50 μm	*ca.* 100 nm
Lipid Bilayer	DOPC with trace mount of organic solvent	DOPC + Cholesterol
CNTP Behavior	Dynamic CNTP insertion and popping out	Stable CNTP insertion
Measurements	Current jumps over time to obtain conductance	I-V curves to obtain conductance and reversal potential
Advantages	Short preparation time, high success rate	Stable current, low noise, long insertion life-time
Drawbacks	Dynamic CNTP movements, lower membrane stability	Long preparation time from aperture fabrications to forming lipid vesicles, long wait time, low success rate

2.5 nCNTP Conductance and Ion Selectivity

As briefly mentioned above, to evaluate ionic transport through nCNTPs (*ca.* 0.76 nm in diameter), we utilized the modified planar lipid bilayer measurement platform (Fig. 2.16A), which had *ca.* 100 nm diameter SiN_x solid-state nanopore over which we burst a CNTP-containing vesicle. This setup provided significant advantages over the more standard painted lipid bilayer setup that we had previously used[64]: (i) the smaller lipid bilayer area drastically improved the overall stability and noise levels and (ii) the setup also allowed us to form solvent-free lipid bilayers, which improved CNTP stability in the bilayer (additional comparisons between both methods are given in Table 2.1). This setup also makes it easier to incorporate a single CNTP into the lipid bilayer, as the CNTP density can be adjusted in the lipid vesicle to match the area of the solid-state nanopore aperture. Using this approach, we were able to repeatedly produce suspended bilayers with a single CNTP within the nanopore aperture area, with a success rate of ~40%. We observed that a single CNTP increased the bilayer conductance by 69 ± 6 pS (Fig. 2.16, B and C), matching the values of the conductance obtained while monitoring spontaneous stepwise insertions of individual nCNTPs into the painted planar lipid bilayer.

We have also been able to probe the relationship between ion conductance through CNTPs and electrolyte (KCl) concentration by measuring the conductance across a bilayer containing multiple nCNTPs. At pH 7.5, as the KCl concentration increased up to 250 mM, nCNTP conductance increased monotonically, and thereafter began to saturate at higher concentrations (Fig. 2.16D). Conductance saturation at high ionic strengths is commonly observed for biological ion channels that force water and ions into a single-file arrangement.[65] In these channels, interactions of the ions with the charged groups on the protein lead to a conductance versus concentration dependence that can be described by a Michaelis-Menten kinetics.[65] At moderate and high ionic strengths, the interactions of potassium ions with the negatively charged carboxylic groups at the CNTP rim result in that CNTP conductances follow the same Michaelis-Menten kinetics. Meanwhile at low salt concentrations, the conductance, *C*, of nCNTPs follows a distinct $C^{1/2}$ dependence (Fig. 2.16D, inset). Notably, the conductance scaling that we observed is distinctly different from the $C^{1/3}$ dependence reported for larger 14 - 3.5 nm diameter

CNTs at low concentrations;[66] however $C^{1/2}$ dependence was recently observed in very long 1.3 - 1.5 nm diameter CNTPs.[67] Further discussion on conductance scaling are included in chapter 3.

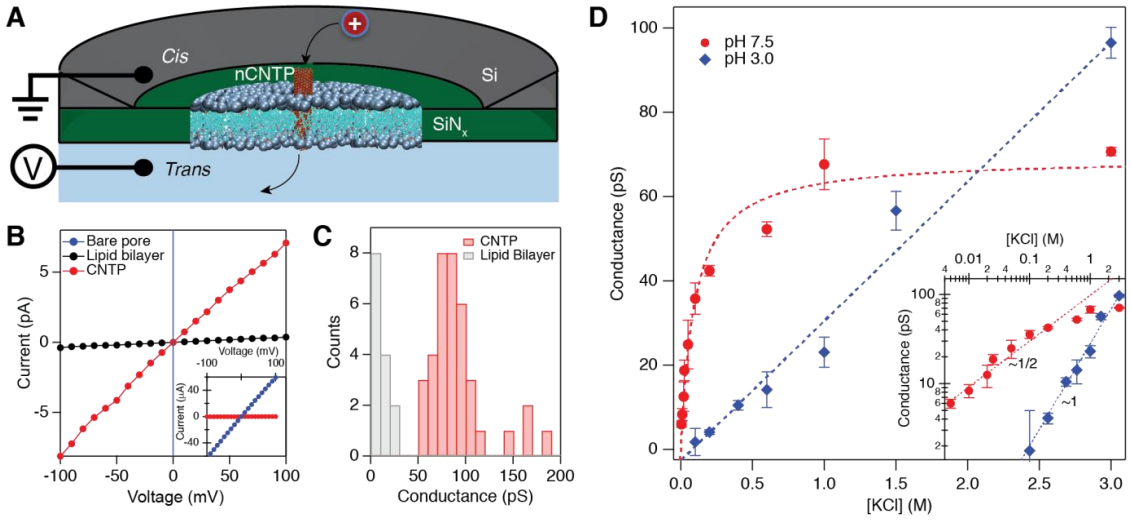

Figure 2.16. Ionic conductance of individual nCNTPs. (**A**) Schematic of the measurement setup showing a single nCNTP inserted into a small (*ca.* 100 nm diameter) patch of lipid bilayer spanning the aperture of a solid state nanopore. (**B**) Current-voltage characteristics (I-V curves) measured for a bare nanopore (blue), nanopore sealed with lipid bilayer (black), and nanopore sealed with the lipid bilayer containing a single CNTP. The initial high conductance of the nanopore (600 nS, blue) drops to less than 6 pS at 1M KCl upon sealing with the lipid bilayer (black), however when the seal contains a CNTP, the overall conductance reaches much higher values (red). (**C**) Histogram of the conductance values measured for individual CNTPs (red bars) compared with those measured for pure lipid bilayer seals (grey bars). (**D**) Conductance of individual CNTPs measured in KCl solutions of different concentrations at pH 7.5 (red circles) and pH 3.0 (blue diamonds). Dashed lines indicate fits to a Michaelis-Menten type conductance model (pH 7.5 data) and to a simple linear conductance model (pH 3.0 data). Inset: Conductance data plotted on a logarithmic scale with dashed lines indicating power law fits to the data. The fit at pH 7.5 uses data points at concentrations $\leqq$ 0.2 M. Image adapted with permission from ref [8].

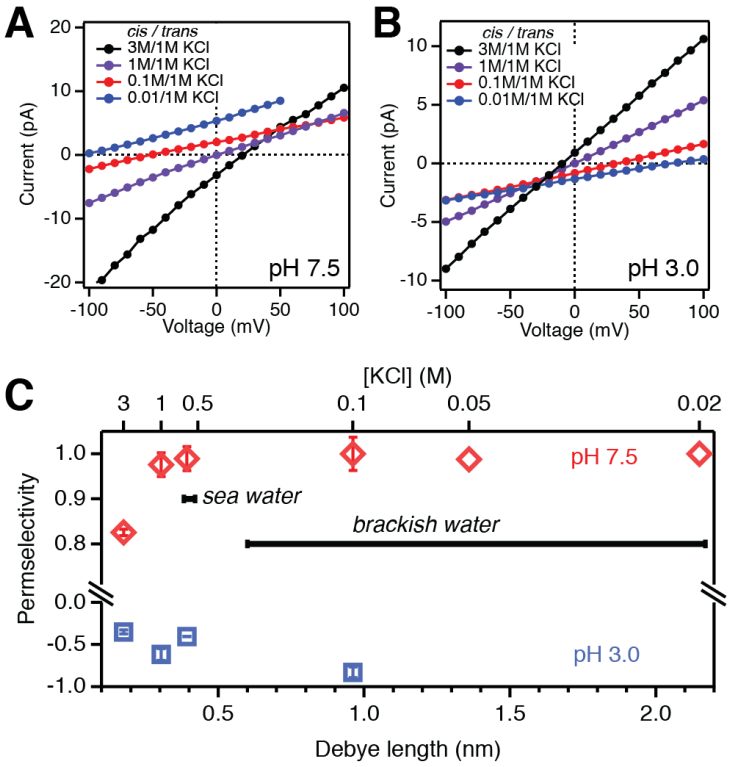

Figure 2.17. Ion selectivity in nCNTPs. (**A, B**) Asymmetric IV curves for nCNTPs where the *cis* and *trans* chambers contained different concentrations of KCl electrolyte at pH 7.5 (A) and 3.0 (B). Permselectivity values were estimated from the values of reversal potential, which is the fitted x-intercept for each curve. (**C**) Permselectivity values obtained from reversal potential measurements at pH 7.5 and 3.0 plotted as a function of the Debye length for the KCl electrolyte in the high salt chamber. Permselectivity values represent an average of several experiments where the KCl concentration in the high salt chamber has been held at a fixed value (as plotted on the top axis), and the lower salt chamber was held at values below the half the KCl concentration in the high salt chamber. Horizontal lines indicate typical salinity ranges for seawater and brackish water. Image adapted with permission from ref [8]. Copyright © 2017, The American Association for the Advancement of Science.

Reversal potential measurements, where the two sides of the CNTP embedded in a lipid bilayer are exposed to different salt concentrations, allowed us to determine the ion selectivity of the CNTPs and further rationalize its conductance behavior. When these measurements were carried out at pH 7.5 (Fig. 2.17), the nCNTPs were almost exclusive cation conductors with a permselectivity value approaching ~0.99, which corresponds to

a ratio of more than 184:1 K^+:Cl^- ion selectivity in salt concentrations similar to sea water values (600 mM). Thus, the conductance characteristics of nCNTPs satisfy the "good co-ion exclusion" conditions,[68] where the negatively-charged CNTP contains almost exclusively counterions (K^+ ions in our case). This is in agreement with what is expected based off the $C^{1/2}$ scaling of the channel conductance observed in our experiments. Furthermore, permselectivity values measured at different electrolyte concentrations show that strong anion exclusion in nCNTPs persists even at rather high ionic strengths up to 1 M salinity (Fig. 2.17C). In fact, the selectivity only starts to diminish at very high salt concentrations (*ca.* 2M). This observation of robust ion selectivity in narrow diameter carbon nanotubes in conditions that approach and exceed seawater salinity is encouraging for the potential water purification applications of this material.

2.6 End-Group Charge Effects and Current Rectifications

We can further corroborate these conclusions by exploring the nCNTP ion conductance and ion selectivity in acidic conditions where the pore ends are uncharged. Conductance for nCNTPs measured at pH 3.0 (Fig. 2.16D) did not show saturation behavior and remained proportional to the ion concentration across the entire range of ion concentrations. Moreover, the reversal potential measurements of the nCNTPs at pH 3.0 (Fig. 2.17B) showed a weak preference to anions over cations, which is in strong contrast to the behavior observed at pH 7.5 (Fig. 2.17C). We speculate that the weak anion selectivity at acidic pH values could be attributed to proton adsorption on the inside of the CNTP sidewalls.

Finally, we demonstrated that nCNTPs can be configured to behave as ionic diodes by exploiting their tunable ion selectivity. When both sides of the CNTP were exposed to 100 mM KCl at pH 7.5, the CNTPs showed a resistor-like linear I-V characteristic (Fig. 2.18). However, when the solution on one side of the bilayer was acidified to pH 3.0, the CNTP showed a highly rectifying diode-like I-V characteristic, indicating unidirectional ion transport. Furthermore, this ionic diode could be reversed by reversing the direction of the pH gradient (Fig. 2.18). The transition between the resistor and diode behavior was

robust and could be subjected to repeated switching, highlighting the potential of CNTPs within dynamically reconfigurable ionic circuits.[69]

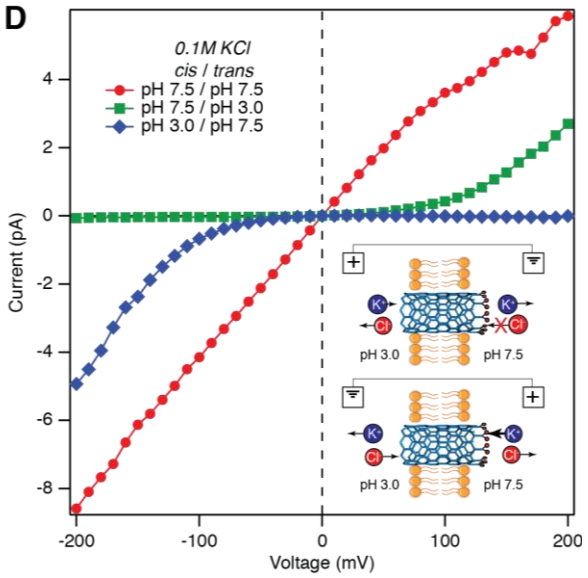

Figure 2.18. **nCNTP current rectification.** I-V curves recorded when different sides of the nCNTPs were exposed to a symmetric KCl concentration (100 mM) and asymmetric pH conditions (pH 7.5 and 3.0). Inset diagrams show ion flux direction at positive and negative applied voltages in the asymmetric pH case. Image adapted with permission from ref _ENREF_8. Copyright © 2017, The American Association for the Advancement of Science.

Acknowledgement

Many thanks to Dr. Robert Henley. He established the ionic transport measurement protocol in our lab and we worked together to collect most of the ionic transport measurements presented in this chapter.

References

1. Murata, K.; Mitsuoka, K.; Hirai, T.; Walz, T.; Agre, P.; Heymann, J. B.; Engel, A.; Fujiyoshi, Y., Structural determinants of water permeation through aquaporin-1. *Nature* **2000,** *407*, 599.
2. de Groot, B. L.; Grubmuller, H., Water permeation across biological membranes: mechanism and dynamics of aquaporin-1 and GlpF. *Science* **2001,** *294*, 2353.

3. Gravelle, S.; Joly, L.; Detcheverry, F.; Ybert, C.; Cottin-Bizonne, C.; Bocquet, L., Optimizing water permeability through the hourglass shape of aquaporins. *Proc. Natl. Acad. Sc.i U.S.A.* **2013,** *110*, 16367.
4. Saito, R.; Dresselhaus, G.; Dresselhaus, M. S., *Physical Properties of Carbon Nanotubes*. Imperial College Press 1998; p 272.
5. Dresselhaus, M.; Dresselhaus, G.; Avouris, P. In *Carbon nanotubes : synthesis, structure, properties, and applications*, 2001.
6. Geng, J.; Kim, K.; Zhang, J.; Escalada, A.; Tunuguntla, R.; Comolli, L. R.; Allen, F. I.; Shnyrova, A. V.; Cho, K. R.; Munoz, D.; Wang, Y. M.; Grigoropoulos, C. P.; Ajo-Franklin, C. M.; Frolov, V. A.; Noy, A., Stochastic transport through carbon nanotubes in lipid bilayers and live cell membranes. *Nature* **2014,** *514*, 612.
7. Tunuguntla, R. H.; Escalada, A.; V, A. F.; Noy, A., Synthesis, lipid membrane incorporation, and ion permeability testing of carbon nanotube porins. *Nat. Protoc.* **2016,** *11*, 2029.
8. Tunuguntla, R. H.; Henley, R. Y.; Yao, Y. C.; Pham, T. A.; Wanunu, M.; Noy, A., Enhanced water permeability and tunable ion selectivity in subnanometer carbon nanotube porins. *Science* **2017,** *357*, 792.
9. Iijima, S., Helical microtubules of graphitic carbon. *Nature* **1991,** *354*, 56.
10. Iijima, S.; Ichihashi, T., Single-shell carbon nanotubes of 1-nm diameter. *Nature* **1993,** *363*, 603.
11. Bethune, D. S.; Kiang, C. H.; de Vries, M. S.; Gorman, G.; Savoy, R.; Vazquez, J.; Beyers, R., Cobalt-catalysed growth of carbon nanotubes with single-atomic-layer walls. *Nature* **1993,** *363*, 605.
12. Terrones, M., Science and Technology of the Twenty-First Century: Synthesis, Properties, and Applications of Carbon Nanotubes. *Annu. Rev. Mater. Res.* **2003,** *33*, 419.
13. Journet, C.; Maser, W. K.; Bernier, P.; Loiseau, A.; de la Chapelle, M. L.; Lefrant, S.; Deniard, P.; Lee, R.; Fischer, J. E., Large-scale production of single-walled carbon nanotubes by the electric-arc technique. *Nature* **1997,** *388*, 756.
14. Bernholc, J.; Brenner, D.; Buongiorno Nardelli, M.; Meunier, V.; Roland, C., Mechanical and Electrical Properties of Nanotubes. *Annu. Rev. Mater. Res.* **2002,** *32*, 347.
15. Dai, H., Nanotube Growth and Characterization. In *Carbon Nanotubes: Synthesis, Structure, Properties, and Applications*, Dresselhaus, M. S.; Dresselhaus, G.; Avouris, P., Eds. Springer Berlin Heidelberg: Berlin, Heidelberg, 2001; pp 29.
16. Thess, A.; Lee, R.; Nikolaev, P.; Dai, H.; Petit, P.; Robert, J.; Xu, C.; Lee, Y. H.; Kim, S. G.; Rinzler, A. G.; Colbert, D. T.; Scuseria, G. E.; Tománek, D.; Fischer, J. E.; Smalley, R. E., Crystalline Ropes of Metallic Carbon Nanotubes. *Science* **1996,** *273*, 483.
17. José-Yacamán, M.; Miki-Yoshida, M.; Rendón, L.; Santiesteban, J. G., Catalytic growth of carbon microtubules with fullerene structure. *Appl. Phys. Lett.* **1993,** *62*, 202.
18. Cheng, H. M.; Li, F.; Sun, X.; Brown, S. D. M.; Pimenta, M. A.; Marucci, A.; Dresselhaus, G.; Dresselhaus, M. S., Bulk morphology and diameter distribution of

single-walled carbon nanotubes synthesized by catalytic decomposition of hydrocarbons. *Chem. Phys. Lett.* **1998,** *289*, 602.
19. Kong, J.; Soh, H. T.; Cassell, A. M.; Quate, C. F.; Dai, H., Synthesis of individual single-walled carbon nanotubes on patterned silicon wafers. *Nature* **1998,** *395*, 878.
20. Yamada, T.; Namai, T.; Hata, K.; Futaba, D. N.; Mizuno, K.; Fan, J.; Yudasaka, M.; Yumura, M.; Iijima, S., Size-selective growth of double-walled carbon nanotube forests from engineered iron catalysts. *Nat. Nanotechnol.* **2006,** *1*, 131.
21. Fagan, J. A., Aqueous two-polymer phase extraction of single-wall carbon nanotubes using surfactants. *Nanoscale Adv.* **2019,** *1*, 3307.
22. Cao, G.; Chen, X., The effects of chirality and boundary conditions on the mechanical properties of single-walled carbon nanotubes. *Int. J. Solids Struct.* **2007,** *44*, 5447.
23. Mori, H.; Hirai, Y.; Ogata, S.; Akita, S.; Nakayama, Y., Chirality Dependence of Mechanical Properties of Single-Walled Carbon Nanotubes under Axial Tensile Strain. *Jpn. J. Appl. Phys.* **2005,** *44*, L1307.
24. Fan, Y.; Goldsmith, B. R.; Collins, P. G., Identifying and counting point defects in carbon nanotubes. *Nat. Mater.* **2005,** *4*, 906.
25. Weisman, R. B., Chapter 5 Optical spectroscopy of single-walled carbon nanotubes. In *Contemporary Concepts of Condensed Matter Science*, Saito, S.; Zettl, A., Eds. Elsevier: 2008; Vol. 3, pp 109.
26. Connell, M. J.; Bachilo, S. M.; Huffman, C. B.; Moore, V. C.; Strano, M. S.; Haroz, E. H.; Rialon, K. L.; Boul, P. J.; Noon, W. H.; Kittrell, C.; Ma, J.; Hauge, R. H.; Weisman, R. B.; Smalley, R. E., Band Gap Fluorescence from Individual Single-Walled Carbon Nanotubes. *Science* **2002,** *297*, 593.
27. Hartschuh, A.; Pedrosa Hn Fau - Peterson, J.; Peterson J Fau - Huang, L.; Huang L Fau - Anger, P.; Anger P Fau - Qian, H.; Qian H Fau - Meixner, A. J.; Meixner Aj Fau - Steiner, M.; Steiner M Fau - Novotny, L.; Novotny L Fau - Krauss, T. D.; Krauss, T. D., Single carbon nanotube optical spectroscopy. *ChemPhysChem* **2005**.
28. Bachilo, S. M.; Strano, M. S.; Kittrell, C.; Hauge, R. H.; Smalley, R. E.; Weisman, R. B., Structure-Assigned Optical Spectra of Single-Walled Carbon Nanotubes. *Science* **2002,** *298*, 2361.
29. Dresselhaus, M. S.; Dresselhaus, G.; Saito, R.; Jorio, A., Raman spectroscopy of carbon nanotubes. *Phys. Rep.* **2005,** *409*, 47.
30. Horner, A.; Zocher, F.; Preiner, J.; Ollinger, N.; Siligan, C.; Akimov, S. A.; Pohl, P., The mobility of single-file water molecules is governed by the number of H-bonds they may form with channel-lining residues. *Sci. Adv.* **2015,** *1*, e1400083.
31. Hummer, G.; Rasaiah, J. C.; Noworyta, J. P., Water conduction through the hydrophobic channel of a carbon nanotube. *Nature* **2001,** *414*, 188.
32. Horner, A.; Pohl, P., Single-file transport of water through membrane channels. *Faraday Discuss.* **2018,** *209*, 9.
33. Qiao, R.; Aluru, N. R., Ion concentrations and velocity profiles in nanochannel electroosmotic flows. *J. Chem. Phys.* **2003,** *118*, 4692.
34. Majumder, M.; Chopra, N.; Andrews, R.; Hinds, B. J., Nanoscale hydrodynamics: enhanced flow in carbon nanotubes. *Nature* **2005,** *438*, 44.

35. Tabakman, S. M.; Welsher, K.; Hong, G.; Dai, H., Optical Properties of Single-Walled Carbon Nanotubes Separated in a Density Gradient: Length, Bundling, and Aromatic Stacking Effects. *The Journal of Physical Chemistry C* **2010,** *114*, 19569.
36. Simpson, J. R.; Fagan, J. A.; Becker, M. L.; Hobbie, E. K.; Hight Walker, A. R., The effect of dispersant on defects in length-separated single-wall carbon nanotubes measured by Raman spectroscopy. *Carbon* **2009,** *47*, 3238.
37. Joseph, S.; Aluru, N. R., Why are carbon nanotubes fast transporters of water? *Nano Lett.* **2008,** *8*, 452.
38. Tunuguntla, R. H.; Allen, F. I.; Kim, K.; Belliveau, A.; Noy, A., Ultrafast proton transport in sub-1-nm diameter carbon nanotube porins. *Nat. Nanotechnol.* **2016,** *11*, 639.
39. Lin, S.; Blankschtein, D., Role of the Bile Salt Surfactant Sodium Cholate in Enhancing the Aqueous Dispersion Stability of Single-Walled Carbon Nanotubes: A Molecular Dynamics Simulation Study. *J. Phys. Chem. B* **2010,** *114*, 15616.
40. Arnold, M. S.; Stupp, S. I.; Hersam, M. C., Enrichment of Single-Walled Carbon Nanotubes by Diameter in Density Gradients. *Nano Lett.* **2005,** *5*, 713.
41. Pagani, G.; Green, M. J.; Poulin, P.; Pasquali, M., Competing mechanisms and scaling laws for carbon nanotube scission by ultrasonication. *Proc. Natl. Acad. Sc.i U.S.A.* **2012,** *109*, 11599.
42. Lucas, A.; Zakri, C.; Maugey, M.; Pasquali, M.; van der Schoot, P.; Poulin, P., Kinetics of Nanotube and Microfiber Scission under Sonication. *J. Phys. Chem. C* **2009,** *113*, 20599.
43. Sun, X.; Zaric, S.; Daranciang, D.; Welsher, K.; Lu, Y.; Li, X.; Dai, H., Optical properties of ultrashort semiconducting single-walled carbon nanotube capsules down to sub-10 nm. *J. Am. Chem. Soc.* **2008,** *130*, 6551.
44. Regan, D.; Williams, J.; Borri, P.; Langbein, W., Lipid Bilayer Thickness Measured by Quantitative DIC Reveals Phase Transitions and Effects of Substrate Hydrophilicity. *Langmuir* **2019,** *35*, 13805.
45. Fagan, J. A.; Simpson, J. R.; Bauer, B. J.; Lacerda, S. H.; Becker, M. L.; Chun, J.; Migler, K. B.; Walker, A. R.; Hobbie, E. K., Length-dependent optical effects in single-wall carbon nanotubes. *J. Am. Chem. Soc.* **2007,** *129*, 10607.
46. Simien, D.; Fagan, J. A.; Luo, W.; Douglas, J. F.; Migler, K.; Obrzut, J., Influence of nanotube length on the optical and conductivity properties of thin single-wall carbon nanotube networks. *ACS Nano* **2008,** *2*, 1879.
47. Li, Y.; Wu, X.; Kim, M.; Fortner, J.; Qu, H.; Wang, Y., Fluorescent Ultrashort Nanotubes from Defect-Induced Chemical Cutting. *Chem. Mater.* **2019,** *31*, 4536.
48. Kuang, Y.; Liu, J.; Sun, X., Ultrashort single-walled carbon nanotubes: Density gradient separation, optical property, and mathematical modeling study. *J. Phys. Chem. C* **2012,** *116*, 24770.
49. Tunuguntla, R. H.; Chen, X.; Belliveau, A.; Allen, F. I.; Noy, A., High-Yield Synthesis and Optical Properties of Carbon Nanotube Porins. *J. Phys. Chem. C* **2017,** *121*, 3117.
50. Tuschel, D., Selecting an excitation wavelength for raman spectroscopy. *Spectroscopy* **2016,** *31*, 14.

51. Fornasiero, F.; In, J. B.; Kim, S.; Park, H. G.; Wang, Y.; Grigoropoulos, C. P.; Noy, A.; Bakajin, O., pH-tunable ion selectivity in carbon nanotube pores. *Langmuir* **2010,** *26*, 14848.
52. Hafner, J. H.; Cheung, C. L.; Woolley, A. T.; Lieber, C. M., Structural and functional imaging with carbon nanotube AFM probes. *Progress in Biophysics and Molecular Biology* **2001,** *77*, 73.
53. Yao, Y.-C.; Taqieddin, A.; Alibakhshi, M. A.; Wanunu, M.; Aluru, N. R.; Noy, A., Strong electroosmotic coupling dominates ion conductance of 1.5 nm diameter carbon nanotube porins. *ACS Nano* **2019,** *13*, 12851.
54. Tunuguntla, R. H.; Zhang, Y.; Henley, R. Y.; Yao, Y. C.; Pham, T. A.; Wanunu, M.; Noy, A., Response to Comment on "Enhanced water permeability and tunable ion selectivity in subnanometer carbon nanotube porins". *Science* **2018,** *359*.
55. Tunuguntla, R. H.; Hu, A. Y.; Zhang, Y.; Noy, A., Impact of PEG additives and pore rim functionalization on water transport through sub-1 nm carbon nanotube porins. *Faraday Discuss.* **2018,** *209*, 359.
56. Li, Z.; Li, Y.; Yao, Y. C.; Aydin, F.; Zhan, C.; Chen, Y.; Elimelech, M.; Pham, T. A.; Noy, A., Strong differential monovalent anion selectivity in narrow diameter carbon nanotube porins. *ACS Nano* **2020,** *14*, 6269.
57. Li, Y.; Li, Z.; Aydin, F.; Quan, J.; Chen, X.; Yao, Y. C.; Zhan, C.; Chen, Y.; Pham, T. A.; Noy, A., Water-ion permselectivity of narrow-diameter carbon nanotubes. *Sci. Adv.* **2020,** *6*.
58. Tunuguntla, R.; Henley, R.; Yao, Y.-C.; Pham, T. A.; Wanunu, M.; Noy, A., Enhanced water permeability and tunable ion selectivity in sub-nanometer carbon nanotube porins. *Science* **2017,** *357*, *792*.
59. Gutsmann, T.; Heimburg, T.; Keyser, U.; Mahendran, K. R.; Winterhalter, M., Protein reconstitution into freestanding planar lipid membranes for electrophysiological characterization. *Nat. Protoc.* **2015,** *10*, 188.
60. Cremer, P. S.; Boxer, S. G., Formation and Spreading of Lipid Bilayers on Planar Glass Supports. *J. Phys. Chem. B* **1999,** *103*, 2554.
61. Keller, C. A.; Glasmästar, K.; Zhdanov, V. P.; Kasemo, B., Formation of Supported Membranes from Vesicles. *Phys. Rev. Lett.* **2000,** *84*, 5443.
62. Gu, L.-Q.; Dalla Serra, M.; Vincent, J. B.; Vigh, G.; Cheley, S.; Braha, O.; Bayley, H., Reversal of charge selectivity in transmembrane protein pores by using noncovalent molecular adapters. *Proc. Natl. Acad. Sc.i U.S.A.* **2000,** *97*, 3959.
63. Myers, V. B.; Haydon, D. A., Ion transfer across lipid membranes in the presence of gramicidin A: II. The ion selectivity. *Biochim. Biophys. Acta* **1972,** *274*, 313.
64. Tunuguntla, R. H.; Escalada, A.; A Frolov, V.; Noy, A., Synthesis, lipid membrane incorporation, and ion permeability testing of carbon nanotube porins. *Nat. Protocols* **2016,** *11*, 2029.
65. Nelson, P. H., A permeation theory for single-file ion channels: Corresponding occupancy states produce Michaelis–Menten behavior. *J. Chem. Phys.* **2002,** *117*, 11396.
66. Secchi, E.; Niguès, A.; Jubin, L.; Siria, A.; Bocquet, L., Scaling behavior for ionic transport and its fluctuations in individual carbon nanotubes. *Physical Review Letters* **2016,** *116*, 154501.

67. Amiri, H.; Shepard, K. L.; Nuckolls, C.; Hernández Sánchez, R., Single-walled carbon nanotubes: mimics of biological ion channels. *Nano Lett.* **2017,** *17*, 1204.
68. Biesheuvel, P.; Bazant, M., Analysis of ionic conductance of carbon nanotubes. *Physical Review E* **2016,** *94*, 050601.
69. Ramirez, P.; Gomez, V.; Cervera, J.; Nasir, S.; Ali, M.; Ensinger, W.; Siwy, Z.; Mafe, S., Voltage-controlled current loops with nanofluidic diodes electrically coupled to solid state capacitors. *RSC Advances* **2016,** *6*, 54742.

Chapter 3. Ionic Transport through wCNTP

Extreme confinement in nanometer-sized channels can alter fluid and ion transport in significant ways, leading to significant water flow enhancement and unusual ion correlation effects. These effects are especially pronounced in carbon nanotube porins (CNTPs) that combine strong confinement in the inner lumen of carbon nanotubes with the high slip flow enhancement due to smooth hydrophobic pore walls. We have studied ion transport and ion selectivity in 1.5 nm diameter CNTPs (wCNTP) embedded in lipid membranes using as single nanopore measurement setup. Our data show that these CNTPs are weakly cation selectivity at pH 7.5 and become nonselective at pH 3.0. Ionic conductance of CNTPs exhibits an unusual 2/3 power law scaling with the electrolyte concentration. Coupled Navier-Stokes and Poisson-Nernst-Planck simulations and molecular dynamics simulations reveal that this scaling originates from strong coupling between water and ion transport in the channels. These effects could result in developments of next generation biomimetic membranes and carbon nanotube-based electroosmotic pumps.

3.1 Introduction

Ion transport and associated ionic equilibria feature prominently in a variety of condensed phase phenomena from energy storage in batteries[1] and colloidal stability[2] in materials science, to plant growth[3] and nerve signal propagation in biology.[4] A large number of these phenomena involves ion traveling through and interacting in confined spaces that typically reaches nanoscale dimensions. Extensive studies of colloidal and electrokinetic phenomena have revealed a detailed picture of ion interactions at distances from hundreds to tens of nanometers,[5, 6] and the development of microfluidics has taught us much about the dynamics of fluid and ion transport in channels in this size regime.[6] At the same time, biophysicists who studied transport in biological ion channels were

revealing efficient transport mechanism and unusual selectivity patterns of sub-nanometer diameter nanopores where water is squeezed down to molecular dimensions and often adopts single file configuration that is drastically different from that of the bulk state.[7] A number of those effects and mechanisms were reproduced and validated in synthetic model nanofluidic channels.[8, 9]

Yet, we still lack detailed knowledge of water and ion behavior in the channels that fall into the intermediate regime of 1-10 nm pore size. These "single digit nanopores" are small enough to severely confine the ions and fluid, yet still too large to force the dramatic hydrogen bond rearrangement of water molecules and partial loss of ion hydration shells that characterizes transport in single-file channels.[6] The existing studies of transport in these channels have already revealed a wealth of interesting physical phenomena including enhanced water transport in carbon nanotubes (CNTs),[9, 10, 11] strong electroosmotic coupling in boron nitride nanotubes,[12] and unusual modes of water transport in graphene and graphene oxide based membranes.[13, 14] Ion transport studies also revealed scaling relationships[15] that deviated from the concentration scaling expected for microchannels.[16, 17] To study the details of these phenomena we need model systems that offer reproducible and consistent channel features covering this size regime. CNTs are good candidates for such model channels because of their relatively simple structure – smooth hydrophobic inner channel surface and the localized controllable charges at the pore entrances[18] – and well-defined diameters that fall squarely into the "single digit nanopore" range. Simulations and experimental studies of water and ion transport in CNT pores showed fast high-slip water flow,[8, 9, 11, 19] unusual ion selectivity and conductance scaling,[9, 15] and electrophoretically-induced water flows.[20]

We have recently reported carbon nanotube porins (CNTPs)[9, 21, 22] —ultra-short CNT fragments that can self-insert into the lipid bilayers and form biomimetic membrane pores. Our previous studies showed that 0.8 nm diameter CNTPs (nCNTPs), which force water into a single file configuration,[9] show highly non-linear conductance vs. ion concentration characteristics attributed to the ion interactions with the negatively charged carboxyl groups at the CNTP entrance. This negative charge was also responsible for the very high cation selectivity of these channels and at low ion concentrations the pore

conductance followed the $c^{1/2}$ concentration scaling characteristic for the good co-ion exclusion conditions.[9, 23] In this work we report the ion conductance characteristics and selectivity of the wider 1.5 nm diameter CNTPs (wCNTPs), compare measured ion transport behavior with that of the narrower nCNTPs and study the effects of the charge on the CNTP entrance on the ion conductance. We also perform continuum simulations using Navier-Stokes and Poisson-Nernst-Planck (NS-PNP) model and molecular dynamics (MD) simulations to show that the dominant contribution to the power law scaling of the concentration-ionic conductance relation comes from the electroosmotic coupling effects. The overall physical picture that emerges shows tightly coupled water and ion flows in these nanopores.

3.2 wCNTP Conductance Measurements

We synthesized wCNTPs using sonication-assisted cutting of μm-long CNT feed stocks in presence of lipid molecules, which stabilized cut CNTs in water. For measuring ion conductance of individual CNTPs we used a modified planar lipid bilayer setup (Fig. 3.1A) that we developed for our previous studies. This setup was based on a small *ca.* 100 nm diameter nanopore etched in a thin SiN_x film supported over a larger opening on a silicon wafer.[9] SiN_x film provides clean hydrophilic surface onto which we fused lipid vesicles containing CNTPs. This platform offers several significant advantages over traditional planar lipid membrane platforms, including the ability to control the number of CNTPs in the bilayer, reduction in the bilayer undulations and the associated noise, and the ability to use completely solvent-free bilayers. Current-voltage (I-V) curves recorded for wCNTPs in this setup (Fig. 3.1B, C) were symmetric and showed linear dependence on applied voltage over two decades of KCl electrolyte concentrations, indicating that the dominant charge carrier ion species did not encounter a significant energy barrier when entering the nanotube pore.[24] wCNTP conductance at 1M KCl concentration, measured from the slope of the I-V curve, 766 ± 49 pS, was close to the value of 630 ± 120 pS which we measured previously from the current jumps corresponding to the spontaneous wCNTP incorporation into lipid bilayer in a traditional

planar lipid bilayer setup.[21] We attribute the slightly higher conductance value obtained in our current experiments to the use of solvent-free bilayers.

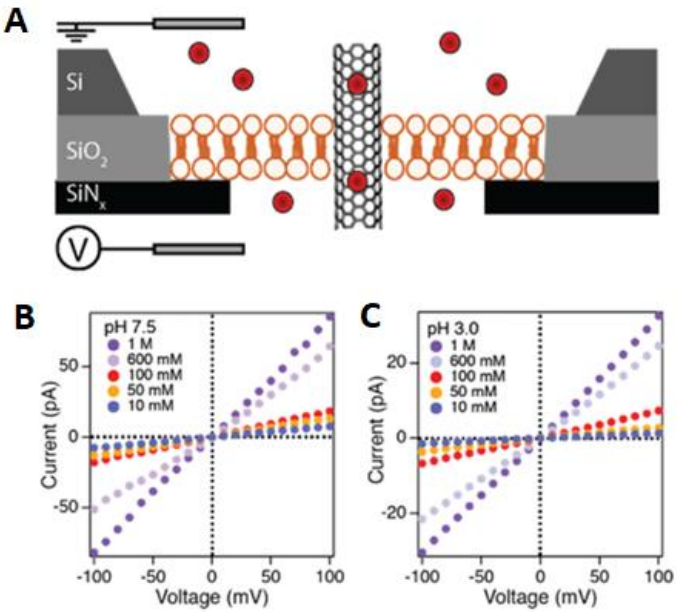

Figure 3.1. Ionic conductance of 1.5 nm diameter wCNTPs. (**A**) Schematics of the experimental setup where a small area lipid bilayer with a single CNTP is formed over a SiN_x nanopore. (**B, C**) I-V curves recorded for individual CNTPs at different KCl concentrations at pH 7.5 (B) and at pH 3.0 (C).

3.3 wCNTP Conductance Scaling

wCNTP conductance exhibited a pronounced non-linear dependence as a function of the KCl electrolyte concentration (Fig. 3.2A). For most of the ion concentration range conductance values followed a power law dependence with the exponent very close to the value of 2/3. This apparent 2/3 power law scaling is qualitatively different from the linear conductance dependence expected for ideal channels; it does not show the limiting surface conductance behavior of typical nanochannels with charged surfaces;[25] and it is also distinct from the conductance scaling reported previously for carbon nanotube channels.[15,17] It is reasonable that wCNTPs would not show the conductance saturation behavior of nCNTPs at high salt concentrations, which arises from a combination of single-file geometry of that channels and charged groups at the nanotube entrance. Our

data also do not follow the $c^{1/2}$ scaling reported by Nuckolls and colleagues for longer CNT channels with the similar 1.5 nm diameter,[17] or the $c^{1/3}$ scaling measured by Bocquet and colleagues in larger 7-70 nm diameter CNTs.[15]

To elucidate the influence of the negative charges that usually decorate nanotube entrance on the ion transport through wCNTPs, we measured their conductance characteristics at pH 3.0 where the carboxylate (-COO^-) groups at the CNTP rim protonate and become neutral (-COOH).[26, 27] I-V curves measured at pH 3.0 conditions (Fig. 3.1C) also showed linear behavior at all tested values of electrolyte concentrations, indicating that the entrance charges do not contribute significantly to the pore entrance barriers. Notably, overall conductance at pH 3.0 is reduced relative to the values measured at pH 7.5, which is qualitatively consistent with the trends observed in experiments and in models.[15, 23] This observation also rules out the possibility of protonic currents dominating CNTP conductance, unlike the behavior reported previously for ultra-long CNT channels of similar diameter.[28]

The exact physical model describing ion conductance scaling in carbon nanotube pores has been the subject of intense scrutiny in recent research literature. Bocquet and co-workers postulated that inner surfaces of nanotube pores bear some negative charge due to adsorption of hydroxyl ions,[29] and showed that charge regulation, combined with the Poisson-Nernst-Plank model for conductance, leads to the $c^{1/3}$ scaling of the ion conductance, a prediction that they confirmed experimentally by measuring ion conductance of large diameter (7-70 nm) carbon nanotubes.[15] Biesheuvel and Bazant described similar physics using a combined space-charge theory with the Donnan approximation and obtained an analytical expression for CNT conductance that predicted a limiting conductance scaling of $c^{1/2}$ at low ion concentrations,[23] the scaling that seems to be corroborated by the data of Nuckolls and co-workers on conductance of 1.5 nm diameter nanotubes incorporated into microfluidic measurement platform.[17] Recently Bonthuis and co-workers presented an detailed theoretical study that showed that conductance in nanotubes can exhibit several regimes characterized by power law exponents of 1, 1/3, or 1/2 and quantified the cross-over between those regimes.[30]

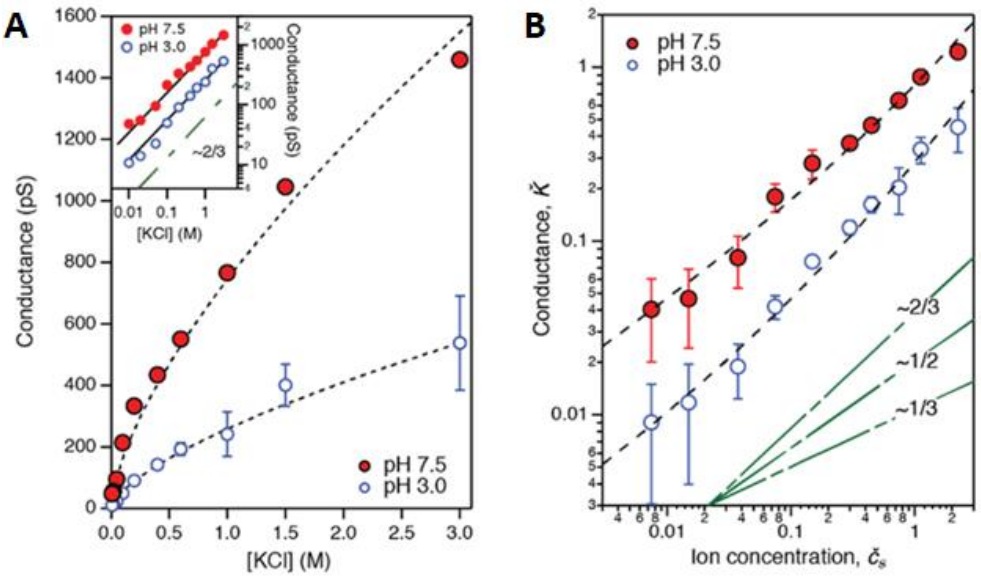

Figure 3.2 wCNTP conductance scaling. (**A**) Individual CNTP ionic conductance as a function of KCl concentration at pH 7.5 and pH 3.0. Inset shows the data plotted on a log-log scale. Lines on both graphs are best fits of the data to a power law. (**B**) Conductance vs KCl concentration data from (A) replotted in dimensionless coordinates defined by Eqs. 3.2 - 3.4. Dashed lines are best fits to Eq. 3.1. Green dash-dotted lines correspond to different power law scaling and are presented only as a guide to the eye.

Curiously, these models did not consider the nature of transport through carbon nanotubes that is characterized by very large wall slip and correspondingly very high rates of water transport.[9, 10, 11] One of the most interesting possibilities for ion transport in these pores is that large slip could lead to unusually high electro-osmotic and diffusion-osmotic coupling,[31, 32] which should be significantly enhanced for small diameter carbon nanotube pores that exhibit very high slip. Even though a number of previous theoretical works mentioned this possibility in passing or alluded to it,[23] most have neglected the contribution of the electroosmotic term to the overall conductance. A rigorous analysis of this case was done only recently by Manghi and colleagues, who solved the Poisson-Boltzmann equation for cylindrical pores in presence of charge regulation and high flow slip and identified several scaling regimes for conductivity.[32]

The most relevant of those regimes for our experiments is the low surface charge density regime, where the conductance arises from the combined contributions of a term

representing ion migration and a term representing slip-enhanced electroosmotic flow. Total conductance is then described as:

$$\check{K} = 2\check{\mu}\left(\frac{\sigma^*}{2h}\check{c}_s\right)^{1/2} + \left(1 + 4\check{b}\right)\frac{\sigma^*}{2h}\check{c}_s \qquad \text{Eq. 3.1}$$

where $\check{K}$ and $\check{c}_s$ are the dimensionless conductance and salt concentration, respectively, obtained from ion conductance, G, and electrolyte concentration, c_s as:

$$\check{K} = G \cdot \frac{2\pi L \cdot l_b^2 \cdot \eta}{e^2} \qquad \text{Eq. 3.2}$$

$$\check{c_s} = \pi \cdot l_b \cdot r^2 \cdot c_s \qquad \text{Eq. 3.3}$$

where L and r are the pore length and radius, l_b is the Bjerrum length, η is the dynamic viscosity of the water, and h is a pH-dependent factor. The additional dimensionless parameters are: σ^* the maximum surface charge density; $\check{\mu}$, the ion mobility; and $\check{b}$, the slip length (an empirical parameter defining the relative retardation of fluid velocity next to the fluid-wall interface) obtained from the corresponding dimensional parameters as:

$$\sigma^* = \frac{\pi R l_b}{e}\sigma; \quad \check{\mu} = 2\pi\eta l_b \mu; \quad \check{b} = \frac{b}{r} \qquad \text{Eq. 3.4}$$

Remarkably, Eq. 1 fits our wCNTP conductance data very well over the whole range of concentrations (Fig. 3.2B) at both pH values that we investigated, reproducing the approximately 2/3 power law scaling observed in the experiment. However, the fits also indicate that the fitted values of slip length, b, differ significantly at different pH, changing from 1.1 nm at pH 7.5 to as much as 19.1 nm at pH 3.0. This observation points to an interesting possibility that the slip length in CNT pores may be a strong function of pH. This notion of pH-dependent slip length is also consistent with the physical picture of OH^- ion adsorption on the CNT walls, where those charges disrupt the slip flow conditions on the perfectly smooth CNT walls. Indeed, we would expect that OH^- adsorption to be diminished at low pH values and produce larger effective slip lengths, which is consistent with the results of the fit. Our previous experimental data also showed enhanced water flow in 1.5 nm diameter CNTPs at acidic pH values. We also note that although the values of the slip lengths obtained in our fits are significantly smaller than values reported in the literature,[10, 11, 19] this discrepancy likely reflects the difference between μm-long CNTs channels used in those studies and the ultrashort nanotubes used in the current work.

3.4 Continuum Simulations

To investigate the contribution of electroosmotic coupling on the ionic conductance and to reduce reliance on the fitted parameters, we performed continuum simulations of the ion transport using the NS-PNP model and the concentration-surface charge dependence relation, $|\sigma| \sim c^{1/2}$.[23] First, we computed the concentration-conductance scaling by solving only the PNP equations. Next, we solved the same system using the coupled NS-PNP equations to account for the contribution of the electroosmotic flow. Here, we simulated a CNT with $d = 14\ nm$ and $L = 10\ nm$. The surface charge values are directly taken from in Biesheuvel and Bazant work for the same CNT size at pH=6.[23] When the contribution from the electroosmotic velocity is neglected, we observe a power law scaling with an exponent of *ca.* 0.49 (Fig. 3.3A), which followed the trend proposed by Biesheuvel and Bazant.[23] When the velocity effect is included, we observed that the conductance-concentration scaling exponent shifts to higher values and follows a higher exponent of *ca.* 0.62, indicating that indeed, as we observed in the experiments and as Manghi and coworkers predicted by analytical modeling, the ionic conductance is enhanced due to electroosmotic effects.[32]

Next, we calibrated the surface charge on the CNTPs by matching the experimental data with conductance simulated using NS-PNP equations for the same CNT geometry (d =1.5 nm and L=10 nm). Unfortunately, we were limited to ion concentrations below 0.25 M because of convergence issues. The fitted surface charge values (Fig. 3.3B**)** are negative, increase with the concentration, and start to saturate around ion concentration of 0.1 M. As expected, the absolute value of the surface charge at pH 3.0 is lower than at pH 7.5, and, interestingly, the values at pH 3.0 and pH 7.5 are consistently within a factor of 2.2-2.5 within each other. The saturation starts to occur when the surface charge reaches a relatively high value, indicating that this phenomenon could result from cation accumulation inside CNTPs pores blocking additional ions from entering, and thus saturating the potential source of the surface charge. Note that our values for the wCNTP surface charge at pH 7.5, which range from -30 to -75 mC/m^2 (which roughly correspond to 10-20 charges over the CNTP surface), are lower than the -40 to -145 mC/m^2 values reported by Bieshuevel and Bazant for larger diameter CNT channels.[23]

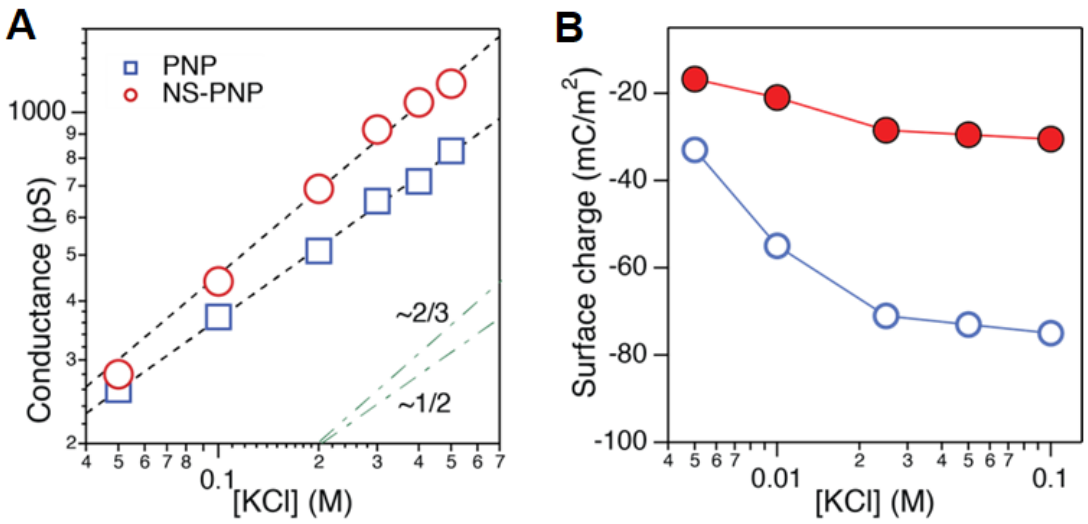

Figure 3.3. NS-PNP simulations of ion conductance in CNTPs. (A). Simulated conductance-concentration scaling in a carbon nanotube porin using PNP model (blue squares) and combined NS-PNP model (red circles). Dashed lines correspond to power law ($G \sim c^{\alpha}$) fits to the data with the slopes of $\alpha = 0.49$ for PNP and $\alpha = 0.62$ for NS-PNP. (**B**). Calibrated effective surface charge of a carbon nanotube porin of $d = 1.5\ nm$ and $L = 10\ nm$ based on the experimentally measured conductance at pH 3 (red circles) and at pH 7.5 (blue circles). Surface charge values were obtained from NS-PNP simulations and plotted as a function of ion concentration.

3.5 wCNTP Ion Selectivity

We have also studied the ion selectivity of wCNTPs using the reversal potential experiments where we measured the I-V characteristics of the CNTPs in asymmetric ion concentration conditions. We varied the electrolyte concentration in one of the chambers while leaving the concentration in the other chamber constant (Fig. 3.4). If a channel has some selectivity to one type of the ions, the I-V curve shifts and the potential value at which the current becomes zero (i.e. the reversal potential, V_{rev}) can determine the channel permselectivity, P. The value of the reversal potential was determined from the new zero-current voltage value and used to derive the ion selectivity using Goldman-Hodgkin-Katz (GHK) equation:[33, 34]

$$V_{rev} = (2t_+ - 1)\frac{RT}{F}\ln\frac{c_{top}}{c_{bottom}} \qquad \text{Eq. 3.5}$$

where V_{rev} is the reversal potential, t_+ is the effective transmembrane number of cation (percentage of cation transferring through membrane out of total ion transfer), *c* is the electrolyte concentration for either top or bottom chamber, R is the molar gas constant, T is the temperature, and F is the Faraday constant. The permselectivity (*P*) was then calculated using the cation transport number in bulk (t_{+bulk} = 0.49 for KCl solution) and the following equation:

$$P = \frac{t_+ - t_{+bulk}}{1 - t_{+bulk}} \qquad \text{Eq. 3.6}$$

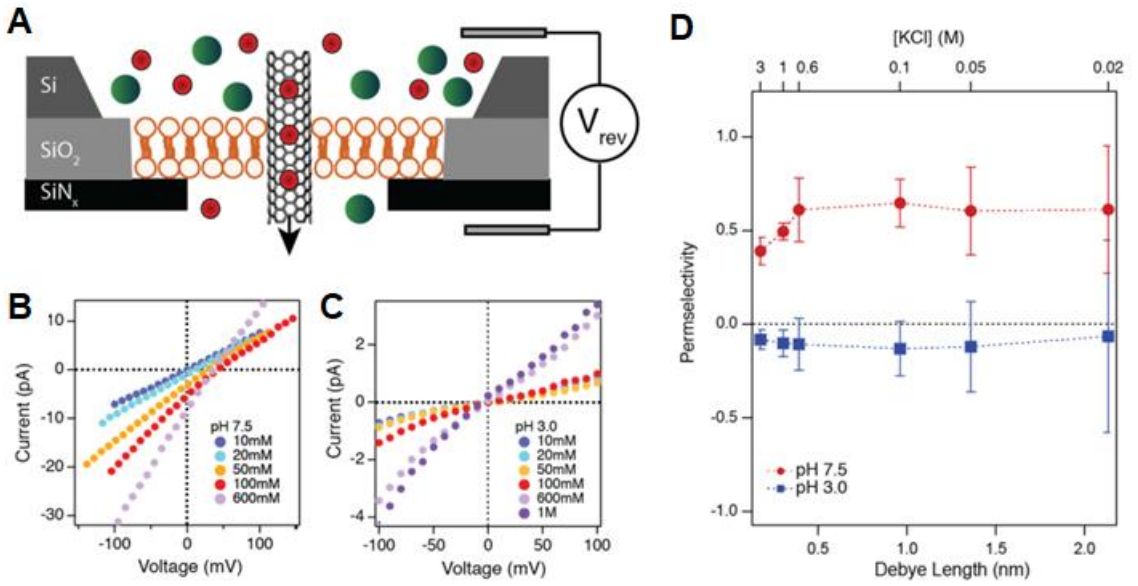

Figure 3.4. Ion selectivity of wCNTPs. (**A**) Schematics of the reversal potential measurements showing how preferential transport of one kind of ions across the membrane gives rise to an electric potential. (**B, C**) IV curves collected for the reversal potential measurements at pH 7.5 (B) and at pH 3.0 (C). For these experiments the bottom chamber always contained 10 mM KCl solution and the concentration of the KCl solution was as indicated on the legend. (**D**) Permselectivity values measured in these experiments plotted as a function of the Debye length and KCl concentration.

As we expected from a channel with the negatively-charged groups at the entrance, at pH 7.5, wCNTPs showed weak cation selectivity with the permselectivity of *ca.* 0.5, which indicates the cation/anion ratio to be 2-10 depending on the concentration.

Unsurprisingly, the channel permselectivity decreased slightly when KCl concentration reached values higher than 600 mM, where the entrance charges became strongly screened (Fig. 3.4D). At pH 3.0, wCNTPs permselectivity dropped down to zero, with the channel showing almost no selectivity between K^+ and Cl^- ions, confirming that the COO- groups at the pore rim were responsible for the channel selectivity at neutral pH values.[9]

We have also investigated the pore selectivity using NS-PNP simulations of the reversal potential experiments using 100 mM as the high concentration and varying the low concentration between 0.1 and 20 mM. The computed permselectivity, which were defined as the ratio of cation and anion currents obtained in the simulations, was 0.585 ± 0.037, which compares favorably with the average value of 0.619 ± 0.019 measured in the experiments at KCl concentrations below 1M.

3.6 Molecular Dynamics Simulation

To understand the molecular level details of the effect of the surface charge on ion transport in these channels we have performed non-equilibrium molecular dynamics simulations of the ion and water flow in CNTPs. The simulations (Fig. 3.5) showed that K^+ cations were rapidly entering and passing through the CNTP channel under an applied electric field of 50 mV/nm. The electroosmotic ion velocities observed in the simulations (Table 3.1) were quite high owing to the relatively large values of the applied electric field. The cation transport was also accompanied by significant overall flow of water through the channel in the direction of the ion travel. Computed trajectories (Fig. 2.5B) and velocities of water and potassium ions (Table 3.1), are strongly correlated, indicating that there is a significant overall water flux in the direction of the ion travel, again illustrating the extreme degree of electroosmotic coupling in these channels. Data in Table 3.1 indicate that water and ion velocities stay constant for low surface charge densities, e.g., for σ =–27 and σ =–54 mC/m^2. However, as the surface charge density increases to σ =–118 mC/m^2; the velocities of both water molecules and potassium ions decrease, indicating that for higher surface charge densities, increased adsorption of

cations to the CNTP walls can frustrate the slip conditions and cause the flow velocities to decrease.

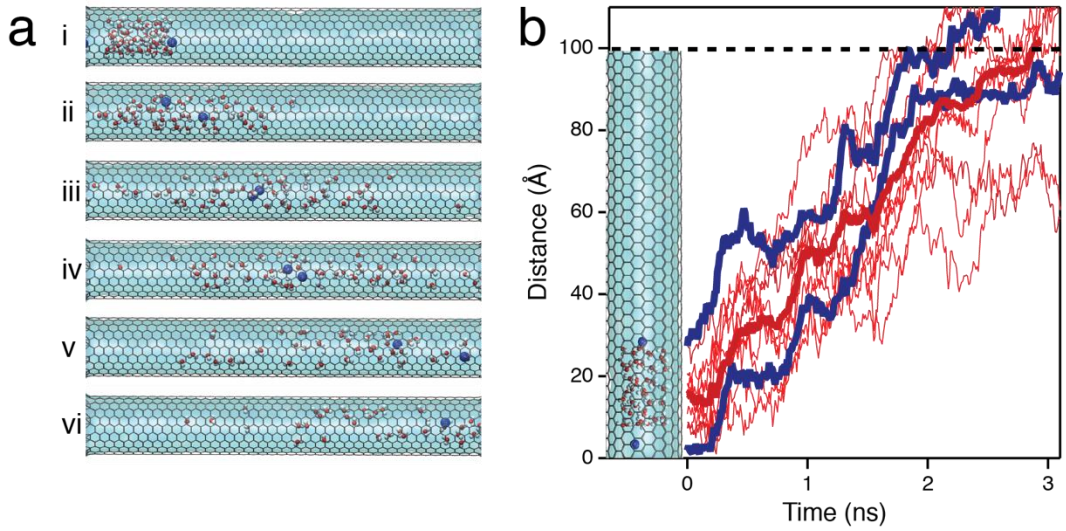

Figure 3.5. MD simulations of water and ion transport in CNTPs. (**A**) Snapshots from MD simulations of water and ion transport in 1.5 nm CNTP under an applied electric field showing two K^+ cations (blue) and several water molecules (red) as they move through the CNTP pore (from left to right). The snapshots are numbered sequentially, with the 0.5 ns interval between adjacent frames covering the total duration of 3 ns. (**B**) Calculated trajectories of K^+ ions (thick blue lines) and water molecules (thin red lines). Thick red line corresponds to the average of 11 water molecule trajectories. The inset image shows the configuration of the system with K^+ ions and water molecules that are being tracked.

The calculated electroosmotic ion velocities allow us to estimate the electrophoretic mobility of K^+ ions in 1.5 nm CNTPs. We can interpolate the calculated ion velocities (Table 3.1) to the surface charge of *ca.* -70 mC/m^2, which would correspond to a relatively high ion concentration regime (Fig. 3.3B). This value (2.37m/s) at the value of applied field of 50 mV/nm corresponds to the electrophoretic mobility for K^+ ions of $4.9 \cdot 10^{-8}$ $m^2 \cdot V^{-1}s^{-1}$, which is about 40% lower than the bulk value of $7.6 \cdot 10^{-8}$ $m^2 \cdot V^{-1}s^{-1}$. Our value is also very close to the electrophoretic mobility of $5.0 \cdot 10^{-8}$ $m^2 \cdot V^{-1}s^{-1}$ reported by Hinds and colleagues for K^+ ion transport in the similar 1.5 nm diameter but significantly thicker (5 μm) SWCNT membranes.[35] Interestingly, in that study Hinds and colleagues did not observe significant electroosmotic flows in unmodified CNTs and had

to graft diazonium salts to the nanotube surface to enhance the surface charge, whereas our experiments and simulations indicate that electroosmotic effects remain significant even in unmodified CNT pores.

Table 3.1. Computed average velocity of water and potassium ions in (11,11) CNT with L = 10 nm at concentration of 1 M using molecular dynamics simulation

Surface charge (mC/m^2)	$\boldsymbol{u}_{water}$(m/s)	$\boldsymbol{u}_{K^+}$ (m/s)
-27	2.9 ± 0.29	2.31
-54	3.01 ± 0.28	2.45
-114	1.98 ± 0.42	2.15

Strong electroosmotic coupling that is pH-independent, high degree of fluid slip at the wCNTP walls leading to low friction flow through the pore, and very small pore length that produced high electric field values for relatively modest applied voltages all point out to the possibility to use unfunctionalized CNTPs as low-voltage electroosmotic pumps (EOPs). Indeed, our calculated water velocities in CNTPs provide an estimate of the electroosmotic transport figure of merit (FOM) of *ca.* 3.7 $mL \cdot cm^{-2} \cdot min^{-1} \cdot V^{-1}$. This value is at least an order of magnitude higher than the typical FOM values for low-voltage electroosmotic pumps based on porous Si,[36] and is the same order of magnitude as the value obtained for EOPs based on chemically-functionalized carbon nanotube membranes.[35]

3.7 Current Noise in wCNTPs

Fluctuation of ionic current can provide additional information about the dynamic processes inside the nanotube pores.[37, 38] Normalized power spectra of the ion current (Fig. 3.6) show the expected behavior where the large bare SiN_x pore shows the smallest relative noise, with the CNTP and lipid bilayer showing progressively larger relative noise. The noise spectra represent the combination of white noise, 1/f noise, and other

noises such as interactions at the channel entrance.[37, 39] The noise component that carries the most information about the ion current is the $1/f$ noise, which dominates the low-frequency regime (1-100 Hz), whereas the higher frequencies are dominated by white noise.[37] $1/f$ noise is observed in electronic current in metals and semiconductors and ionic currents in biological and artificial membrane channels.[40, 41] A common approach to analyzing $1/f$ noise is the Hooge's empirical relation, which was first proposed for electronic conductance in homogeneous samples, but later became well-accepted for analyzing ionic current through biological and solid-state nanopore system.[15, 40, 42]

$$\frac{S(f)}{I^2} = \frac{A}{f} = \frac{\alpha}{N}\frac{1}{f} \qquad \text{Eq. 3.7}$$

where $S(f)$ is power density, f is frequency, I is current, and A is noise amplitude, α is a parameter related to temperature and mobility,[38] and N is the number of charge carriers. Hooge's relation states that the normalized power density $S(f)/I^2$ is inversely proportional to the frequency and the proportionality coefficient, A, is itself inversely proportional to the number of charge carriers. Indeed, when we fitted our data to the Hooge's relationship (Eq. 3.7) and plotted the values of $1/A$ as a function of ion concentration we observed that they followed the same 2/3 power law dependence that we saw in ion current measurement (Fig. 3.6C). Interestingly, noise spectra obtained at pH 7.5 show the $1/f$ noise decreasing as the KCl concentration increased (Fig. 3.6B), which likely reflects the increased screening of charges at the pore entrance. Indeed, the noise spectra obtained at different concentrations of KCl at pH 3.0 (Fig. 3.6D), were the CNTP entrance charges are neutralized, do not show this trend and instead overlap one another.

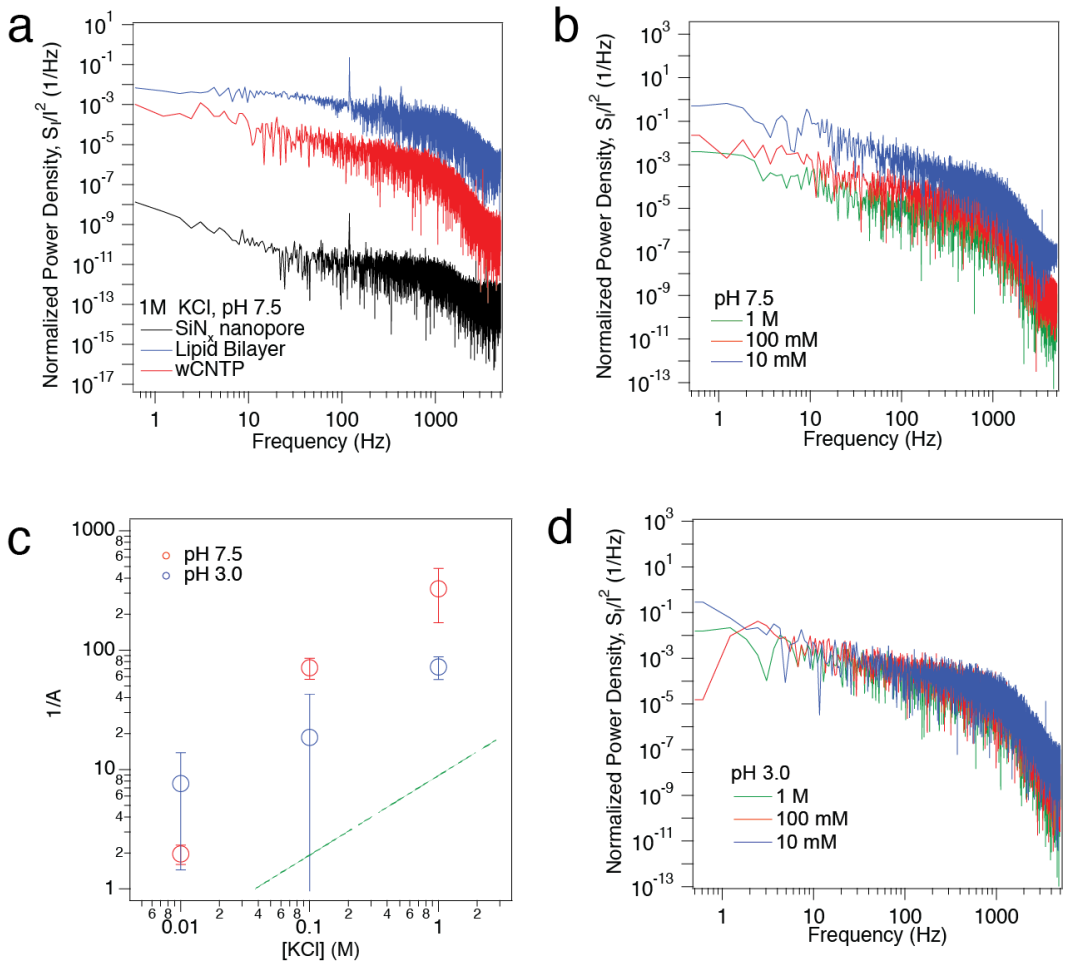

Figure 3.6. Ionic current noise in wCNTPs. (**a**) Normalized power spectra of bare SiN_x nanopore, SiN_x nanopore sealed with a lipid bilayer, and wCNTP measured for 1M KCl electrolyte concentration, +100 mV bias voltage, and pH 7.5. (**b, d**) Power spectra of wCNTP at pH 7.5 (b) and pH 3.0 (d) measured at different KCl concentrations. (**c**) Plot of the inverse values of the parameter *A* (see Eq. 5) fitted to the power spectra as a function of ion concentration. The green dash-dotted line is provided as a guide to the eye and corresponds to the 2/3 power law.

3.8 Conclusions

Our results indicate that ion conductance through 1.5 nm diameter carbon nanotubes is governed by a complex interplay of phenomena that involve confinement, wall slip, charge equilibria, and above all very strong electroosmotic transport coupling. Significantly, these effects lead to a characteristic $c^{2/3}$ conductance scaling with ion concentration. Continuum NS-PNP simulations and non-equilibrium molecular dynamics

simulations revealed the mechanism of this coupling at the molecular scale and provided estimates of electroosmotic transport velocities in this system that indicate that small diameter CNTPs could act as efficient electroosmotic pumping media. Our findings should also help researchers to design the next generations of membranes, separation systems, and microfluidic devices for the applications that require control over water and ion transport on the nanoscale.

Acknowledgement

Many thanks to Amir Taqieddin and Prof. Narayana Aluru for the simulation work (Section 3.4 and 3.6), Dr. Mohammad Alibakhshi and Prof. Meni Wanunu for support in SiN_x devices, and Dr. Robert Henley for establishing the measurement protocol.

References

1. Dunn, B.; Kamath, H.; Tarascon, J. M., Electrical energy storage for the grid: a battery of choices. *Science* **2011,** *334*, 928.
2. Plett, T.; Thai, M. L.; Cai, J.; Vlassiouk, I.; Penner, R. M.; Siwy, Z. S., Ion transport in gel and gel-liquid systems for LiClO4-doped PMMA at the meso- and nanoscales. *Nanoscale* **2017,** *9*, 16232.
3. Blumwald, E.; Aharon, G. S.; Apse, M. P., Sodium transport in plant cells. *Biochim. Biophys. Acta.* **2000,** *1465*, 140.
4. Hille, B., *Ion channels of excitable membranes*. 3rd ed.; Sinauer: Sunderland, Mass., 2001; p xviii.
5. Stein, D.; Kruithof, M.; Dekker, C., Surface-charge-governed ion transport in nanofluidic channels. *Phys. Rev. Lett.* **2004,** *93*, 035901.
6. Bocquet, L.; Charlaix, E., Nanofluidics, from bulk to interfaces. *Chem. Soc. Rev.* **2010,** *39*, 1073.
7. Horner, A.; Pohl, P., Single-file transport of water through membrane channels. *Faraday Discuss.* **2018,** *209*, 9.
8. Hummer, G.; Rasaiah, J. C.; Noworyta, J. P., Water conduction through the hydrophobic channel of a carbon nanotube. *Nature* **2001,** *414*, 188.
9. Tunuguntla, R.; Henley, R.; Yao, Y.-C.; Pham, T. A.; Wanunu, M.; Noy, A., Enhanced water permeability and tunable ion selectivity in sub-nanometer carbon nanotube porins. *Science* **2017,** *357, 792*.
10. Holt, J. K.; Park, H. G.; Wang, Y.; Stadermann, M.; Artyukhin, A. B.; Grigoropoulos, C. P.; Noy, A.; Bakajin, O., Fast Mass Transport Through Sub-2-Nanometer Carbon Nanotubes. *Science* **2006,** *312*, 1034.
11. Secchi, E.; Marbach, S.; Niguès, A.; Stein, D.; Siria, A.; Bocquet, L., Massive radius-dependent flow slippage in carbon nanotubes. *Nature* **2016,** *537*, 210.

12.Siria, A.; Poncharal, P.; Biance, A. L.; Fulcrand, R.; Blase, X.; Purcell, S. T.; Bocquet, L., Giant osmotic energy conversion measured in a single transmembrane boron nitride nanotube. *Nature* **2013,** *494*, 455.
13. Esfandiar, A.; Radha, B.; Wang, F. C.; Yang, Q.; Hu, S.; Garaj, S.; Nair, R. R.; Geim, A. K.; Gopinadhan, K., Size effect In Ion transport through angstrom-scale silts. *Science* **2017,** *358*, 511.
14.Fumagalli, L.; Esfandiar, A.; Fabregas, R.; Hu, S.; Ares, P.; Janardanan, A.; Yang, Q.; Radha, B.; Taniguchi, T.; Watanabe, K.; Gomila, G.; Novoselov, K. S.; Geim, A. K., Anomalously low dielectric constant of confined water. *Science* **2018,** *360*, 1339.
15. Secchi, E.; Niguès, A.; Jubin, L.; Siria, A.; Bocquet, L., Scaling behavior for ionic transport and its fluctuations in individual carbon nanotubes. *Phys. Rev. Lett.* **2016,** *116*, 154501.
16. Smeets, R. M.; Keyser, U. F.; Krapf, D.; Wu, M.-Y.; Dekker, N. H.; Dekker, C., Salt dependence of ion transport and DNA translocation through solid-state nanopores. *Nano Lett.* **2006,** *6*, 89.
17. Amiri, H.; Shepard, K. L.; Nuckolls, C.; Hernández Sánchez, R., Single-Walled Carbon Nanotubes: Mimics of Biological Ion Channels. *Nano Lett.* **2017,** *17*, 1204.
18. Corry, B., Water and ion transport through functionalised carbon nanotubes: implications for desalination technology. *Energy Environ. Sci.* **2011,** *4*, 751.
19. Majumder, M.; Chopra, N.; Andrews, R.; Hinds, B. J., Nanoscale hydrodynamics: Enhanced flow in carbon nanotubes. *Nature* **2005,** *438*, 44.
20. Wu, J.; Gerstandt, K.; Zhang, H.; Liu, J.; Hinds, B. J., Electrophoretically induced aqueous flow through single-walled carbon nanotube membranes. *Nat. Nanotechnol.* **2012,** *7*, 133.
21. Geng, J.; Kim, K.; Zhang, J.; Escalada, A.; Tunuguntla, R.; Comolli, L. R.; Allen, F. I.; Shnyrova, A. V.; Cho, K. R.; Munoz, D.; Wang, Y. M.; Grigoropoulos, C. P.; Ajo-Franklin, C. M.; Frolov, V. A.; Noy, A., Stochastic transport through carbon nanotubes in lipid bilayers and live cell membranes. *Nature* **2014,** *514*, 612.
22. Tunuguntla, R. H.; Escalada, A.; V, A. F.; Noy, A., Synthesis, lipid membrane incorporation, and ion permeability testing of carbon nanotube porins. *Nat. Protoc.* **2016,** *11*, 2029.
23. Biesheuvel, P. M.; Bazant, M. Z., Analysis of ionic conductance of carbon nanotubes. *Phys. Rev. E* **2016,** *94*, 050601.
24. Feng, J.; Liu, K.; Graf, M.; Dumcenco, D.; Kis, A.; Di Ventra, M.; Radenovic, A., Observation of ionic Coulomb blockade in nanopores. *Nat. Mater.* **2016,** *15*, 850.
25. Kowalczyk, S. W.; Grosberg, A. Y.; Rabin, Y.; Dekker, C., Modeling the conductance and DNA blockade of solid-state nanopores. *Nanotechnology* **2011,** *22*, 315101.
26. Fornasiero, F.; In, J. B.; Kim, S.; Park, H. G.; Wang, Y.; Grigoropoulos, C. P.; Noy, A.; Bakajin, O., pH-Tunable Ion Selectivity in Carbon Nanotube Pores. *Langmuir* **2010,** *26*, 14848.
27. Tunuguntla, R. H.; Henley, R. Y.; Yao, Y. C.; Pham, T. A.; Wanunu, M.; Noy, A., Enhanced water permeability and tunable ion selectivity in subnanometer carbon nanotube porins. *Science* **2017,** *357*, 792.

28. Lee, C. Y.; Choi, W.; Han, J. H.; Strano, M. S., Coherence resonance in a single-walled carbon nanotube ion channel. *Science* **2010,** *329*, 1320.
29. Grosjean, B.; Pean, C.; Siria, A.; Bocquet, L.; Vuilleumier, R.; Bocquet, M.-L., Chemisorption of hydroxide on 2d materials from DFT calculations: Graphene versus hexagonal boron nitride. *J. Phys. Chem. Lett.* **2016,** *7*, 4695.
30. Uematsu, Y.; Netz, R. R.; Bocquet, L. r.; Bonthuis, D. J., Crossover of the Power-Law Exponent for Carbon Nanotube Conductivity as a Function of Salinity. *J. Phys. Chem. B* **2018,** *122*, 2992.
31. Lokesh, M.; Youn, S. K.; Park, H. G., Osmotic Transport across Surface Functionalized Carbon Nanotube Membrane. *Nano Lett.* **2018,** *18*, 6679.
32. Manghi, M.; Palmeri, J.; Yazda, K.; Henn, F.; Jourdain, V., Role of charge regulation and flow slip in the ionic conductance of nanopores: An analytical approach. *Phys. Rev. E* **2018,** *98*, 012605.
33. Hodgkin Al Fau - Katz, B.; Katz, B., The effect of sodium ions on the electrical activity of giant axon of the squid.
34. Feher, J., 3.1 - The Origin of the Resting Membrane Potential. In *Quantitative Human Physiology (Second Edition)*, Feher, J., Ed. Academic Press: Boston, 2017; pp 255.
35. Wu, J.; Gerstandt, K.; Majumder, M.; Zhan, X.; Hinds, B. J., Highly efficient electroosmotic flow through functionalized carbon nanotube membranes. *Nanoscale* **2011,** *3*, 3321.
36. Yao, S.; Myers, A. M.; Posner, J. D.; Rose, K. A.; Santiago, J. G., Electroosmotic pumps fabricated from porous silicon membranes. *J. Microelectromech. Syst.* **2006,** *15*, 717.
37. Neumcke, B., 1/f noise in membranes. *Biophys. Struct. Mech.* **1978,** *4*, 179.
38. Verveen, A. A.; DeFelice, L. J., Membrane noise. *Prog. Biophys. Mol. Biol.* **1974,** *28*, 189.
39. Antonov, V. F., *Lipids and ionic permeability of membranes*. Nauka: Moscow, 1982; p 150.
40. Bezrukov, S. M.; Irkhin, A. I.; Sibilev, A. I., An Upper Estimate for 1/F Noise Intensity in Ionic Conductors from Experiments with a Molecular Microcontact. *Phys. Lett. A* **1987,** *123*, 477.
41. Hooge, F. N.; Hoppenbrouwers, A. M., 1/F-Noise in Continuous Thin Gold Films. *Physica* **1969,** *45*, 386.
42. Smeets, R. M.; Keyser, U. F.; Dekker, N. H.; Dekker, C., Noise in solid-state nanopores. *Proc. Natl. Acad. Sci. U. S. A.* **2008,** *105*, 417.

Chapter 4. Gateable CNTP Devices: A Model Study

*This chapter has been submitted as a research article: Yao, Y.-C.; Li, Z.; Gillen, A.; Yosinski, S.; Reed, M.; Noy, A. Electrostatic Gating of Ion Transport in Carbon Nanotube Porins: A Modeling Study. *J. Chem. Phys.* **2021**

Carbon nanotube porins (CNTPs) are biomimetic membrane channels that demonstrate excellent biocompatibility and unique water and ion transport properties. Gating transport in CNTPs with external voltage could increase control over ion flow and selectivity. Herein, we used continuum modeling to probe the parameters that enable and further affect CNTP gating efficiency, including the size and composition of the supporting lipid membrane, slip flow in the carbon nanotube, and its intrinsic electronic properties. Our results show that the optimal gated CNTP device consists of a semiconducting CNTP inserted into a small membrane patch containing an internally conductive layer. Moreover, we demonstrate that the ionic transport modulated by gate voltages is controlled by the CNTP charge distribution along the tube under the external gate electric potential. The theoretical understanding developed in this study offers a valuable guide for the future design of gated CNTP devices for nanofluidic studies and the design of novel biomimetic membranes and cellular interfaces.

4.1 Introduction

Efficient and controlled ion flow through nanoscale pores is critical for a variety of applications ranging from water desalination[1] to industrial separations[2, 3] and energy harvesting[4] to kidney dialysis.[5] An emerging body of nanofluidics research demonstrates that strong molecular level confinement in graphene nanoslits,[6, 7] carbon nanotubes,[8, 9, 10, 11, 12] 2D material nanopores,[13] and biological channels, such as aquaporins,[14] produces some of the highest known transport efficiencies.[15] Strong confinement in these nanostructures also induces a range of exotic behaviors including changes in water dielectric constant,[6] water phase transition temperatures,[16] and ionic conductance trends.[7, 10, 17, 18, 19, 20] While nanofluidics researchers have been making significant progress in understanding and harnessing these phenomena,[15, 21] molecular confinement can offer

other, and to date largely unexplored, opportunities to control and regulate transport in nanopores using applied external stimuli, such as electric fields or mechanical forces.[22, 23]

Membrane protein channels, such as aquaporins or Na^+ and K^+ channels in neurons,[24, 25] have elegant functionality that controls fluidic transport. Gated protein channels can switch between open and closed states to modulate ionic and molecular transport through the channel using membrane potential, ligand binding, mechanical force, temperature, or even light as their gating mechanism.[25] In voltage-gated ion channels in neurons, changes in the membrane potential modulate transmembrane ion current, enabling fast and reliable transmission of nerve signals over large distances.[25] Replicating such capabilities using synthetic analogs, such as single-digit nanopores[26] and other model nanofluidic systems,[27, 28, 29] has the potential to revolutionize biointerface technologies by enabling 'smart' membranes with increased efficiency and stability.

A number of microfluidic transistors and lab-on-chip devices have shown on/off behavior that is controlled by an externally applied gate voltage.[30, 31, 32] However, these devices have relatively large channel sizes and rely on ion-selective media to control the flow of ions and charged molecules,[33] which severely limits their application. Single-digit nanopores offer an opportunity to combine confinement and gating functionality to gain ultimate control over transport, perhaps down to a single ion level.

Previous work by our group has led to the development of carbon nanotube porins (CNTPs).[9, 34, 35] CNTPs are biomimetic channels made of single-walled carbon nanotubes, which have well-defined diameters at the nanometer and sub-nanometer range. Furthermore, CNTPs can be coated with lipid molecules that disperse the CNTPs and enable their easy self-insertion into lipid membranes.[34, 35] Our previous studies showed efficient electrophoretic and electroosmotic transport in individual small diameter CNTPs incorporated into a modified planar lipid bilayer device, where lipid bilayers span over a *ca.* 100 nm diameter SiN_x aperture.[9, 20] This experimental configuration provides several advantages for exploring electrostatic gating of nanofluidic transport. Small diameter CNTPs provide strong confinement that is essential for efficient gating at higher ionic strength solutions. Moreover, carbon nanotubes with

different pore sizes and electronic properties can be incorporated into the lipid bilayer, while the microfabricated SiN_x device platform allows reasonably simple incorporation of electrodes and straightforward ion current measurements increasing the versatility of the system.

Here we use continuum COMSOL modeling to explore the possibilities of creating gated CNTP devices and the basic parameters that govern their function. We demonstrate that we should be able to achieve efficient gating of CNTP channels and examine the impact of lipid size and composition to identify threshold requirements for gating. Using the optimal lipid configuration, we further probe the dependence of device gating on the intrinsic properties of the CNTPs, including slip length and permittivity. We believe that these results can be used to guide experimental approaches for creating gated CNTP devices and also inform the broader design space for the next generation of nanofluidic systems.

4.2 Simulation Setup

To explore the possibility of constructing a gated CNTP device we started with the experimental setup that we developed for measuring ion conductance of individual CNTPs[9, 20] (Fig. 4.1A) and modeled it in the finite element analysis software COMSOL Multiphysics 5.5.[29] Our simulations used three physics modules for describing the processes in this system: electrostatic, transport of diluted species, and creeping flow, which are described by the Poisson equation, Nernst-Planck equation, and Stokes equation, respectively.[29, 36] We modeled the device as an axisymmetric cell (see Fig 1B and C for a cross-section and a three-dimensional (3D) model) that has two reservoirs with 50 nm height and radius (r). These chambers were separated by a circular patch of a lipid membrane with a CNTP channel placed in the center. The parameters of the CNTP channel were matched to values obtained from previous experiments:[34] a length of 10 nm, radius of 0.58 nm, and CNT wall thickness of 0.34 nm, giving 1.5 nm as the carbon-to-carbon diameter of the CNTP.[8, 20, 34] The CNTP channel was also assigned an entrance charge density ($4e^-$), equivalent to four negatively charged functional groups at one end, that was distributed homogenously along the CNTP pore mouth. This value was chosen

based on our best estimate of the number of COOH groups at the nanotube pore mouth.[20] The membrane matrix holding the CNTP was modeled as a 10 nm thick simplified lipid bilayer that was impermeable to liquid solutions. This lipid bilayer was divided into three parts: two hydrophilic outer layers and an inner hydrophobic layer. Both reservoirs were filled with 100 mM KCl solution (unless otherwise specified).

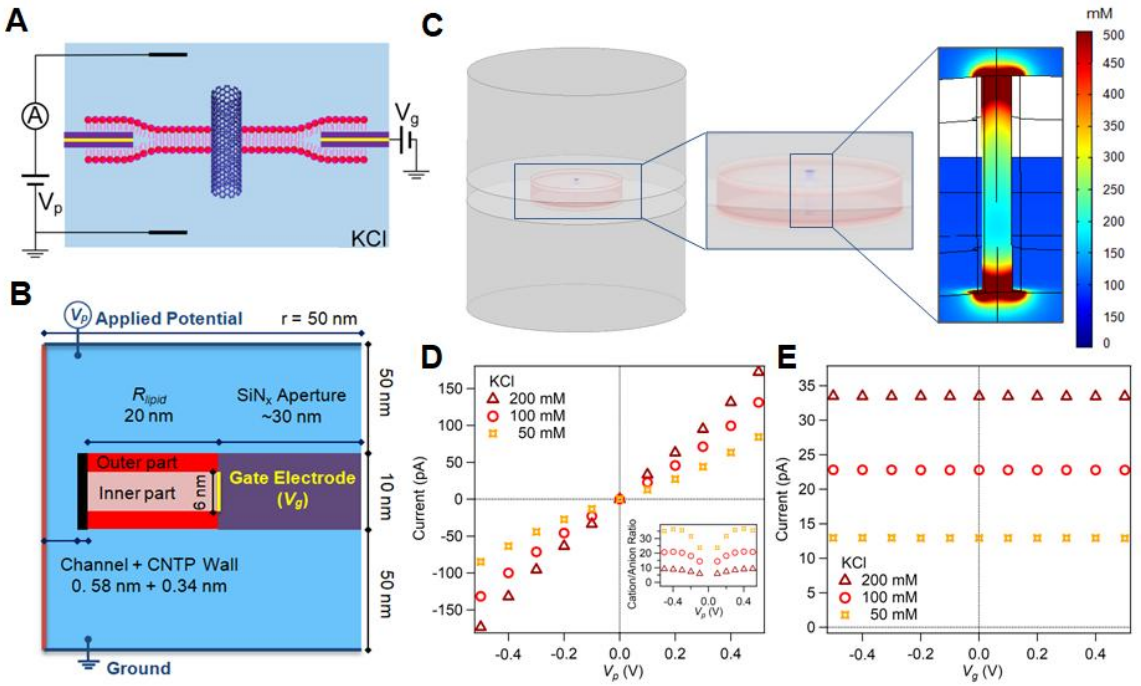

Figure 4.1. Gated CNTP device setup and initial conductance characteristics. (**A**) Schematics of the device setup. (**B**) The axisymmetric cross-section of the CNTP model. The applied potential (V_p) at the upper boundary of top reservoir drives the ionic current through the nanotube pore and the gate voltage (V_g) at the boundary between lipid inner part and the SiNx aperture provides the applied gate voltage potential. (**C**) The 3D structure of the axisymmetric setup with zoomed-in view at the lipid patch and gate electrode rim. Inset: K^+ ion distribution along the CNTP channel at V_p = 0.1 V. (**D**) I-V_p curves for CNTP at 50, 100, and 200 mM KCl. Inset: Ionic current ratio of K^+ and Cl^- ions. (**E**) Ionic current of CNTP channel as a function of gate voltage in KCl solutions of different concentrations at V_p = 0.1 V.

The bottom reservoir was grounded (0 V) and an external potential (V_p) was applied at the upper boundary of the top reservoir to drive the ion transport through the CNTP.

To simulate the electrostatic gating of the device we have also incorporated a gating electrode into the device aperture rim,[37] with a gate voltage (V_g) applied at the boundary of the hydrophobic part of the lipid and the SiN_x aperture. The applied voltages varied across a bio-compatible range of -0.5 V and 0.5 V. Prior experiments showed that lipid bilayers spanning over the nanopores remained stable at these voltages.[38, 39] Ionic current was determined by integrating the current density of ions passing through a channel cross-section halfway along the CNTP. Currents at positions 1/3 and 2/3 along the CNTP were also checked to confirm the accuracy of the finite element modeling. In order to compare the gating efficiency of our system, we also calculated the gating factor as:

$$Gating\ Factor = I_{max}/I_{min}$$

where I_{max} and I_{min} were, respectively, the highest and lowest currents obtained at constant V_p and different applied gate voltages, V_g.

4.3 Device Geometry, Lipid Configuration, and Gating Efficiency

We first investigated the ionic conductance and selectivity of the CNTP channel in the absence of an applied gate voltage (V_g = 0 V). In agreement with previous data from the literature,[17, 20, 28] we assigned a small negative charge to the inner surface of CNTP and set the slip length to 1 nm at 100 mM KCl. As expected, the ion concentration distribution showed cation accumulation next to the negatively charged nanotube entrances (Fig. 4.1C, inset). A comparison of the cation and anion concentrations inside the channel indicated the channel was cation selective and the current-voltage (I-V_p) curves were linear within the +/- 0.5 V applied potential range (Fig. 4.1D), both in line with experimental observaions.[20] The conductance, 228 pS, and cation/anion ratio, *ca.* 14, also showed excellent agreement with previous experimental data obtained under similar conditions (214 ± 40 pS and *ca.* 12 at a KCl concentration of 100 mM),[20] indicating that our COMSOL model can effectively capture the major features of ion transport in 1.5 nm diameter CNTPs. Upon application of a gate voltage, however, this device configuration showed no gating effect as the current remained virtually constant with varying V_g (Fig. 4.1E). This behavior was not surprising because the lipid molecules are not very

polarizable and thus acted as an insulator between the CNTP channel and the gate electrode, hindering electric field propagation.

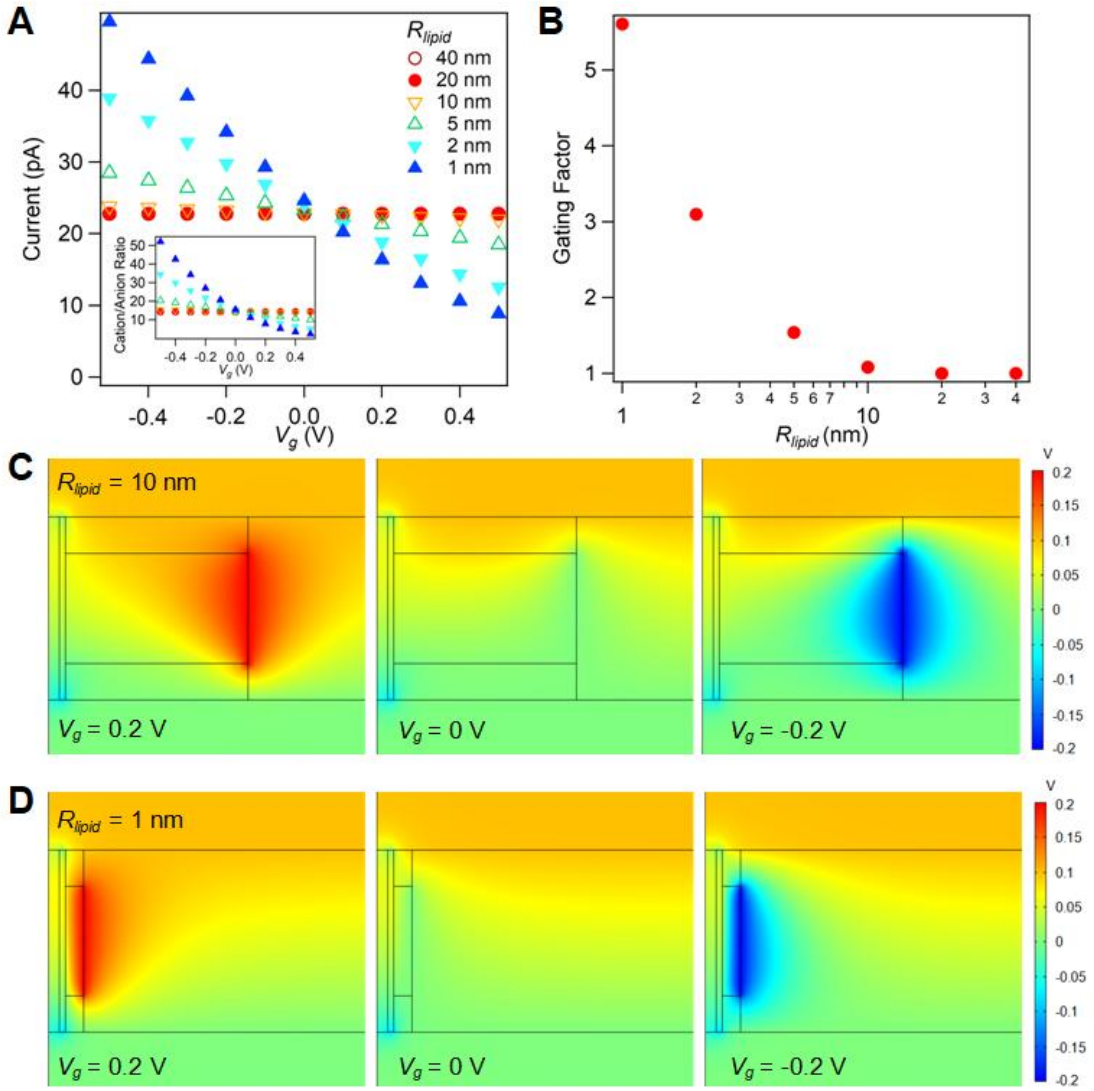

Figure 4.2. Lipid bilayer patch size and CNTP gating. (**A**) Ion current through the CNTP channel as a function of V_g at V_p = 0.1 V for R_{lipid} = 1, 2, 5, 10, 20, and 40 nm. Inset: Calculated cation/anion selectivity ratio. (**B**) Plot of the gating factor for different lipid patch sizes, R_{lipid}. (**C, D**) Electric potential distributions at V_p = 0.1 V for R_{lipid} = 10 nm (C) and 1 nm (D) calculated for V_g = 0.2 V (left), 0 V (center), and -0.2 V (right).

One way to improve the gating efficiency would be to reduce the size of the bilayer patch, thus bringing the electrode closer to the CNTP channel. To test this hypothesis, we

simulated transport in the devices with different SiN_x aperture sizes, which was accomplished by changing the lipid bilayer radius (R_{lipid}) in the model. In line with expectation, as we varied V_g, the ionic current remained unchanged for large bilayer sizes (R_{lipid} = 40, 20, and 10 nm). However, as the R_{lipid} value dropped below 10 nm (R_{lipid} = 5, 2, and 1 nm), we observed a gating behavior with enhanced ionic current at negative V_g and decreased current at positive V_g (Fig. 4.2A, B). Furthermore, we noticed that the higher currents at negative V_g were due to an increased cation flow, suggesting that gating also directly impacted the cation/anion selectivity of the device (Fig. 4.2A, inset). As a negative gate voltage made the channel surface potential more negative, it attracted more cations, which increased the overall ionic current in this cation selective channel. Positive gate voltages reduced the negative surface potential, lowering the cation current that dominated the conductance in this device. Despite the strength of the electric field at the CNTP increasing as R_{lipid} decreases (Fig. 4.2C and 4.2D), our simulations never showed gating factors higher than 10, indicating that reducing the lipid bilayer patch size alone was a poor way to obtain efficient gating.

Another, and potentially more important, parameter influencing gating in a CNTP device is the composition of the lipid membrane and its dielectric properties. We modeled these effects using different relative permittivity values for the inner and outer lipid bilayer regions. For these simulations we kept the bilayer size, R_{lipid}, constant at 20 nm. In the original condition, the relative permittivity of the outer regions, corresponding to the hydrophilic lipid head groups, was set to 3, while the permittivity of hydrophobic inner part was set to 1.[40] We examined various lipid membrane compositions by using different combinations of relative permittivity values for the inner and outer lipid regions, which we denote as *lipid(outer, inner, outer)* (Fig. 4.3A and 4.4). When the dielectric permittivity of the outer regions was kept constant, higher inner permittivity values resulted in higher gating factors (Fig. 4.3B - E). A comparison of Fig. 4.3C, D and E shows that as the inner permittivity increases, the electric field starts to propagate much closer to the CNTP.

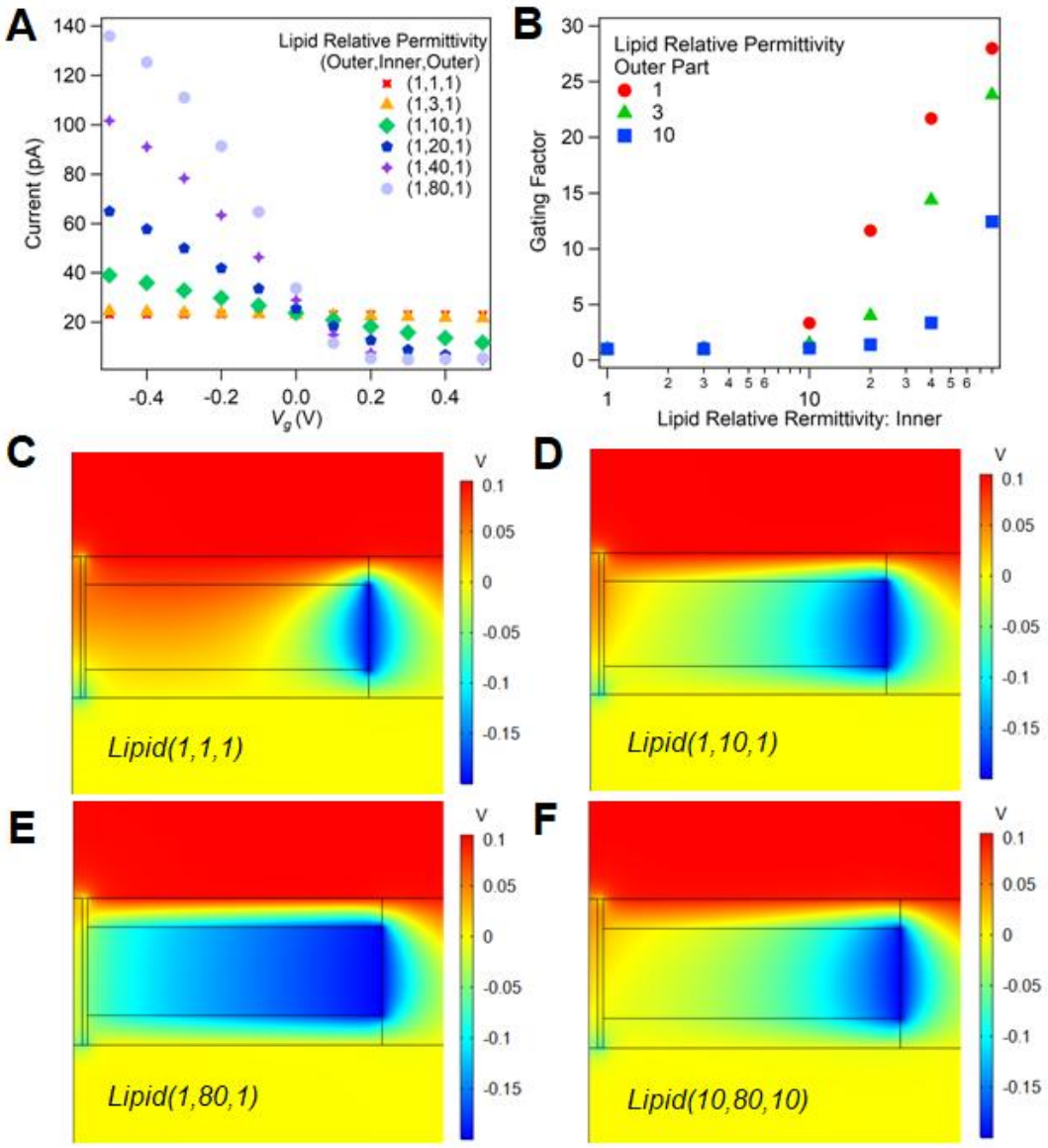

Figure 4.3. Lipid membrane dielectric properties and CNTP gating. (**A**) Calculated ionic current as a function of applied gate voltage, V_g, at V_p = 0.1 V. The outer lipid layer relative permittivity was set to be 1 and inner lipid relative permittivity values varied from 1 to 80 as indicated on the legend. (**B**) Calculated gating factors as a function of relative permittivity of both lipid outer and inner parts. (**C-F**) Surface electric potential distribution at V_p = 0.1 V and V_g = -0.2 V calculated for four lipid matrix compositions: *lipid(1,1,1)* (**C**), *lipid(1,10,1)* (**D**), *lipid(1,80,1)* (**E**), and *lipid(10,80,10)* (**F**).

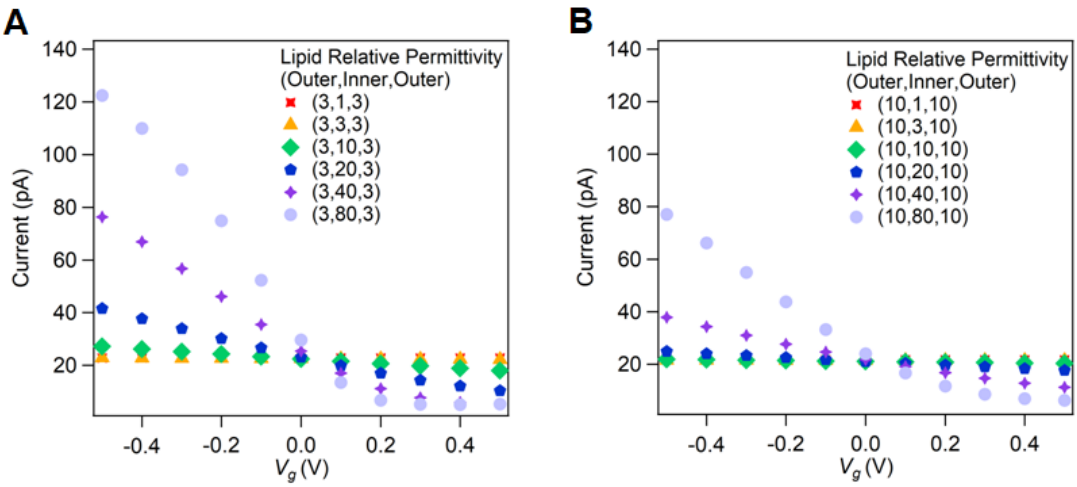

Figure 4.4. Calculated CNTP ionic current as a function of V_g. For these simulations V_p value was set at 0.1 V, and outer lipid relative permittivity value was set at 3 (**A**) and 10 (**B**). Inner lipid relative permittivity values varied from 1 to 80 as indicated on the legend.

We obtained the highest gating factor values for the configurations where the inner region permittivity was high, and the outer region permittivity was low. This observation is not surprising, as in order to prevent field dissipation into the solution reservoirs and maintain high gating efficiency an ideal bilayer matrix must have outer lipid regions with low relative permittivity values (Fig. 4.3B). This effect is clearly observable by comparing the field distribution for *lipid(10,80,10)* (Fig. 3F) to *lipid(1,80,1)* (Fig. 4.3E), where the electric field in the former is much weaker and much closer to what was observed for the *lipid(1,10,1)* configuration. We have also investigated whether the change in the gating efficiency is driven by the absolute values of the bilayer matrix permittivity or the ratio of the permittivity values of the inner and outer region. We observed strong correlation between the calculated gating factor values and the absolute values of the permittivity of the inner bilayer region (Fig. 4.5A). In contrast, the correlation with the ratio of the inner and outer region permittivity values was much weaker (Fig. 4.5B), indicating that absolute value of the permittivity of the inner region remains the dominant factor that determined gating efficiency. Overall, the gating factors improve from *ca.* 5x observed for *lipid(1,10,1)* to *ca.* 30x for *lipid(1,80,1)*. Although these gating factors are much lower than that the typical on/off ratios for solid-state

transistors (10^7-10^9x), they are comparable to the gating factor values achievable using ionic field effect transistors, such as microfluidic transistors (5-100x).[41, 42]

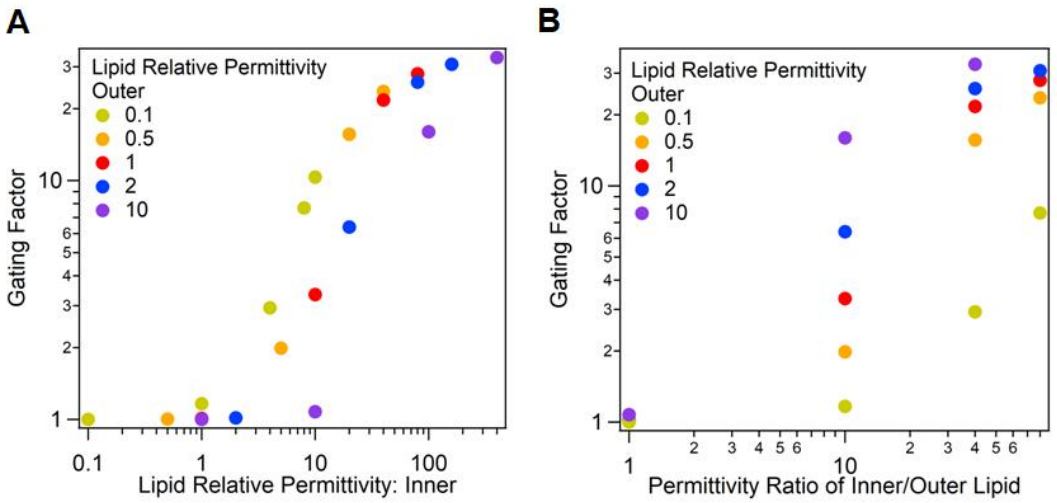

Figure 4.5. Calculated gating factors depending on lipid configurations. Gating factors plotted as a function of absolute inner lipid relative permittivity (**A**) and as a function of the ratio of lipid outer and inner relative permittivity (**B**) at V_p = 0.1 V.

Based on these results, we conclude that to maximize gating efficiency in a CNTP devices we need to use small bilayer patches with highly conductive inner regions and insulating outer regions. As fabricating SiN_x aperture devices with radii smaller than 20 nm is quite difficult, control of the bilayer composition represents a more attractive experimental opportunity. A properly engineered lipid bilayer matrix also produces higher gating efficiencies even for a relatively large membrane size (R_{lipid} = 20 nm). What are the possible approaches to engineer such bilayer structures? Most lipid molecules have relative permittivity values around 1 to 3.[40] Lipid doping could produce more conductive lipid bilayers and researchers have shown that organic semiconducting materials can be doped into lipid bilayer membranes, resulting in higher relative permittivity values.[37, 43, 44] Alternatively, lipids may be substituted with conductive polymer chains, which again can increase the relative permittivity within the matrix layer.[45]

4.4 Carbon Nanotube Porin Properties and Gating Efficiency

Another important question is whether intrinsic properties of the CNTPs, such as their electronic nature and slip length, impact the gating characteristics of the final device.[27, 46] Slip length is an important parameter impacting both the electroosmotic flow and ion transport through the CNTP. Intuitively, lower intrinsic friction for the transport should lead to more sensitivity to external gating. In our initial set of simulations we set the slip length to 1 nm to match the value derived from the experimental conductance measurements for d = 1.5 nm CNTPs.[20] However, several studies have suggested that the slip length may be much larger depending on factors such as CNT chirality or the presence of additional chemical moieties.[10] To study the effect of different CNTP slip lengths on gating, we compared the gating factor values obtained in our simulations for two lipid systems, *lipid(1,80,1)* (Fig. 4.6A) and *lipid(1,10,1)*, with slip lengths ranging from 0 (non-slip) to 1000 nm. For both lipid systems, we obtained gating at all slip lengths, with a higher slip length producing a higher gating factor. However, this enhancement was very minimal, less than 10% (Fig. 4.6B), indicating that CNTP slip length does not significantly impact the CNTP gating efficiency.

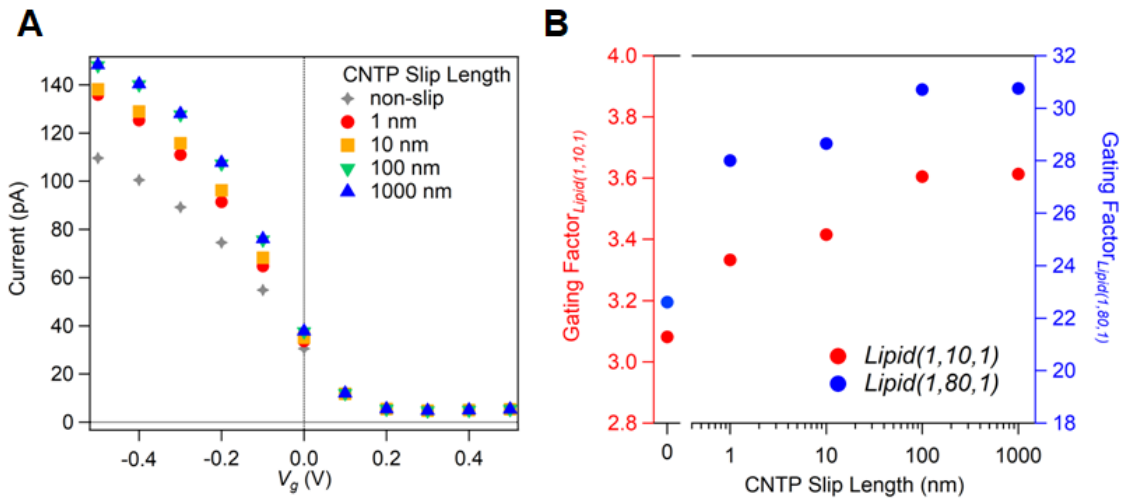

Figure 4.6. CNT slip length and CNTP gating. (**A**) Ionic current as a function of V_g for various CNTP slip length 0, 1, 10, 100, 1000 nm with *lipid(1,80,1)*. (**B**) The gating factor for different CNTP slip length with two lipid permittivity conditions: *lipid(1,80,1)* (blue, right axis) and *lipid(1,10,1)* (red, left axis). All simulations assumed R_{lipid} = 20 nm and V_p = 0.1 V.

CNTs can be semiconducting, semi-metallic, or metallic in nature depending on the nanotube structure (chirality).[47] Difficulties associated with obtaining chirally pure samples mean that, to date, many experimental studies use CNTs that are a mix of both metallic and semiconducting nanotubes and, as a result, permittivity values are unknown. However, as chirality sorting techniques continue to improve, an increase in the availability of pure semiconducting and metallic samples means that devices can be constructed using nanotubes with more well-defined electronic properties.[48, 49, 50, 51] We modeled CNTPs with different electronic structures by assigning different relative permittivity values to the CNTP walls (Fig. 4.7) and then calculated the impact this had on the ion transport. Relative permittivity values of 30-100 corresponded to semiconducting nanotubes, while values above 1000 represented pure metallic nanotubes.[52] In the absence of an applied gate voltage (V_g = 0 V), metallic nanotubes had higher ionic currents than their semiconducting counterparts, in agreement with previous experimental observations.[27, 46] We attributed this phenomenon to the more effective delocalization of the negative entrance charge along the metallic CNTP (Fig. 4.7D), which led to higher accumulation of cations inside the channel (Fig. 4.9) and thus to higher overall conductance.

The other notable observation was that the gating efficiency did not monotonically increase over different CNTP relative permittivity values (Fig. 4.7B). The highest gating factor values appeared at a CNTP permittivity value around 100. After examining the underlying values impacting the gating factor, I_{max} and I_{min}, it became clear to us that the distribution of the gating factor values was strongly impacted by the variations in I_{min} (Fig. 4.8). While I_{max} continuously increased with increasing permittivity values, the I_{min} values showed a distinct minimum at the permittivity value range corresponding to semiconducting nanotubes.

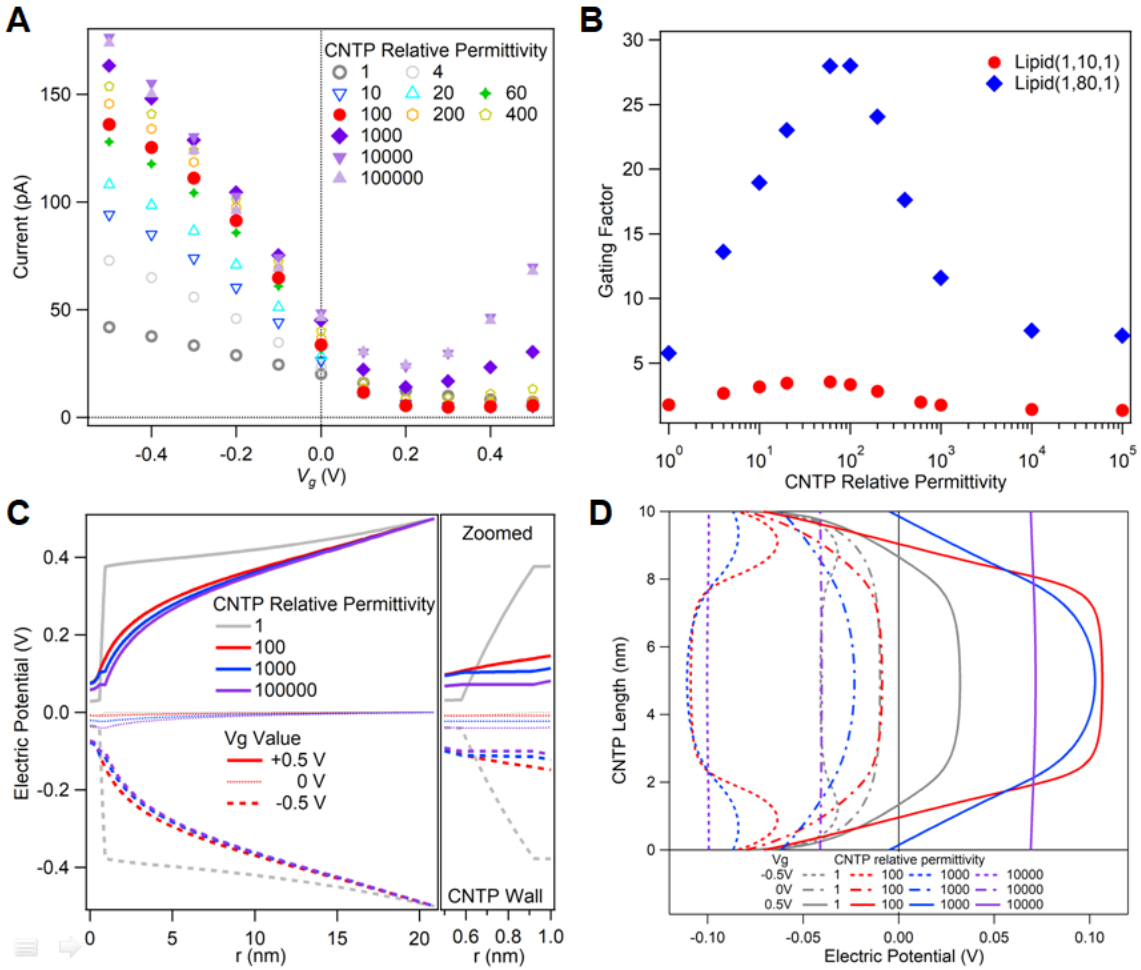

Figure 4.7. Electronic properties of CNTPs and CNTP gating. (**A**) Ionic current as a function of V_g for different CNTP relative permittivity values with *lipid(1,80,1)* at V_p = 0.1 V. (**B**) Gating factors as a function of CNTP relative permittivity values for two lipid compositions *lipid(1,80,1)* and *lipid(1,10,1)*. (**C**) Electrical potential profiles showing propagation of the gate electrode potential (r = 20.92 nm indicates electrode location and r = 0 nm corresponds to the center of the channel) for different CNTP relative permittivity values. membrane composition was fixed at *lipid(1,80,1)*, V_p = 0 V and gate voltage values varied as V_g = 0.5, 0, -0.5 V. Zoomed-in area: Comparison of the electric potential profiles within the CNTP wall region (r = 0.58 to 0.92 nm). (**D**). Profiles of the electric potential distribution along the CNTP wall (r = 0.58 nm) from the bottom (length = 0 nm) to the top of the CNTP (length = 10 nm) for different CNTP relative permittivity values. Membrane composition was fixed at *lipid(1,80,1)*, V_p = 0 V and gate voltage values varied as V_g = 0.5, 0, -0.5 V. All simulations assumed R_{lipid} = 20 nm.

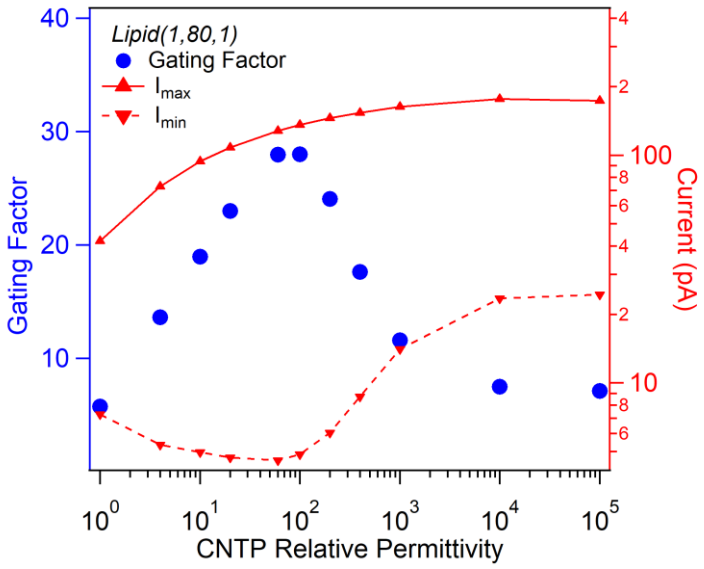

Figure 4.8. Calculated gating factor values (left axis) and maximum and minimum ion current values (right axis) plotted as a function of CNTP relative permittivity.

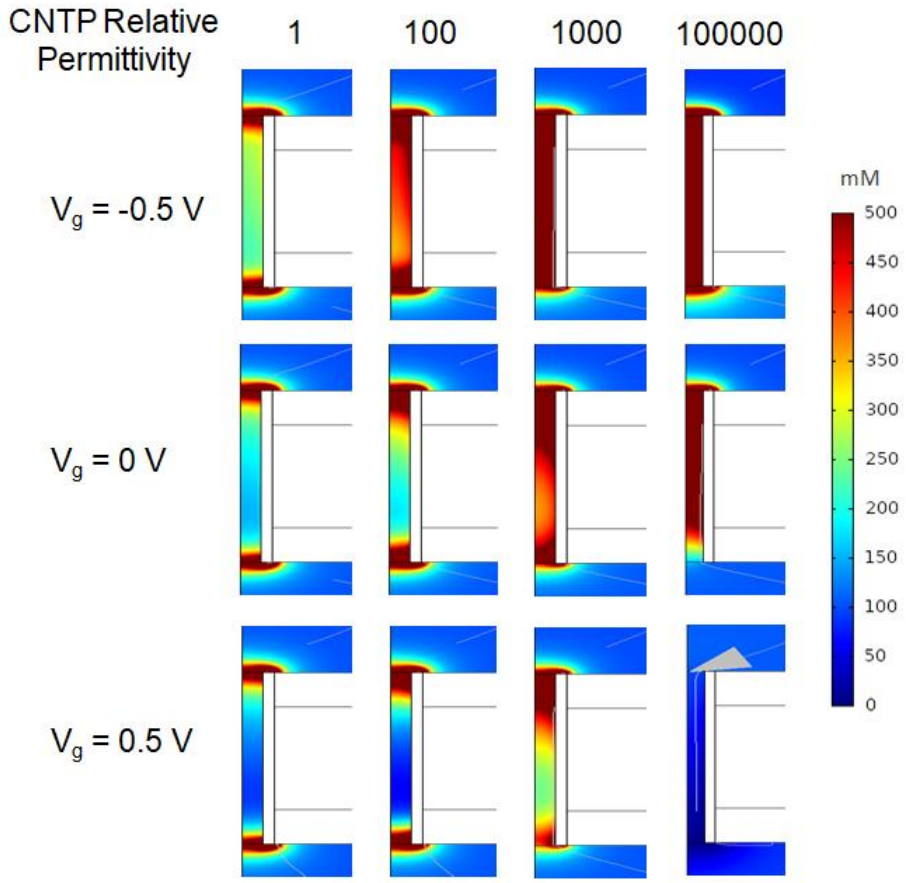

Figure 4.9. Cation distributions calculated for *lipid(1,80,1)* at V_p = 0.1 V for different CNTP relative permittivity values: 1, 100, 1000, and 100000 and different V_g values: -0.5, 0, 0.5 V.

Electric potential distributions (Fig. 4.7C, D) provide strong clues as to why these nanotubes were the most effective at shutting down the ion current under positive applied potential. Negative entrance charges remained localized in a semiconducting CNTP even in the presence of external fields (Fig. 4.7D), and thus could provide an effective barrier for anion transport. In addition, semiconducting nanotubes allowed the electric field to propagate into the channel (Fig 4.7D, red lines), creating an effective barrier for cation transport at positive V_g values, as evidenced by the low cation concentration in the middle of the nanotube (Fig. 4.8). As the result, both cation and anion transport was suppressed at positive V_g values and the overall ion current through the channel was minimized. In insulating CNTPs (Fig. 4.7C, D, gray lines) the electric field applied by the gate electrode could not effectively penetrate into the channel, allowing cation flow even at positive gate voltages and producing higher I_{min} current values. Metallic CNTPs, on the contrary, were quite efficient in propagating the gating field into the middle of the channel and effectively shutting down the cation current. However, they were also very effective in delocalizing charge, meaning that an external gate voltage was able to alter the potential over the entire nanotube (Fig 4.7D). As a result, when we applied a sufficiently positive gate voltage to the metallic nanotube in the simulation, we were able to reverse the effective charge, repelling the cations. However, this charge reversal simultaneously reduced the barrier to anion transport, leading to anions becoming the primary charge carrier. Indeed, the increase in total current observed at high positive V_g for permittivity values above 1000 was due to anion flow, confirming this hypothesis (Fig. 4.7A and 4.8). Based on these findings, we conclude that, in order to achieve optimum gating performance, an ideal CNTP-based gate device should incorporate semiconducting CNTs.

4.5 Conclusions

In this work, we used COMSOL simulations to investigate gating of carbon nanotube porins. Our results showed that efficient gating can be achieved in a device with an individual CNTPs embedded within a thin membrane matrix. Our simulations show that the best gating occurs in a device that consists of a semiconducting CNTP (with

permittivity values *ca.* 80-100) inserted into a thin membrane with a highly polarizable or conductive interior, which potentially could be accomplished by doping the lipid bilayer. We further demonstrated that the gate electric field can strongly affect the surface charge distribution of the CNTP channel, and that the extent by which this occurs is dependent on the nanotube's electronic nature. The results from our model demonstrate that electrostatic gating is impacted directly by the ion distribution and cation/anion selectivity. Additional factors, such as changes in ion mobility and hydration/dehydration energy, can play important roles in the gating effect mechanisms for ion transport in confined spaces. However, a COMSOL model does not account for these effects and capturing them would require molecular dynamics simulations. This electrostatic gating mechanism can be used to control the ionic flow and selectivity in the device. Our simulations show that these devices can control ion transport through the CNTP channel using gate voltages that are well within a bio-compatible range of values, indicating that these concepts can be used for real-world bioelectronics applications.

Acknowledgement

Many thanks to Dr. Shari Yosinski, Prof. Mark Reed, Mauricio Dantus, Prof. Viatcheslav Freger, and Pedro de Souza for discussion and comments about this project.

References

1. Werber, J. R.; Osuji, C. O.; Elimelech, M., Materials for next-generation desalination and water purification membranes. *Nat. Rev. Mater.* **2016,** *1*, 16018.
2. Li, Z.; Li, Y.; Yao, Y.-C.; Aydin, F.; Zhan, C.; Chen, Y.; Elimelech, M.; Pham, T. A.; Noy, A., Strong Differential Monovalent Anion Selectivity in Narrow Diameter Carbon Nanotube Porins. *ACS Nano* **2020,** *14*, 6269.
3. Epsztein, R.; DuChanois, R. M.; Ritt, C. L.; Noy, A.; Elimelech, M., Towards single-species selectivity of membranes with subnanometre pores. *Nat. Nanotechnol.* **2020**.
4. Xiao, K.; Jiang, L.; Antonietti, M., Ion Transport in Nanofluidic Devices for Energy Harvesting. *Joule* **2019,** *3*, 2364.
5. Cameron, J. S., *A history of the treatment of renal failure by dialysis*. Oxford University Press Oxford: 2002.
6. Fumagalli, L.; Esfandiar, A.; Fabregas, R.; Hu, S.; Ares, P.; Janardanan, A.; Yang, Q.; Radha, B.; Taniguchi, T.; Watanabe, K.; Gomila, G.; Novoselov, K. S.; Geim, A. K., Anomalously low dielectric constant of confined water. *Science* **2018,** *360*, 1339.

7. Gopinadhan, K.; Hu, S.; Esfandiar, A.; Lozada-Hidalgo, M.; Wang, F. C.; Yang, Q.; Tyurnina, A. V.; Keerthi, A.; Radha, B.; Geim, A. K., Complete steric exclusion of ions and proton transport through confined monolayer water. *Science* **2019,** *363*, 145.
8. Joseph, S.; Aluru, N. R., Why are carbon nanotubes fast transporters of water? *Nano Lett.* **2008,** *8*, 452.
9. Tunuguntla, R. H.; Henley, R. Y.; Yao, Y. C.; Pham, T. A.; Wanunu, M.; Noy, A., Enhanced water permeability and tunable ion selectivity in subnanometer carbon nanotube porins. *Science* **2017,** *357*, 792.
10. Secchi, E.; Marbach, S.; Nigues, A.; Stein, D.; Siria, A.; Bocquet, L., Massive radius-dependent flow slippage in carbon nanotubes. *Nature* **2016,** *537*, 210.
11. Hummer, G.; Rasaiah, J. C.; Noworyta, J. P., Water conduction through the hydrophobic channel of a carbon nanotube. *Nature* **2001,** *414*, 188.
12. Li, Y.; Li, Z.; Aydin, F.; Quan, J.; Chen, X.; Yao, Y. C.; Zhan, C.; Chen, Y.; Pham, T. A.; Noy, A., Water-ion permselectivity of narrow-diameter carbon nanotubes. *Sci. Adv.* **2020,** *6*.
13. Feng, J.; Graf, M.; Liu, K.; Ovchinnikov, D.; Dumcenco, D.; Heiranian, M.; Nandigana, V.; Aluru, N. R.; Kis, A.; Radenovic, A., Single-layer MoS2 nanopores as nanopower generators. *Nature* **2016**.
14. Horner, A.; Zocher, F.; Preiner, J.; Ollinger, N.; Siligan, C.; Akimov, S. A.; Pohl, P., The mobility of single-file water molecules is governed by the number of H-bonds they may form with channel-lining residues. *Sci. Adv.* **2015,** *1*, e1400083.
15. Bocquet, L., Nanofluidics coming of age. *Nat. Mater.* **2020,** *19*, 254.
16. Agrawal, K. V.; Shimizu, S.; Drahushuk, L. W.; Kilcoyne, D.; Strano, M. S., Observation of extreme phase transition temperatures of water confined inside isolated carbon nanotubes. *Nat. Nanotechnol.* **2017,** *12*, 267.
17. Secchi, E.; Nigues, A.; Jubin, L.; Siria, A.; Bocquet, L., Scaling behavior for ionic transport and its fluctuations in individual carbon nanotubes. *Phys. Rev. Lett.* **2016,** *116*, 154501.
18. Biesheuvel, P. M.; Bazant, M. Z., Analysis of ionic conductance of carbon nanotubes. *Phys. Rev. E* **2016,** *94*, 050601.
19. Noh, Y.; Aluru, N. R., Ion transport in electrically imperfect nanopores. *ACS Nano* **2020,** *14*, 10518.
20. Yao, Y.-C.; Taqieddin, A.; Alibakhshi, M. A.; Wanunu, M.; Aluru, N. R.; Noy, A., Strong electroosmotic coupling dominates ion conductance of 1.5 nm diameter carbon nanotube porins. *ACS Nano* **2019,** *13*, 12851.
21. Kavokine, N.; Netz, R. R.; Bocquet, L., Fluids at the Nanoscale: From Continuum to Subcontinuum Transport. *Annual Review of Fluid Mechanics* **2021,** *53*, null.
22. Fang, A.; Kroenlein, K.; Riccardi, D.; Smolyanitsky, A., Highly mechanosensitive ion channels from graphene-embedded crown ethers. *Nature Materials* **2019,** *18*, 76.
23. Marcotte, A.; Mouterde, T.; Niguès, A.; Siria, A.; Bocquet, L., Mechanically activated ionic transport across single-digit carbon nanotubes. *Nature Materials* **2020,** *19*, 1057.
24. Tornroth-Horsefield, S.; Wang, Y.; Hedfalk, K.; Johanson, U.; Karlsson, M.; Tajkhorshid, E.; Neutze, R.; Kjellbom, P., Structural mechanism of plant aquaporin gating. *Nature* **2006,** *439*, 688.

25. Cannon, S. C., Ion Channels, Overview. In *Encyclopedia of the Neurological Sciences (Second Edition)*, Aminoff, M. J.; Daroff, R. B., Eds. Academic Press: Oxford, 2014; pp 747.
26. Faucher, S.; Aluru, N.; Bazant, M. Z.; Blankschtein, D.; Brozena, A. H.; Cumings, J.; Pedro de Souza, J.; Elimelech, M.; Epsztein, R.; Fourkas, J. T., Critical knowledge gaps in mass transport through single-digit nanopores: a review and perspective. *J. Phys. Chem. C* **2019,** *123*, 21309.
27. Pang, P.; He, J.; Park, J. H.; Krstic, P. S.; Lindsay, S., Origin of giant ionic currents in carbon nanotube channels. *ACS Nano* **2011,** *5*, 7277.
28. Marcotte, A.; Mouterde, T.; Nigues, A.; Siria, A.; Bocquet, L., Mechanically activated ionic transport across single-digit carbon nanotubes. *Nat. Mater.* **2020,** *19*, 1057.
29. Lucas, R. A.; Siwy, Z. S., Tunable nanopore arrays as the basis for ionic circuits. *ACS Appl. Mater. Interfaces* **2020,** *12*, 56622.
30. Karnik, R.; Fan, R.; Yue, M.; Li, D.; Yang, P.; Majumdar, A., Electrostatic control of ions and molecules in nanofluidic transistors. *Nano Lett.* **2005,** *5*, 943.
31. Karnik, R.; Castelino, K.; Majumdar, A., Field-effect control of protein transport in a nanofluidic transistor circuit. *Appl. Phys. Lett.* **2006,** *88*, 123114.
32. Guan, W.; Fan, R.; Reed, M. A., Field-effect reconfigurable nanofluidic ionic diodes. *Nat. Commun.* **2011,** *2*, 506.
33. Sun, G.; Senapati, S.; Chang, H. C., High-flux ionic diodes, ionic transistors and ionic amplifiers based on external ion concentration polarization by an ion exchange membrane: a new scalable ionic circuit platform. *Lab Chip* **2016,** *16*, 1171.
34. Geng, J.; Kim, K.; Zhang, J.; Escalada, A.; Tunuguntla, R.; Comolli, L. R.; Allen, F. I.; Shnyrova, A. V.; Cho, K. R.; Munoz, D.; Wang, Y. M.; Grigoropoulos, C. P.; Ajo-Franklin, C. M.; Frolov, V. A.; Noy, A., Stochastic transport through carbon nanotubes in lipid bilayers and live cell membranes. *Nature* **2014,** *514*, 612.
35. Tunuguntla, R. H.; Escalada, A.; V, A. F.; Noy, A., Synthesis, lipid membrane incorporation, and ion permeability testing of carbon nanotube porins. *Nat. Protoc.* **2016,** *11*, 2029.
36. Lin, C.-Y.; Wong, P.-H.; Wang, P.-H.; Siwy, Z. S.; Yeh, L.-H., Electrodiffusioosmosis-induced negative differential resistance in pH-regulated mesopores containing purely monovalent solutions. *ACS Appl. Mater. Interfaces* **2020,** *12*, 3198.
37. Ma, T.; Feng, X.; Ohori, T.; Miyata, R.; Tadaki, D.; Yamaura, D.; Deguchi, T.; Komiya, M.; Kanomata, K.; Hirose, F.; Niwano, M.; Hirano-Iwata, A., Modulation of photoinduced transmembrane currents in a fullerene-doped freestanding lipid bilayer by a lateral bias. *ACS omega* **2019,** *4*, 18299.
38. Kang, X.; Alibakhshi, M. A.; Wanunu, M., One-pot species release and nanopore detection in a voltage-stable lipid bilayer platform. *Nano Lett.* **2019,** *19*, 9145.
39. Gutsmann, T.; Heimburg, T.; Keyser, U.; Mahendran, K. R.; Winterhalter, M., Protein reconstitution into freestanding planar lipid membranes for electrophysiological characterization. *Nat. Protoc.* **2015,** *10*, 188.
40. Huang, W.; Levitt, D. G., Theoretical calculation of the dielectric constant of a bilayer membrane. *Biophys. J.* **1977,** *17*, 111.

41. Sze, S. M.; Ng, K. K., *Physics and properties of semiconductors—A review*. 2006; p 5.
42. Nam, S.-W.; Rooks, M. J.; Kim, K.-B.; Rossnagel, S. M., Ionic field effect transistors with sub-10 nm multiple nanopores. *Nano Lett.* **2009,** *9*, 2044.
43. Schwenn, P. E.; Burn, P. L.; Powell, B. J., Calculation of solid state molecular ionisation energies and electron affinities for organic semiconductors. *Org. Electron.* **2011,** *12*, 394.
44. Sun, H.; Ryno, S.; Zhong, C.; Ravva, M. K.; Sun, Z.; Körzdörfer, T.; Brédas, J.-L., Ionization energies, electron affinities, and polarization energies of organic molecular crystals: quantitative estimations from a polarizable continuum model (PCM)-tuned range-separated density functional approach. *J. Chem. Theory Comput.* **2016,** *12*, 2906.
45. Johansson, P. K.; Jullesson, D.; Elfwing, A.; Liin, S. I.; Musumeci, C.; Zeglio, E.; Elinder, F.; Solin, N.; Inganas, O., Electronic polymers in lipid membranes. *Sci. Rep.* **2015,** *5*, 11242.
46. Liu, L.; Yang, C.; Zhao, K.; Li, J.; Wu, H.-C., Ultrashort single-walled carbon nanotubes in a lipid bilayer as a new nanopore sensor. *Nat. Commun.* **2013,** *4*, 2989.
47. *Carbon Nanotubes: Synthesis, Structure, Properties, and Applications*. Springer: 2001.
48. Fagan, J. A., Aqueous two-polymer phase extraction of single-wall carbon nanotubes using surfactants. *Nanoscale Adv.* **2019,** *1*, 3307.
49. Li, H.; Gordeev, G.; Garrity, O.; Peyyety, N. A.; Selvasundaram, P. B.; Dehm, S.; Krupke, R.; Cambré, S.; Wenseleers, W.; Reich, S.; Zheng, M.; Fagan, J. A.; Flavel, B. S., Separation of specific single-enantiomer single-wall carbon nanotubes in the large-diameter regime. *ACS Nano* **2020,** *14*, 948.
50. Li, H.; Gordeev, G.; Garrity, O.; Reich, S.; Flavel, B. S., Separation of small-diameter single-walled carbon nanotubes in one to three steps with aqueous two-phase extraction. *ACS Nano* **2019,** *13*, 2567.
51. An, H. J.; Kim, S.; Seo, H.; Yoo, P. J.; Kim, W.-J., Simultaneous separation of high-purity semiconducting and metallic single-walled carbon nanotubes by surfactant concentration-controlled gel chromatography. *Appl. Surf. Sci.* **2020,** *508*, 145258.
52. Lu, W.; Wang, D.; Chen, L., Near-static dielectric polarization of individual carbon nanotubes. *Nano Lett.* **2007,** *7*, 2729.

Chapter 5. Outlook

Nanofluidic research is rapidly expanding owing to both technology developments and more research groups joining this burgeoning field. Various model systems can be utilized to probe transport phenomena at an atomic-scale and reveal the underlying physics governing the unique behaviors. To date, we have been able to study the intrinsic water and ionic transport through our excellent model system, CNTPs. The customizability of this system has the additional advantage of flexible design which can be leveraged and customized to work in several different set-ups. In this chapter, I propose new methods to improve CNTP-based systems using several different approaches. First, I am going to discuss methods for increasing the purity of CNTP batches, in terms of both CNT chirality and CNTP length. Second, I will present various chemical modifications to CNTP rims that could bring extra transport controls at either end. Third, I will discuss the development of alternative measurement platforms, using polymer bilayers or using glass capillary tips instead of planar lipid bilayers covering an aperture. Last but not least, I will present a design that combines all features listed above and the gateable CNTP devices discussed in Chapter 4 to make a flexible CNTP module with controllable components for membrane pore design and nanofluidic circuitry. Details of each potential improvements and preliminary results are discussed below.

5.1 CNTP Chirality and Length

As demonstrated by our previous studies using nCNTP and wCNTP, water and ion permeability values highly depend on the CNTP diameter.[1, 2, 3] Additional reports in the literature have also shown that metallic tubes result in higher conductance values compared to semiconducting tubes.[4, 5] These findings were corroborated by my Comsol simulations (see Chapter 4), which showed similar trends in the results. CNT separation methods have significantly improved over the last ten years, meaning that the purity of processed CNT samples can be more accurately tuned.[6, 7, 8] Using chirality separated CNTs means that the fabricated CNTPs will have a single chirality with a certain electronic behavior and a precisely known diameter . Using individual chirality-specific

CNTPs, we will be able to obtain single channel conductances of metallic tubes and semiconducting tubes, even to capture permeability values through CNTPs with the same diameters but different chiral indices. Obtaining diameter-dependent permeability values will also be possible with minimal diameter interval like 0.1 nm, which will help figuring out the critical diameter for single-file water chain in the nanotubes. A potential remaining challenge to creat chiral-pure CNTPs is the stability of different CNT chiralities during extended tip-sonication; it is possible that certain chiralities are less mechanically stable and may not be able to generate CNTPs.[9]

Another important consideration is the length of the CNTPs. We have previously observed a distribution in CNTP length (as obtained from cryogenic TEM images), ranging from 3 nm to 40 nm, with average lengths of around 10 nm.[10, 11] It is uncertain whether this wide distribution would cause fluctuations in permeability measurements or it actually has no effect on transport results as suggested by the simulation from Kalra *et al*., showing that entrance effects dominate transport behaviors.[12] In order to further probe and understand the role of nanotube length on transport properties, it is important to be able to more accurately control the CNTP length distributions in the solution. This can be achieved using density gradient ultracentrifugation in order to separate narrow length distributions of CNTPs which can subsequently be used to measure the single channel conductance of the different length fractions.[13, 14] This approach will require additional efforts to overcome the current resolutions in CNT length separation and also efforts to increase the final concentrations of the CNTP fractions.

Using CNTP samples with more precisely known properties offers an occasion to fine-tune the experimentally measured water and ion permeability values. Increasing the purity of the starting CNT samples can only benefit CNTP studies, and as such is deemed a necessary next step despite the many challenges associated with achieving these solutions. Owing to the impact of nanotube diameter distributions on density gradient separation, obtaining single chirality CNTPs should be the first goal, and these samples should subsequently be used for the length separation studies.

5.2 Chemical Modifications at CNTP Rims

The functional groups at the entrance of CNTPs critically affect cation/anion selectivity and can also change the resulting conductance value.[1, 3] In my work to date, I have examined the differences in ionic transport through CNTPs at neutral and acidic pHs (See Chapter 2 and 3), demonstrating the impact of entrance charges on the transport behavior.[1, 3] However, instead of changing environmental conditions like pH, the addition of chemical modifications at CNTP ends could be used to manipulate the transport behavior. In our work, the ends of CNTPs are carboxylate groups that are capable of undergoing EDC coupling, and as such can be used to add a variety of functional groups.[15, 16] I propose two methods for performing these reactions: (1) attaching functional groups to CNTPs in aqueous solution and (2) functionalizing the ends of CNTPs following incorporation into lipid bilayers. Both methods have potential challenges; the former method could impact the CNTP incorporation rate into lipid bilayers, while the latter would generate asymmetric functional groups by only modifying one side, which could alter transport behavior. Regarding which functional groups to employ, several options exist. Methylation would give neutral CNTP ends at pH 7.5 (Fig. 5.1A), which should result in conductance and selectivity numbers similar to unmodified CNTPs at pH 3.0.[15] Alternatively, switching the ends to a positively charged group could give rise to anion selective channels (Fig. 5.1B).

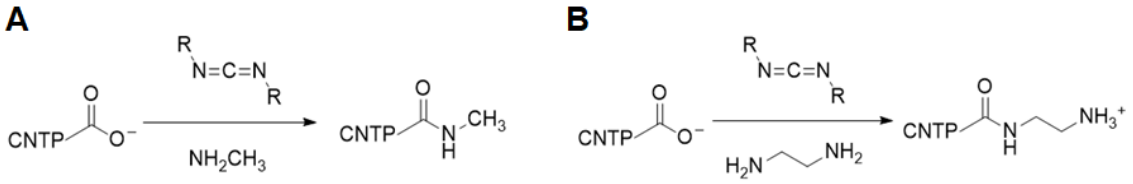

Figure 5.1. Chemical modifications at CNTP rims. EDC coupling to synthesize (**A**) neutral and (**B**) positively charged functional groups at CNTP entrances.

Terminal modifications can also be used to introduce macromolecules at CNTP ends, for example gold nanoparticles (AuNP) as previously demonstrated by our group.[11] CNTPs were first functionalized with sulfur groups using EDC coupling and AuNPs were attached by taking advantage of the affinity between gold and sulfur (Fig. 5.2A). To

match the narrow CNTP diameters, AuNPs with diameter less than 5 nm were used. The AuNP attachments were used to help locating the CNTP in cryo-TEM images (Fig. 5.2B), and may also be able to serve as a gate at CNTP entrances, introducing on/off current response. This idea could further be extended to attach DNA aptamers or antibodies for small molecule detection.[17]

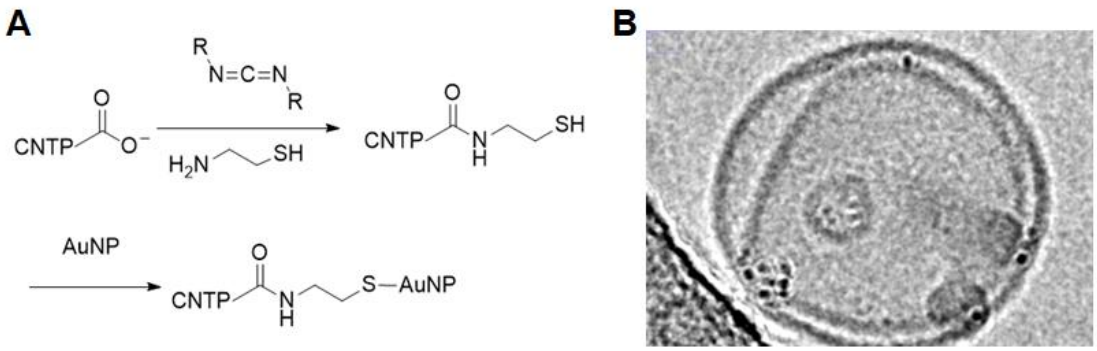

Figure 5.2. Au-CNTP modification. (**A**) Chemical modifications at CNTP ends to add a sulfur group and subsequently attach a gold nanoparticle (AuNP). (**B**) Cryogenic TEM images of lipid vesicles with Au-CNTPs, which AuNPs are *ca.* 3 nm.

5.3 CNTP in Polymer Membranes and Glass Capillary Platforms

Our group has shown that CNTPs can be incorporated into amphiphilic block copolymer vesicles, which enables a broader range of applications.[18] Applying similar rationale, replacing planar lipid bilayers with polymer materials would allow ionic measurements of CNTP across a wider temperature range, and perhaps not only in aqueous solution but also in organic solvent conditions due to the increased stability of polymer. Previously the main challenge has been that the temperature required for polymer vesicles to burst and cover the aperture is much higher than that for lipid vesicles. To address this problem, a new setup is required with better temperature and humidity control. Nevertheless, a recently published study by Wanunu group utilized polymers in the painting method of lipid bilayer formation,[19] which is much easier to accomplish in experiments and is worth trying in the future with our CNTPs.

An alternative platform to vesicles and planar lipid bilayers is the glass capillary set-up.[20, 21] We have previously tried forming DOPC lipid bilayers using the tip-dip method

at glass capillary ends[22] and could observe current jumps following the addition of CNTP stock solution (Fig. 5.3A), indicating CNTP insertion. The resulting I-V curves showed great sealing with the DOPC lipid bilayers and single wCNTP conductance after one insertion (Fig. 5.3B). A future goal of this work would be to develop a capillary tip with a CNTP protruding that could serve as a probe for scanning ion conductance microscopy.[23] However, during trials, we observed that the CNTP-membrane was unstable as the glass capillary was moved. In an attempt to address this issue, we utilized a gel-filled capillary to maintain the CNTP tip structure (Fig. 5.3C).[24, 25] However, in this setup we could not observe CNTP insertion (Fig. 5.3D) despite achieving membrane seals.

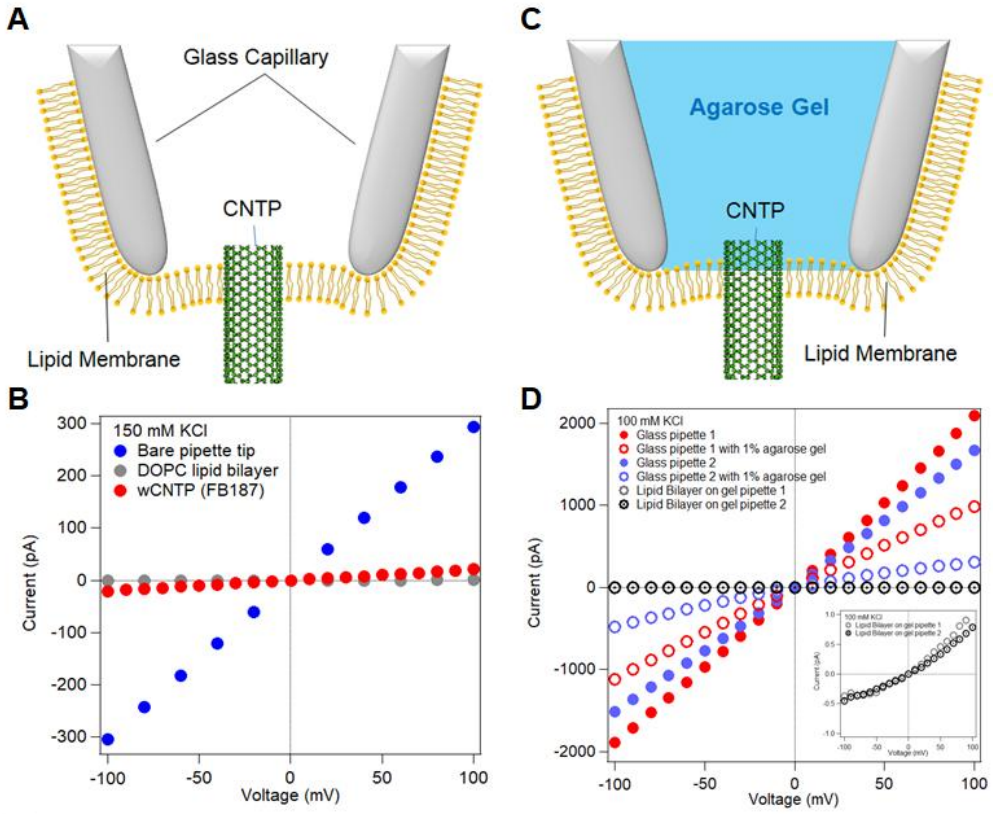

Figure 5.3. Glass capillary platform for CNTPs. (**A**) The original setup with DOPC lipid membrane and single wCNTP insertion. (**B**) The corresponding I-V curves for bare glass capillary tip, lipid bilayer sealing, and single wCNTP conductance for a glass capillary platform. (**C**) A gel capillary setup to increase the stability. (**D**) I-V curves show extra variants caused by gel filling and the lipid bilayer sealing (inset).

5.4 Integrated CNTP Nanofluidic Circuitry

The transport behavior of CNTPs is highly dependent on the CNTP size and the functional groups at the rim.[1, 3] For example, due to the high cation selectivity of CNTPs, a diode behavior was previously observed for nCNTPs with one negatively charged end and one uncharged end.[1] Furthermore, as shown in the Comsol simulation (Chapter 4), a gateable wCNTP device is feasible with an additional gate voltage and optimal lipid conditions. With additional systematical examination, future work should be able to attribute weighted factors for these various components, such as diameter, length, and entrance charges. This knowledge can then be leveraged to manipulate CNTPs in order to obtain the desired transport properties. It will enable us to further amplify the current rectification of CNTPs demonstrated in Comsol by increasing the passage current at one gate voltage while maintaining a close to zero current at the reverse gate voltage. By taking numerous changeable factors into account, we should be able to achieve a complex system that can be fine-tuned in many different ways. As such, CNTPs have the potential to become a flexible module with controllable components for future membrane pore design and nanofluidic circuitry.

Acknowledgement

Many thanks to Dr. Alice Gillen for discussions regarding the CNT purification project. Special thanks to Dr. Kazuki Shigyou, Prof. Toshio Ando, and summer intern Alexa Kassels for their efforts on the glass capillary project.

References

1. Tunuguntla, R. H.; Henley, R. Y.; Yao, Y. C.; Pham, T. A.; Wanunu, M.; Noy, A., Enhanced water permeability and tunable ion selectivity in subnanometer carbon nanotube porins. *Science* **2017,** *357*, 792.
2. Li, Y.; Li, Z.; Aydin, F.; Quan, J.; Chen, X.; Yao, Y. C.; Zhan, C.; Chen, Y.; Pham, T. A.; Noy, A., Water-ion permselectivity of narrow-diameter carbon nanotubes. *Sci. Adv.* **2020,** *6*.
3. Yao, Y.-C.; Taqieddin, A.; Alibakhshi, M. A.; Wanunu, M.; Aluru, N. R.; Noy, A., Strong electroosmotic coupling dominates ion conductance of 1.5 nm diameter carbon nanotube porins. *ACS Nano* **2019,** *13*, 12851.
4. Pang, P.; He, J.; Park, J. H.; Krstic, P. S.; Lindsay, S., Origin of giant ionic currents in carbon nanotube channels. *ACS Nano* **2011,** *5*, 7277.

5. Liu, L.; Yang, C.; Zhao, K.; Li, J.; Wu, H.-C., Ultrashort single-walled carbon nanotubes in a lipid bilayer as a new nanopore sensor. *Nat. Commun.* **2013,** *4*, 2989.
6. Fagan, J. A.; Huh, J. Y.; Simpson, J. R.; Blackburn, J. L.; Holt, J. M.; Larsen, B. A.; Walker, A. R., Separation of empty and water-filled single-wall carbon nanotubes. *ACS Nano* **2011,** *5*, 3943.
7. Streit, J. K.; Lam, S.; Piao, Y.; Hight Walker, A. R.; Fagan, J. A.; Zheng, M., Separation of double-wall carbon nanotubes by electronic type and diameter. *Nanoscale* **2017,** *9*, 2531.
8. Fagan, J. A.; Khripin, C. Y.; Silvera Batista, C. A.; Simpson, J. R.; Haroz, E. H.; Hight Walker, A. R.; Zheng, M., Isolation of specific small-diameter single-wall carbon nanotube species via aqueous two-phase extraction. *Adv. Mater.* **2014,** *26*, 2800.
9. Cao, G.; Chen, X., The effects of chirality and boundary conditions on the mechanical properties of single-walled carbon nanotubes. *Int. J. Solids Struct.* **2007,** *44*, 5447.
10. Geng, J.; Kim, K.; Zhang, J.; Escalada, A.; Tunuguntla, R.; Comolli, L. R.; Allen, F. I.; Shnyrova, A. V.; Cho, K. R.; Munoz, D.; Wang, Y. M.; Grigoropoulos, C. P.; Ajo-Franklin, C. M.; Frolov, V. A.; Noy, A., Stochastic transport through carbon nanotubes in lipid bilayers and live cell membranes. *Nature* **2014,** *514*, 612.
11. Tunuguntla, R. H.; Allen, F. I.; Kim, K.; Belliveau, A.; Noy, A., Ultrafast proton transport in sub-1-nm diameter carbon nanotube porins. *Nat. Nanotechnol.* **2016,** *11*, 639.
12. Kalra, A.; Garde, S.; Hummer, G., Osmotic water transport through carbon nanotube membranes. *Proc. Natl. Acad. Sci. U.S.A.* **2003,** *100*, 10175.
13. Sun, X.; Zaric, S.; Daranciang, D.; Welsher, K.; Lu, Y.; Li, X.; Dai, H., Optical properties of ultrashort semiconducting single-walled carbon nanotube capsules down to sub-10 nm. *J. Am. Chem. Soc.* **2008,** *130*, 6551.
14. Kuang, Y.; Liu, J.; Sun, X., Ultrashort single-walled carbon nanotubes: Density gradient separation, optical property, and mathematical modeling study. *J. Phys. Chem. C* **2012,** *116*, 24770.
15. Tunuguntla, R. H.; Zhang, Y.; Henley, R. Y.; Yao, Y.-C.; Pham, T. A.; Wanunu, M.; Noy, A., Response to Comment on "Enhanced water permeability and tunable ion selectivity in subnanometer carbon nanotube porins". *Science* **2018,** *359*, eaaq1241.
16. Tunuguntla, R. H.; Hu, A. Y.; Zhang, Y.; Noy, A., Impact of PEG additives and pore rim functionalization on water transport through sub-1 nm carbon nanotube porins. *Faraday Discuss.* **2018,** *209*, 359.
17. Xiao, Y.; Lubin, A. A.; Heeger, A. J.; Plaxco, K. W., Label-free electronic detection of thrombin in blood serum by using an aptamer-based sensor. *Angew. Chem. Int. Ed.* **2005,** *44*, 5456.
18. Sanborn, J. R.; Chen, X.; Yao, Y. C.; Hammons, J. A.; Tunuguntla, R. H.; Zhang, Y.; Newcomb, C. C.; Soltis, J. A.; De Yoreo, J. J.; Van Buuren, A.; Parikh, A. N.; Noy, A., Carbon nanotube porins in amphiphilic block copolymers as fully synthetic mimics of biological membranes. *Adv. Mater.* **2018,** *30*, e1803355.
19. Yu, L.; Kang, X.; Alibakhshi, M. A.; Pavlenok, M.; Niederweis, M.; Wanunu, M., Stable polymer bilayers for protein channel recordings at high guanidinium chloride concentrations. *Biophys. J.* **2021**.

20. Tognoni, E.; Baschieri, P.; Ascoli, C.; Pellegrini, M.; Pellegrino, M., Characterization of tip size and geometry of the pipettes used in scanning ion conductance microscopy. *Micron* **2016,** *83*, 11.
21. Cadinu, P.; Paulose Nadappuram, B.; Lee, D. J.; Sze, J. Y. Y.; Campolo, G.; Zhang, Y.; Shevchuk, A.; Ladame, S.; Albrecht, T.; Korchev, Y.; Ivanov, A. P.; Edel, J. B., Single molecule trapping and sensing using dual nanopores separated by a zeptoliter nanobridge. *Nano Lett.* **2017,** *17*, 6376.
22. Oiki, S.; Iwamoto, M., Lipid bilayers manipulated through monolayer technologies for studies of channel-membrane interplay. *Biol. Pharm. Bull.* **2018,** *41*, 303.
23. Watanabe, S.; Ando, T., High-speed XYZ-nanopositioner for scanning ion conductance microscopy. *Appl. Phys. Lett.* **2017,** *111*, 113106.
24. Ide, T.; Kobayashi T Fau - Hirano, M.; Hirano, M., Lipid bilayers at the gel interface for single ion channel recordings. *Anal. Chem.* **2008**.
25. Navikas, V.; Leitao, S. M.; Marion, S.; Davis, S. J.; Drake, B.; Fantner, G. E.; Radenovic, A., High-throughput nanocapillary filling enabled by microwave radiation for scanning ion conductance microscopy imaging. *ACS Appl. Nano Mater.* **2020,** *3*, 7829.

Appendix I. Modified Planar Lipid Bilayer Method

SiN_x nanopore chip fabrication. SiN_x nanopore chips fabrication followed the protocols that we reported in *Science* **2017**, *357*, 792-796. Briefly, a 500 µm-thick and 100 mm diameter silicon <100> wafer was cleaned and 2 µm-thick SiO_2 films were thermally deposited on both sides, followed by 50 nm of SiN_x deposited on both sides of the wafer. 100 nm diameter circular windows were defined by electron-beam lithography on one side of the wafer and etched with SF_6 plasma. Photolithography was used on the other side to define the pattern for KOH etching and buffered oxide etching down to SiN_x membrane. This process produces freestanding SiN_x membranes containing *ca.* 100 nm diameter through-holes. To improve the quality of chips, we additionally utilized atomic layer deposition (ALD) to deposit *ca.* 5 – 10 nm silicon dioxide (SiO_2) on both sides of chips after plasma cleaning. After the ALD deposition the chips were cleaned for 20 min in heated Piranha solution: 33% of hydrogen peroxide (35 wt.% in H_2O, stabilized, Acros organics, CAS: 7722-84-1) and 66% of sulfuric acid (Merck, GR ACS, CAS: 7664-93-9). After cleaning the chips were rinsed by and stored in deionized water.

Vesicles preparation. Preparation of the *ca.* 200 nm diameter large unilamellar vesicles (LUV) followed a previously described protocol in *Science* **2017**, *357*, 792-796. The lipid composition was 90% 1,2-dioleoyl-*sn*-glycero-3-phosphocholine (DOPC, Avanti, CAS: 4235-95-4) and 10% cholesterol (Sigma, CAS: 57-88-5). Briefly, the mixture of DOPC and cholesterol was dried and then bath sonicated in 200 mM KCl to form lipid vesicles. After 30 min incubation, vesicle solution underwent 10 cycles of freeze and thaw to break possible multi-layers. Next, the solution was extruded through a 200 nm filter. The size of final vesicles was verified by dynamic light scattering (DLS).

Ion conductance measurements. Cleaned SiN_x chips were mounted in a home-made Teflon fluid cell with silicon glue (Ecoflex 5, Smooth-On, Inc.). The cell was equipped with a pair of Ag/AgCl electrodes. For some measurements 1 M KCl salt bridges (4 wt. % agar powder, Alfa Aesar, CAS: 9002-18-0) were used. Conductance characteristics

were recorded with a patch clamp amplifier (Axon Instruments, CV 203BU Headstage, Axopatch 200B Integrating Patch Clamp, and Axon CNS Digidata 1440A). The electrolyte solution for the measurements contained potassium chloride (Sigma, CAS: 7447-40-7) TE buffer, 10 mM Trizma base (Sigma, CAS: 77-86-1) and 1 mM EDTA (Sigma-Aldrich, CAS: 60-00-4). Solution pH values were titrated with hydrochloric acid. Conductance values were determined from the slope of the recorded I-V curves. 50+ different devices were used and at least three measurements were performed for each concentration and pH value. Conductance measured in this modified planar lipid bilayer platform matched the values obtained in the painted lipid bilayer platform that values obtained from I-V curves matched the conductance values determined from observing conductance jumps following individual CNTP incorporation events.

Ion selectivity determination with reversal potential measurements. To measure ion selectivity an I-V curve was first recorded using 10 mM KCl in both top and bottom chambers and compensated for any instrumental offsets to the zero-current voltage. The solution of the top chamber was then changed to a different concentration and an I-V curve was recorded using the fixed original offset. The value of the reversal potential was determined from the new zero-current voltage value and used to derive the ion selectivity using Goldman-Hodgkin-Katz (GHK) equation:

$$V_{rev} = (2t_+ - 1)\frac{RT}{F}\ln\frac{c_{top}}{c_{bottom}}$$

where V_{rev} is the reversal potential, t_+ is the effective transmembrane number of cation (percentage of cation transferring through membrane out of total ion transfer), c is the electrolyte concentration for either top or bottom chamber, R is the molar gas constant, T is the temperature, and F is the Faraday constant. The permselectivity (P) was then calculated using the cation transport number in bulk (t_{+bulk} = 0.49 for KCl solution) and the following equation:

$$P = \frac{t_+ - t_{+bulk}}{1 - t_{+bulk}}$$